

TECHNISCHE UNIVERSITÄT MÜNCHEN

Lehrstuhl für Technische Chemie II

On the Dry Reforming of Methane at Elevated Pressures

Linus Andreas Schulz

Vollständiger Abdruck der von der Fakultät für Chemie der Technischen Universität München zur Erlangung des akademischen Grades eines

Doktors der Naturwissenschaften (Dr. rer. nat.)

genehmigten Dissertation.

Vorsitzender: Univ.-Prof. Dr.-Ing. K.-O. Hinrichsen

Prüfer der Dissertation: 1. Univ.-Prof. Dr. techn. J.A. Lercher

2. Univ.-Prof. Dr. rer. nat. S. Günther

Die Dissertation wurde am 08.06.2016 bei der Technischen Universität München eingereicht und durch die Fakultät für Chemie am 17.10.2016 angenommen.

„Daß ich nicht mehr mit sauerm Schweiß,
Zu sagen brauche, was ich nicht weiß;
Daß ich erkenne, was die Welt
Im Innersten zusammenhält“

Johann Wolfgang von Goethe - Faust

Acknowledgements

Ich möchte mich als erstes bei meinem Doktorvater Prof. Johannes Lercher bedanken für die Chancen, die er mir durch seine Unterstützung geboten hat. Sowohl die Aufnahme in die Gruppe, als auch die verschiedenen Auslandsaufenthalte wäre ohne seine Hilfe nicht möglich gewesen. Was lange währt wird endlich gut.

Weiterhin danke ich meinem Betreuer Prof. Andreas Jentys, der stets ein offenes Ohr für meine Anliegen hatte und mir auch durch gelegentliches Schieben in die richtige Richtung meinen Weg zum Doktor gewiesen hat. Danke für all die langen und ausdauernden Diskussionen über Nickel und was es so alles mit Kohlenstoff anrichten kann.

Also, I would like to thank Prof. Cathy Chin for letting me join her group for several weeks and helping me so much with the kinetics of my reaction. I really enjoyed my time in Toronto and I learned so incredibly much there.

Ein besonderer Dank gilt dem Bundesministerium für Wirtschaft und Energie, unter dessen Förderung ich mein Promotionsprojekt durchführen konnte (Fördernummer 0320327856D). Ebenso möchte ich meinen Partnern aus dem DRYREF Projekt, BASF SE, hte GmbH, KIT, Linde AG und TU Dresden, danken, die in vielen Stunden Diskussion die verschiedenen Aspekte meiner Arbeit immer wieder kritisch unter die Lupe genommen haben und so zu deren guten Gelingen wesentlich beigetragen haben.

Außerdem möchte ich mich bei all unseren guten Seelen des Lehrstuhls bedanken. Xaver, ohne den ich noch immer ohne Anlage dastehen würde. Andreas, Martin, Helen, Bettina, **Karen** und **Uli**, für die all die kleinen Dinge im Hintergrund die so unglaublich wichtig sind. Und natürlich **Steffi**, dank der man immer sicher sein konnte, dass alles so reibungslos wie möglich ablief.

All meinen Kollegen (besonders aus Büro 46301) möchte ich für die hervorragende Atmosphäre danken, die stets in der Gruppe herrschte. Aus vielen dieser ehemaligen Kollegen sind gute Freunde geworden und ich würde es bedauern euch nicht kennengelernt zu haben: Oliver, Dani, Sarah, Michi, Claudia, Moni, Jenni, Robin, Stefan, Lisl und die Sebastians. Dazu kommt noch der Fichtl, der einfach alles weiß und alles kann.

Yu danke ich für seine unendliche Hilfsbereitschaft und seine Freundschaft, die er mir während unserer gemeinsamen Zeit des Trockenreformierens geboten hat. Ohne dich wäre ich noch immer nicht fertig.

Dann gibt es unter all den Leuten in der TC II noch drei Personen, die mir – und das obwohl sie alle Ingenieure sind ☺ – besonders ans Herz gewachsen sind. Christian, mein ewiger Büronachbar, der über die Jahre hinweg immer wieder eine unschätzbare Hilfe war, Max, den ich zu Beginn falsch eingeschätzt habe und der mich eines Besseren belehrt hat und Steffi, die mir gezeigt hat, wie schnell 12-Stunden-Schichten vergehen können. Danke!

Ebenso danke ich all den Studenten, die mir über die Jahre geholfen haben. Insbesondere Matthias, Kai, Robert und Marvin, ihr habt mir unglaublich geholfen.

Consti, Daniel, Roland, Joe, Waldi und Flo, die mich schon im Studium aushalten mussten und mir dennoch ihre Freundschaft geboten haben, danke ich für die nun schon fast 10 Jahre dauernde wunderbare Zeit in München, Schenna und Garmisch.

Zu guter Letzt möchte ich Danke sagen meiner Familie, Heike, Manfred, Matti und Enno und natürlich meiner **Helene** die mich alle immer unterstützt haben und bei denen ich mich stets geborgen fühlten konnte. Danke für die Möglichkeit zu träumen und dabei nicht aus dem Tritt zu geraten.

Table of Contents

1 Introduction

1.1 General

The distribution of fossil feedstock has been changing over the last decades, and especially the accelerating shale gas production in the United States speeded up this process. The United Sates turned from one of the major importers of fossil fuels to an important exporter. This went hand in hand with a steep drop in gas prices over the last 10 years. While the price was 8.69 $/Mio Btu (British thermal unit) (Henry Hub) in the end of 2005, it dropped to 2.62 $/Mio Btu in 2015 [1]. In Germany there are exploitable shale gas resources of estimated $0.7 – 2.3 \cdot 10^{12}$ m³ (in comparison: conventional gas reserves are about $0.15 \cdot 10^{12}$ m³) [2] but hydraulic fracturing (also known as fracking) of shale gas is strongly under discussion due to its non-resolved environmental and sanitary risks. Consequently, up to date there are no significant amounts of shale gas produced but this might chance over the next decades. Regardless these national concerns, the worldwide production capacities and therefore the possible utilization pathways for hydraulic cracking are constantly increasing.

Besides direct usage of natural gas for heating or mobility, natural gas serves as a raw material in the production of chemicals, mainly via the synthesis gas route. Synthesis gas is a mixture of H_2 and CO in varying ratios. The numerous production techniques differ mainly in the composition of the feed – and consequently in the resulting H_2/CO ratio of the product gas. The most notable processes are steam reforming (SRM) (1-2) dry reforming (DRM) (1-1), partial oxidation (POx) (1-3) and autothermal reforming (ATR) (1-4).

$CO_2 + CH_4$	⇌	$2\ CO + 2\ H_2$	$\Delta H^0_{298K} = 247\ \mathrm{kJ/mol}$ [3]	(1-1)
$H_2O + CH_4$	⇌	$CO + 3\ H_2$	$\Delta H^0_{298K} = 206\ \mathrm{kJ/mol}$ [3]	(1-2)
$CH_4 + ½\ O_2$	⇌	$CO + 2\ H_2$	$\Delta H^0_{298K} = -36\ \mathrm{kJ/mol}$ [4]	(1-3)
$CH_4 + 0.5\ O_2 + H_2O$	⇌	$3\ H_2 + 3\ CO + H_2O$	$\Delta H^0_{298K} = -12\ \mathrm{kJ/mol}$ [5]	(1-4)

In steam reforming, the product composition and side effects are usually controlled by the amount of steam fed into the reactor and the H_2O/CH_4 ratio is normally greater than 1. This leads to H_2/CO ratios above 3, which would be the result of the stoichiometric reaction of CH_4 and H_2O. In POx and in ATR, methane is processed with oxygen, a normally very costly raw material [6, 7]. It is clearly visible from Figure 1-1 that DRM, the transformation of CH_4 with CO_2 produces the synthesis gas with the highest carbon content. By using a combination of the various processes, synthesis gas in a theoretical H_2/CO ratio range from 0.8 to 4.9 can be produced.

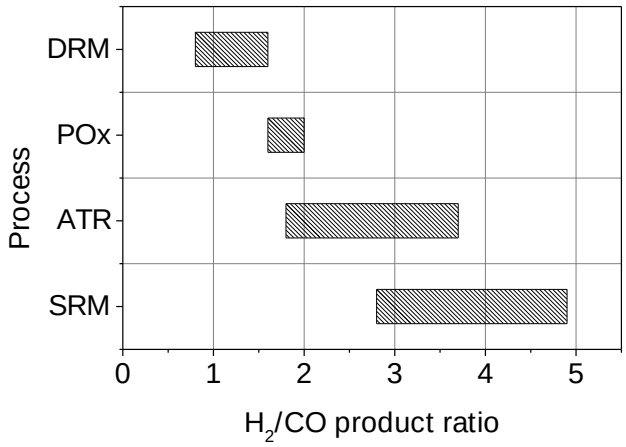

Figure 1-1 Possible H2/CO ratios of the technical synthesis-gas production processes [8].

The product composition is also dependent on the available feedstock, as the C/H- and the C/O-ratios can vary tremendously in the accessible natural gasses of different exploitation sites. Synthesis gas can be used in a wide array of downstream applications in a refinery, but while the SRM is mostly employed to produce large amounts of H_2 for hydro-treating, DRM provides feedstock for Fischer-Tropsch or methanol/DME synthesis. In addition, the two reactants for the DRM can be major fractions of natural gas, which renders on site utilization at remote exploration locations imaginable – especially embedded into networks that require only little amounts of steam and the production costs of such would not match the value.

All processes mentioned above require defined feed compositions. However, the H_2/CO ratio produced is not only defined by the DRM reaction but also by several side reactions that occur in parallel under the applied conditions. In the next section, an overview on the most impacting secondary reactions of dry reforming will be given.

1.2 Dry reforming side reactions

There are two major concerns that need to be considered when discussing the side reactions in DRM. The first one regards the product H_2/CO ratio produced in the process for which the reverse water gas shift reaction (RWGS) is most influencing. The second topic to address is the carbon deposition during the reaction by Boudouard reaction, the activation of methane and the reverse gasification of coal.

1.2.1 The Reverse Water Gas Shift reaction (RWGS)

The RWGS (1-5) converts excess CO_2 and H_2 into CO and H_2O, which has two effects: 1) the H_2/CO ratio drops significantly. There are few chemical processes that can utilize synthesis gas with a H_2/CO ratio below 1 but thermodynamically the equilibrium composition of the DRM process would be 0.8 due to RWGS (as will be shown later in detail). 2) The RWGS enables steam reforming in gas feeds that originally do not contain any water by producing it internally.

$$CO_2 + H_2 \rightleftharpoons CO + H_2O \qquad \Delta H^0_{298K} = 41 \text{ kJ/mol [3]} \qquad (1\text{-}5)$$

It even has been claimed in literature that the mechanisms for dry and steam reforming are basically the same and the water formed from RWGS is the key intermediate also for DRM. In this case, some hydrogen would be produced from the activation of methane without the influence of CO_2. In a second step the production of hydroxyl groups from hydrogen and oxygen would take place and these would react with surface carbon and form CO [9]. This question will be addressed in detail in later chapters of this work.

1.2.2 Carbon formation reactions

The Boudouard reaction (1-6), the activation of methane (1-7) and the reverse gasification of coal (RGC, (1-8)) are those side reactions presumably most relevant for the coke deposition during the dry reforming. While the Boudouard reaction and the RGC influence the coke deposition at high product concentrations, the activation of methane – also a postulated step in the reforming mechanism [10] – stimulates carbon deposition at high reactant concentrations. Under industrial relevant conditions (≤ 1000 K, ≤ 1 MPa) all of these reactions must be considered as reversible and all of them share not only the same reactants and products, but also the same surface intermediates. Therefore, all of them need to be taken into account when it comes to an assessment of a reaction mechanism or reaction kinetics.

$$CO \rightleftharpoons C + CO_2 \qquad \Delta H^0_{298K} = -171 \text{ kJ/mol [3]} \qquad (1\text{-}6)$$

$$CH_4 \rightleftharpoons C + 2\,H_2 \qquad \Delta H^0_{298K} = 75 \text{ kJ/mol [3]} \qquad (1\text{-}7)$$

$$CO + H_2 \rightleftharpoons C + H_2O \qquad \Delta H^0_{298K} = -131 \text{ kJ/mol [3]} \qquad (1\text{-}8)$$

Among the relevant reactions, there are exothermic as well as endothermic ones, thus the product composition strongly depends on the reaction temperature. Additionally,

most of the reactions are not constant in volume. Hence, the next section deals with the influence of system temperature and pressure on the theoretically possible product composition in detail.

1.3 Thermodynamic assessment

Both the DRM and the SRM are endothermic which means that high reaction temperatures increase the thermodynamically possible conversion level of CH_4, CO_2 and H_2O. Additionally, high temperatures reduce the tendency for coke deposition, as the Boudouard reaction (1-6) and activation of methane (1-7) are exothermic and hindered at increased temperatures. To obtain an overview of the thermodynamic boundaries of the reaction network, the equilibrium compositions of the gas phase components CH_4, CO_2, CO, H_2, H_2O and N_2 have been calculated at various temperatures and pressures[1].

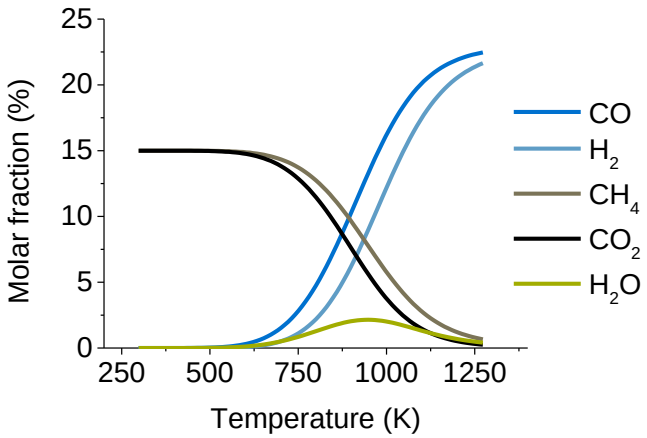

Figure 1-2 Calculation of the equilibrium composition of the gasses - CH_4, CO_2, H_2, CO, H_2O and N_2 in a temperature range from 373 – 1273 K at 1MPa of pressure. Initial composition of the gasses was 15/15/70 mol-% of CH_4/CO_2/N_2. For better visibility, molar fraction of N_2 has been ignored in the graph.

As can be observed from the results of these calculations in Figure 1-2 at temperatures below 573 K there is no observable conversion of CH_4 or CO_2. At higher temperatures, the concentrations of the two reactants decrease constantly in the equilibrium composition with a simultaneously increasing content of H_2 and CO. The formation of

[1] *HSC Chemistry 6.0* by *Chemistry Software Ltd.* was used for the calculations.

water can be observed and the content of CO is always higher than the one of H_2 at a constantly lower concentration of CO_2 with respect to CH_4. These deviations have their maximum between 873 K and 973 K – the same temperature range as the maximum in the water content. At higher temperatures, the possible conversions of the reactants as well as the theoretical yields of the products converge again, respectively. Recently, Gardner et al. could prove these theoretical profiles to be accurate by performing temperature programmed surface reactions (TPSR) at in temperature range from 473 K to 1173 K, The experiments were conducted at a pressure of 0.2 MPa and $CH_4/CO_2 = 1$ over $Ba_{0.75}Ni_yAl_{12-y}O_{19-x}$ (y = 0.4 – 1) resembled the predicted data well [11].

Let us have a look at the pressure dependence of the reactions in the next step. High pressures are favored in technical reformers mainly for two reasons: 1) Smaller apparatuses can be used, which reduces the costs for new facilities. 2) Many downstream processes in a refinery are operated at high pressures and the compression particularly of hydrogen is difficult and costly, which renders the production of high pressure synthesis gas economically feasible. Simultaneously, reforming reactions are not constant in volume. Stoichiometric steam reforming produces three H_2 molecules together with one CO from H_2O and CH_4, whereas dry reforming transforms CH_4 and CO_2 into two H_2 and two CO. With proceeding reaction, the volume expands or – as this technically usually is not possible in reforming reactors – the pressure and/or the gas velocity increases. According to Le Chatelier's principle, such a reaction will be suppressed by higher pressures. Consequently, an increasing system pressure will reduce the maximum possible conversion.

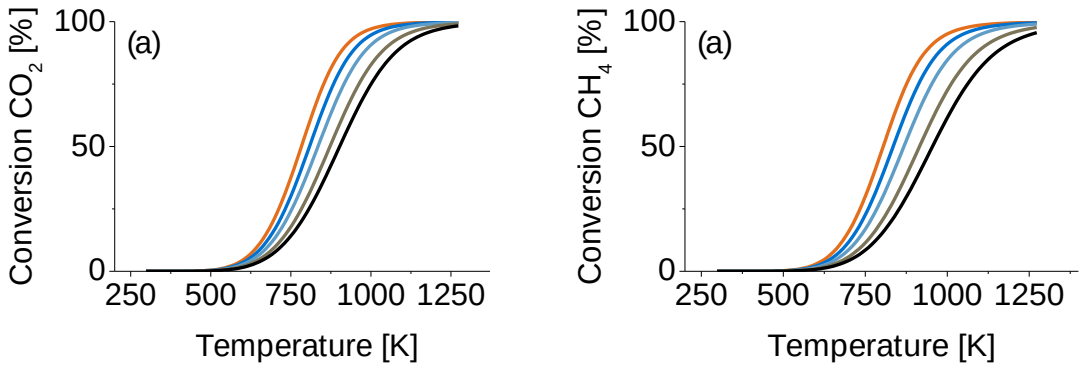

Figure 1-3 Influence of the system pressure on the thermodynamically possible conversion levels of (a) CO_2 and (b) CH_4 in a temperature range from 373 to 1273 K. The various pressures are ■ 0.05 MPa, ■ 0.1 MPa, ■ 0.2 MPa, ■ 0.5 MPa and ■ 1 MPa.

This effect can be seen in Figure 1-3 as the possible conversion of CO_2 (Figure 1-3, a) of CH_4 (Figure 1-3, b) at a particular temperature decrease constantly with higher system pressure. For example, to reach a CO_2 conversion of 60 % at 0.5 MPa of system pressure the reactor needs to be heated to 813 K while at a pressure of 1 MPa 933 K need to be set in order to obtain the same result. The same applies for CH_4 as e.g. the reactor temperature required for 60 % of conversion increases from 823 K (at 0.5 MPa) to 993 K (at 1 MPa) with increasing pressure. One has to note here that the pressure influences the conversion of CH_4 more than the one of CO_2.

One can easily deduce from the former figures that the H_2/CO ratio in the product stream also is strongly affected by reaction temperature and the pressure. The effect is especially significant for a variation in temperature as can be observed from Figure 1-4. The ratio rises from near zero – which means there is almost no H_2 in the mixture – to unity. The low ratio in the beginning can be explained by the formation of water through the RWGS reaction, which consumes most of the H_2 and produces H_2O. The molar fraction of water never exceeds a certain value which consequently limits the RWGS reaction and with increasing temperature the influence of the RWGS with respect to the product composition diminishes.

However, not only temperature but also pressure is influencing the processes in the reactor as can be observed from the individual graphs in Figure 1-4. While an equimolar composition of the products is reached already at 973 K at pressures below 0.1 MPa, an increase in pressure of to 1 MPa prevents this even at 1250 K to occur. Hence, the two parameters temperature and pressure can be used rather independently to alter the conditions in the reactor and hence the performance of the process. As discussed before, high pressures are preferred for technical applications, which leads to also high temperature processes in order to compensate the lower conversions that come along with pressurization.

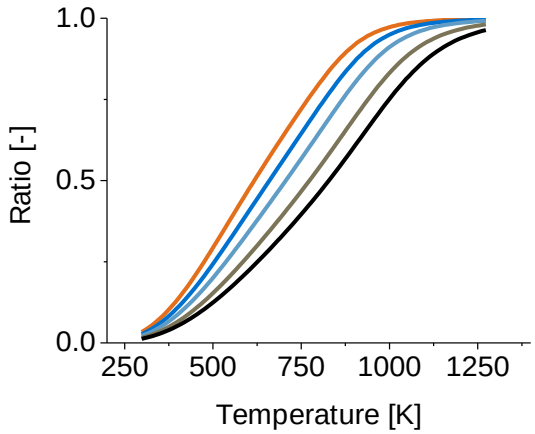

Figure 1-4 Calculated H_2/CO ratio at various reaction temperatures and system pressures. The applied pressures are ■ 0.05 MPa, ■ 0.1 MPa, ■ 0.2 MPa, ■ 0.5 MPa and ■ 1 MPa.

Most of the experimental work in this thesis was conducted at a temperature of 1123 K, under a pressure of 1 MPa and in a dilution of N_2. Thus the composition, conversions of CO_2 and CH_4 as well as the H_2/CO ratio as expected at the thermodynamic equilibrium have been summarized in Table 1-1.

Table 1-1 Thermodynamic equilibrium composition of the gas phase at 1123 K and 1 MPa of pressure and a gas feed composition of 15/15/70 CO_2/CH_4/N_2 as calculated with *HSC Chemistry 6.0*

Molar fraction [%]						Conversion [%]		H_2/CO [-]
N_2	CO_2	CH_4	CO	H_2	H_2O	CO_2	CH_4	
56	1	2	21	19	1	92	85	0.89

The thermodynamically possible conversion of CH_4 is 84 % and the one for CO_2 is 92 %, which leads to a very low concentration of those two gases in the product stream. The CO concentration is 21 % and thus marginally higher than the H_2 concentration at 19 %. This leads to a H_2/CO ratio of 0.89 and such a low H_2/CO ratio means that there is a high carbon content.

Additionally, the deposition of coke is increased at higher pressures as the deposited carbon is removed from the gas phase and adsorption-desorption processes are shifted towards the adsorbed states [12]. Hence, coke deposition would be a very simple way for the system to remove carbon from the gas phase and simultaneously reduce pressure. As shown before, there are several reactions in the reaction network that contain solid surface carbon as component. The upcoming chapter deals with the thermodynamic boundaries of carbon deposition during DRM in detail.

1.4 Carbon deposition

Carbon deposition is in general a challenge for technical applications. Firstly, the deposited carbon is removed from the product stream, and therefore lost as valuable product. Secondly, the carbon can cover the catalytic area and deactivate the catalyst. The first two reasons are significant but the most dangerous issue for the dry reforming process, in particular, is that the continuous deposition of carbon eventually can block and destroy the reactor. The content of graphitic carbon in the gas phase was calculated and can be found in Figure 1-5[2].

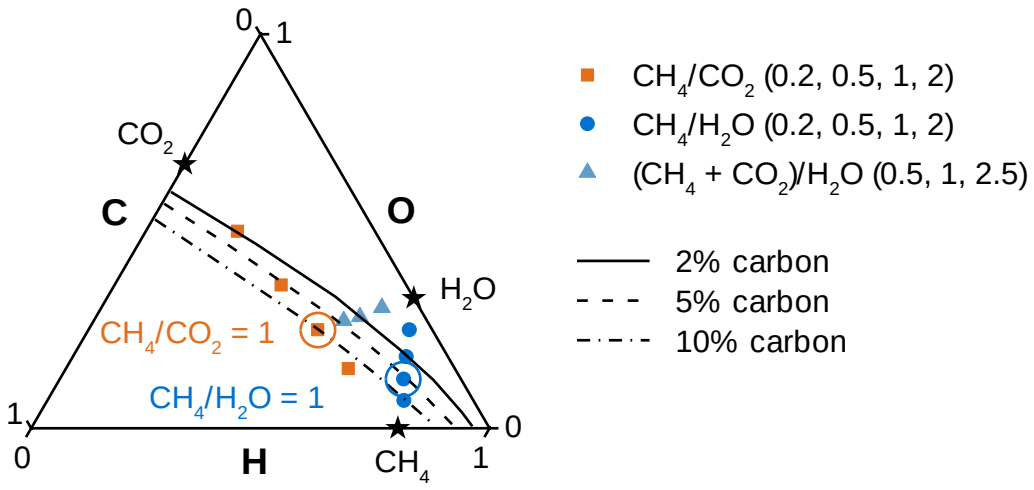

Figure 1-5 Thermodynamic calculation of the solid graphite content in the equilibrium composition. The content of 2 % (solid), 5 % (dashed) and 10 % (dashed and points) graphite has been plotted in lines at 1 MPa and 1123 K. The symbols show steam (●), dry (■) and mixed reforming (▲) at varying gas feeds. The CH_4/CO_2 and CH_4/H_2O ratios of 1 are highlighted in circles and pure H_2O, CH_4 and CO_2 are marked with stars.

The carbon content that is thermodynamically stable under the selected conditions (1023 K, 1 MPa), at an inlet composition of $CH_4/CO_2 = 1$, is 10 %, which can lead to severe coke deposition. Increasing the fraction of CO_2 or H_2O decreases the content of carbon. Hence, a CH_4/CO_2 ratio of 0.5 merely produces 5 % of coke and a ratio of 0.2 leads to a graphite content of less than 2 %. Steam reforming with a CH_4/H_2O ratio of unity produces a content of 5 % of carbon at the thermodynamic equilibrium. Technical steam reformers are operated with CH_4/H_2O between 0.2 and 0.4 to reduce the carbon deposition to a minimum [13]. For this work the influence of carbon deposition on the

[2] *HSC Chemistry 6.0* by *Chemistry Software Ltd.* was used for the calculations.

reaction was one crucial aspect, thus most of the experiments were conducted with CH_4/CO_2 ratios of 1 taking the carbon deposition into account.

Carbon formed under dry reforming conditions is likely to procedure very voluminous carbon nano-tubes (CNT´s) that can easily block the reactor during reaction and especially some base metals are known for their ability to form this kind of deposits [10]. The generally accepted mechanism of CNT formation is the creation of a Ni-carbide is formed that enables the Ni to dissolve in the Ni particle, to diffuse through the metal or on its surface and to leave it at another spot. This means the whisker-producing metal cluster gets encapsulated by carbon in the tip of the CNT and thereby determines the diameter of the latter. This principle in mind, Bitter et al. investigated the carbon formation behavior of different Ni materials under DRM conditions and they found that Ni cluster sizes smaller than a certain diameter suppress the buildup of coke strongly [14, 15]. They provided evidence that Ni particles smaller than 2 nm cannot create CNT´s and related this to the fact that the surface tension on the outside of such a thin fiber would be too high to create stable structures. Very similar results were published by Zhang et al., whereas they propose a particle size smaller than 10 nm to be crucial for the suppression of carbon [16].

CNT´s are formed at the active metals but the vast majority of the carbon is not in direct contact with the active surface any more after deposition. Thus carbon deposition must not consequently lead to deactivation. There is strong evidence in the literature that it is possible to conduct dry reforming at constant activity under conditions that strongly depose carbon during reaction [17-23]. Consequently, reactor blockage becomes the main risk.

Base metals such as Ni are known to be much more prone to coking than noble metals like Pt, Ru or Pd [9]. On the other hand, base metals would be preferred over noble metals in industrial applications due to their much better availability and their lower price. This issue has been addressed by synthesizing novel materials [24], developing suitable reactor concepts, like membrane reactors [25, 26], but also by trying to understand the basic principles of carbon deposition [27]. The effect of the catalytic material will be discussed in detail in chapters 2 and 1.

In the previous sections, the thermodynamic boundaries of the dry reforming have been discussed with a strong focus on the macroscopic effects. In the upcoming part, a closer look on the mechanisms and surface reactions postulated in literature over the last decades will be presented. Some aspects are generally accepted, but there is a vivid

discussion about other details, and therefore a closer look at both will be taken at the agreed and the disputed elements.

1.5 Reaction mechanism

Many people addressed the mechanism of DRM over the last years, although the outcome of the experiments often is strongly dependent on the chosen reaction conditions or catalytic materials. For both, dehydrogenation of hydrocarbons and cleavage of CO_2, a Langmuir-Hinshelwood mechanism is usually assumed. In addition, many references assume the C-H bond activation as rate determining step in the network. Simultaneously, the co-reactants CO_2 (DRM) or H_2O (SRM) are considered often as kinetically irrelevant. Apel'baum et al. were one of the first to describe a mechanism for steam reforming [28] and later they used the same model to describe dry reforming [29] (⟶ = irreversible reaction, ⇔ = quasi-equilibrated reaction, ⇌ = reversible reaction):

$CH_4 + *$	$\longrightarrow^{+}$	$CH_2* + H_2$	Step (1)
$CO_2 + *$	$\Leftrightarrow$	$CO + O*$	Step (2)
$O* + H_2$	$\Leftrightarrow$	$H_2O + *$	Step (3)
$CH_2* + H_2$	$\Leftrightarrow$	$CO* + 2\ H_2$	Step (4)
$CO*$	$\Leftrightarrow$	$CO + *$	Step (5)

The rate equation they derived from their network depends on the partial pressures of CH_4, CO, H_2 and H_2O:

$$r = \frac{kp_{CH_4}}{1 + a\left(\frac{p_{H_2O}}{p_{H_2}}\right) + bp_{CO}} \tag{1-9}$$

Iglesia et al. conducted extensive investigations on the mechanism of steam and dry reforming over various metals [30-33]. They discovered a sole influence of CH_4 on the dry and steam reforming rate over Ni and denoted this to the C-H bond activation as the RDS. They proved that the rate constants for CO_2 and H_2O reforming were quasi identical, as well as the energies of activation and additionally the values matched those

of CH_4 activation without oxidizing agent. Therefore, CO_2 and H_2O activation on the catalyst´s surface were even set as quasi equilibrated, which resulted into a reaction mechanism as it is presented in Figure 1-6. The adsorption and dissociation of CO_2, H_2O and H_2 are quasi equilibrated while the adsorption and desorption of CO onto the surface is assumed to be reversible and remarkably faster than CH_4 activation.

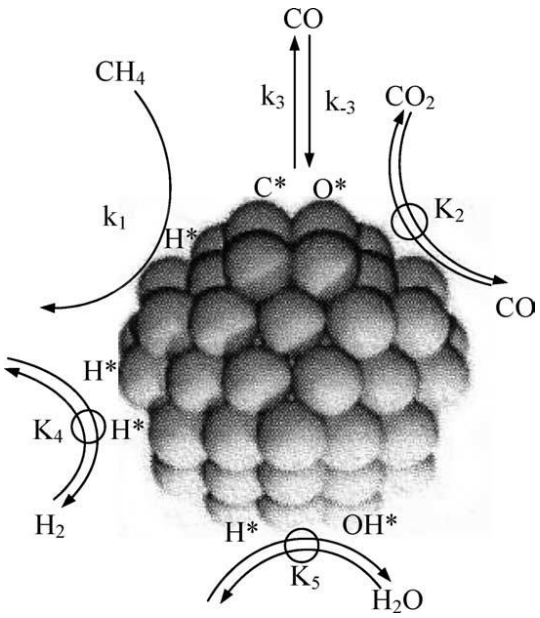

Figure 1-6 Reaction mechanism of steam and dry reforming over Ni catalysts postulated by Iglesia et al. [32]

The rate equation described for Ni catalysts is:

$$r = kp_{CH_4} \tag{1-10}$$

This is the case because they found the active centers to be quasi free of any reactive intermediates. In addition, they also investigated the kinetics for formation of C* (denoted as a_{c^*}) on the surface and found the two reactions

$$a_{C^*} = \frac{k' p_{CH_4} p_{H_2}}{p_{H_2O}} = \frac{k p_{CH_4} p_{CO}}{p_{CO_2}} \tag{1-11}$$

to be equal to one another. As $p_{CH_4} p_{H_2} / p_{H_2O}$ in related to $p_{CH_4} p_{CO} / p_{CO_2}$, via the water-gas shift equilibrium, both terms are directly proportional at any temperature [32]. They emphasized the importance of the of the RWGS reaction on dry reforming.

Another theory has been proposed by Bradford and Vannice in 1996, who identified the RWGS to be vital for the mechanism. In their network the CO_2 does not participate in the reforming mechanism directly, but serves as an oxygen donor that produces surface bound hydroxyl groups. These OH* groups subsequently react with CH_x* species to form intermediate CH_xO* that subsequently decompose into adsorbed CO* and H* [34].

$CH_4 + *$	$\rightleftharpoons^{+}$	$CH_x* + \left(\frac{4-x}{2}\right) H_2$	Step (6)
$CO_2 + *$	$\Leftrightarrow$	CO_2*	Step (7)
$H_2 + 2*$	$\Leftrightarrow$	$2\ H*$	Step (8)
$CO_2* + H*$	$\Leftrightarrow$	$CO* + OH*$	Step (9)
$OH* + H*$	$\Leftrightarrow$	$H_2O + 2*$	Step (10)
$CH_x* + OH*$	$\Leftrightarrow$	$CH_xO* + H*$	Step (11)
CH_xO*	$\rightarrow$	$CO* + \left(\frac{x}{2}\right) H_2$	Step (12)
$CO*$	$\Leftrightarrow$	$CO + *$	Step (13)

The rate equation derived from this network can be denoted as

$$r = \frac{a p_{CH_4} p_{CO_2}}{b p_{CO} {p_{H_2}}^{(4-x)/2} + (1 + c p_{CH_4}) p_{CO_2}} \tag{1-12}$$

These examples highlight the broad range of possible equations for difference catalytic systems and experimental conditions. Therefore, one can find numerous different rate equations in literature and a summary is listed in table 1-2.

Table 1-2 Proposed rate equations for steam and dry reforming of methane [10]

Model	Catalyst System	References
$r = \frac{k p_{CH_4}}{1 + a\left(\frac{p_{H_2O}}{p_{H_2}}\right) + b p_{CO}}$	Ni foil	[28, 29]
$r = k p_{CH_4}$	Ni/Kieselgur Ni/MgO	[32, 35]
$r = \frac{k\sqrt{K_1 K_2 p_{CO_2} p_{CH_4}}}{(1 + \sqrt{K_1 p_{CO_2}} + \sqrt{K_2 p_{CH_4}})^2}$	Ni/Al_2O_3 Ni/CaO-Al_2O_3 Ni/SiO_2	[36, 37]
$r = \frac{a p_{CH_4} p_{CO_2}^2}{(p_{CO_2} + b p_{CO_2}^2 + p_{CH_4})^2}$	Ni/Al_2O_3 Ni/CaO-Al_2O_3	[38]
$r = \frac{a p_{CH_4} p}{b p_{CO} {p_{H_2}}^{(4-x)/2} + (1 + c p_{CH_4}) p_{CO_2}}$	Ni/MgO Ni/TiO_2	[34]

While our explicit examples list the adsorption and kinetic parameters, others lack this important information and should therefore be handled with care [36-38]. Nevertheless, the large number of publications on the reaction mechanism clarifies the importance of further detailed discussion on this topic.

Huang et al. postulated the formation of CO from H_2 and CO_2 to occur only at steps and kinks of the metal [39] while there is a broad range of DFT calculations showing the transition states of CH_4 adsorption and dissociation on ideal, flat surfaces [40-42]. Exposed sites, like edges and steps are usually energetically favored for reactions over higher coordinated sites in flat planes. Thus, it is very easy to accept the hypothesis of an easier activation of the C-H bond at such exposed sites. A detailed theoretical work on the differences between plane surfaces and kinks has been published by Wang et al. [43]. They deduced that the carbon formation is more difficult in flat areas than at steps due to more facile C-H oxidation in parallel with less CO decomposition. In addition, they provided evidence for the self-induction of carbon deposition as Ni carbide easier forms coke than carbon free surfaces. This indicates that an already partially covered surface forms more carbon than a free one.

Another issue under discussion is the localization and nature of the active centers of DRM. While the references mentioned above used the same active center for all surface reactions, others found that the C-H cleavage occurs on the metal and the CO_2 is activated at the oxide support [17]. To account for the importance of this issue, the influence of the support will be discussed in a section 1.6.3, individually.

Furthermore, the degree of de-hydrogenation of the hydrocarbons during the reaction must be addressed. In other words: Does surface carbon directly participate in the reforming and what role does it play? It is likely that surface carbon participates to some extent in the reaction but its reactivity varies with the gas phase above the surface. Most of the published models irreversibly decompose CH_4 into adsorbed C* and H_2 (or H*, which immediately re-combines and desorbs). Subsequently, the surface carbon gets re-activated by the O* or OH* supplied from CO_2 [6, 9, 32, 33, 44]. The fact that carbon deposition does not deactivate the catalyst (see chapter 1.4) is an affirmation to this theory. In addition, the energy barrier of the C-H bond cleavage in CH_4 is high than those in CH_3*, CH_2* and CH*. This supports the theory of a complete dehydrogenation of CH_x* species as part of the reforming reaction. A mechanistic and kinetic discussion under conditions very close to technical applications will be one main part of this thesis (chapter 1).

The effective carbon affinity varies with the employed materials. Hence, one can imagine how important the elemental composition of the used catalyst is. In the next section the aspects of the various possible catalytic materials will be discussed especially with respect to their stability against coking.

1.6 Catalysts

1.6.1 Noble metal catalysts

Most noble metal catalysts in the laboratory scale are prepared by impregnation of oxide supports with precursor substances and subsequent calcination in a stream of synthetic air. To transform the materials into their active form before reaction the catalyst is usually reduced in a stream of H_2 (often diluted in an inert gas like N_2 or Ar) [17, 27, 45].

All group VIII metals (with an exception for Os) have already been investigated in DRM over various support and Bradford et al. list the activity of a broad variety of those catalysts reported in literature [10]. They reported e.g. TOF´s for CH_4 that vary from 0.03 sec^{-1} Pt/MgO to 2.3 sec^{-1} in Pt/TiO_2 and energies of activation ranging from 62 to 305 kcal/mol in various Pt materials. Consequently, it seems to be very difficult to predict the activity of specific catalytic materials. Rostrup-Nielsen et al. and Kikuchi et al. published a sequence of activity in the noble metals to be Ru ≥ Rh > Ir, > Pt ≥ Pd [9, 46] while Iglesia et al. postulated exact reverse results some years later. The sequence they obtained for the DRM activity was Pd > Pt > Ir > Ru, Rh at similar conditions as the former [44]. Jones et al. combined first principal calculations with experimental data to resolve this discrepancy and found a temperature dependence of the rate determining step on the reaction temperature. At low temperatures the CO activation is the RDS while heating to temperatures near 1000 K the mechanism shifts to C-H activation as the kinetically relevant step. They refer this difference in experimental conditions to be a possible reason for the inversion of reactivity as no other discrepancies of the Iglesia data from the results of Rostrup-Nielsen, Kikuchi or Qin were found by the authors. Something Jones and Iglesia both found, is that the activity of the noble metal catalysts is directly dependent on the dispersion of the active metal [44, 47].

All of these groups found Ni to be comparably active in the reforming reaction as the noble metals, which makes this element an interesting alternative to the very precious other metals. The next section will explain the chances and drawbacks of Ni as supplement for noble metals in DRM.

1.6.2 Ni catalysts

Ni is well known for its ability to activate C-H bonds and its affinity to form stable Ni-C bonds. While the first characteristic is mandatory to transform CH_4 over a Ni surface, the latter can cause coking (see section 1.4). One way to overcome this drawback is a sophisticated synthesis of suitable materials that can withstand carbon deposition because of very defined structural properties. Many different synthesis routes have been proposed to find Ni materials that suppress carbon deposition effectively, e.g. surfactant supported synthesis to define the shape of the support [48], carbon itself as supporting material [49], Ni in catalytically active membranes to separate reactants and products from one another [50] or D-optimal designs to identify the best material composition already before synthesis [24, 51] to name some of the extraordinary routes. Unfortunately, up to now all of these methods are more of scientific relevance but did not make it to a technical upscale.

Like for the noble metals, the standard synthesis route for Ni catalyst is the impregnation of metal-precursors, like nitrates or acetates, with subsequent drying and calcination to obtain the oxide as-synthesized material. The active form of Ni in reforming is the Ni^0, thus the metal needs to be pretreated by reduction (usually above 800 K) before the reforming process [52-57]. In order to thermodynamically reduce the tendency to carbon deposition, very high temperatures are maintained in reforming reactors. The Tamman-temperature of Ni is at 863 K [58], which means that the mobility of the Ni particles on the supported surface usually is high. As a consequence, sintering and the buildup of large arrays of Ni on the surface can be observed. This is disadvantageous for several reasons: 1) Sintering leads to a loss of active surface as more and more Ni atoms disappear into the particle bulk. 2) Materials that have been produced with very high dispersions and low particle sizes (e.g. to overcome the production of CNT´s, see 1.4) lose these characteristics in the course of the reaction. 3) Constant changes in the catalysts structure lead to varying activities of the materials and thus complicate the comparability of the catalysts among one another other.

Both, the carbon affinity and the sintering, can be tuned by the use of bi-metallic materials that upgrade the thermal stability and the carbon withstanding of the original Ni material by adding a second metal. These materials will be discussed in the next section.

1.6.3 Supports

Ideally, the support of a catalyst not only provides a large surface area, but also prevents sintering of the metal particles, thus, maximizing the amount of active centers. The supports most investigated in dry reforming are TiO_2 [21, 59], Al_2O_3 [20, 60-62] and ZrO_2 [15, 19, 63-67]. Next to these common materials some more special arrangements, like ordered mesoporous materials [68-70], solid solutions [71] or carbon [72], have been tested. Additionally, hexaaluminates, which will be discussed in detail later, attracted a lot of interest [73-75].

Most of these materials cannot be taken as inert under dry reforming conditions – especially at temperatures above 1073 K. This leads to the assumption that the support itself participates in the reforming. Lercher et al. could provide evidence that the catalyst support also plays a remarkable role for the stabilization against coking. The stability increases in the in the order of $Pt/Al_2O_3 < Pt/TiO_2 < Pt/ZrO_2$ with substantial differences between the materials because of their differences in Lewis-acid site concentration [17, 76, 77]. Lewis acid sites activate C-H bonds, which makes the decomposition of hydrocarbons faster than the re-activation of carbon with oxygen containing species (CO*, OH*, O*). Therdthianwong et al. published similar results as they upgraded Al_2O_3 supported Ni catalysts with ZrO_2 and received a better coking stability in the doped samples [78]. Pompeo et al. concluded from their experiments with α-Al_2O_3, ZrO_2 and α-Al_2O_3-ZrO_2 that the ZrO_2 helps activating CO_2 on the surface and hence enhances the carbon removal [79].

1.7 Hexaaluminates

Hexaaluminates are materials with high-temperature stability that crystallize in a layered form [80-82]. Spinel planes are separated from one another by so called “mirror” or “conduction” layers, as can be observed in Figure 1-7. Those mirror planes, incorporate large cations like La^{3+}, Sr^{2+} or Ba^{2+} and render the crystal structure to be very temperature-stable. Depending on the mirror-plane-cation hexaaluminates crystallize either in a magnetoplumbite (e.g. La^{3+} or Sr^{2+}) or a β-alumina (e.g. Ba^{2+}) structure [83]. Both are formed from α-Al_2O_3, the high temperature configuration of Al_2O_3, so a calcination at temperatures above 1372 K needs to be employed in the synthesis of hexaaluminates. In order to obtain phase pure structures even temperatures above 1473 K have to be employed [84]. During the high temperature treatment, the materials lose their porosity and inner surface and the outer surface usually sinters to values below 30 m²/g.

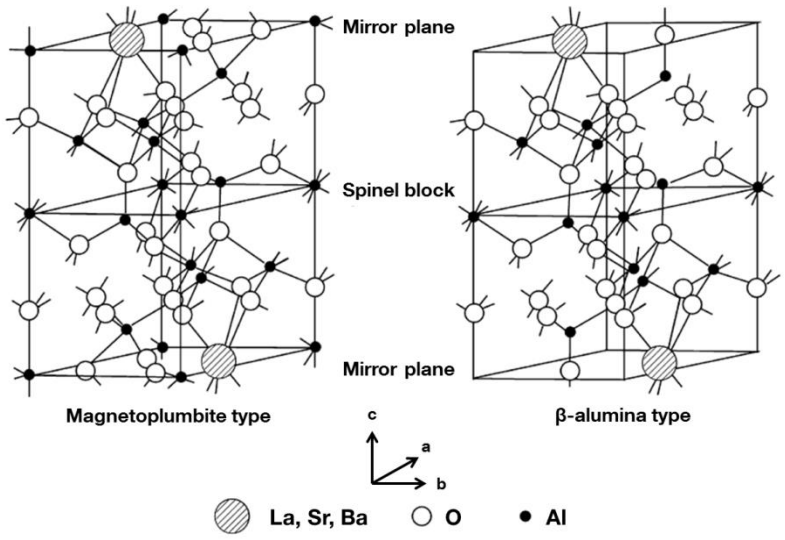

Figure 1-7 Unit cell of the two possible configurations of the hexaaluminate crystal [85].

Besides other application like coatings [16], nuclear waste storage [18] or as crystals for fluorescence lasers [56], hexaaluminates have attracted interest as supports for high temperature catalysis, especially in partial and total oxidation [85-91] and CO_2-CH_4 reforming [73-75, 92].

Gardner et al. performed extensive work on the structure of the crystals and possibilities to influence it. They could show that increasing Ni loadings lead to a shrinking unit cell along the c axis. The Ni^{2+} usually substitutes tetrahedrally coordinated Al^{3+} in order to reduce strains in the lattice that originate from the higher charge. As a consequence the Ni-O bond in the spinel of the hexaaluminate is stronger than in bulk NiO [93].

Additionally, the authors could show that the mirror cation does not only influence the structure of the crystal, but also its reactivity (e.g. in the partial oxidation of *n*-tetradecane). At the same loading of Ni, the stability against carbon deposition decreased in the order $BaNi_{0.4}Al_{11.6}O_{19-\delta}$ >> $SrNi_{0.4}Al_{11.6}O_{19-\delta}$ > $LaNi_{0.4}Al_{11.6}O_{19-\delta}$. The authors concluded that this behavior is a result of the varying anchoring of the Ni in the lattice by the counter ions and hence different Ni-hydrocarbon interactions [85].

1.8 Recycle and single pass reaction setup

For the experiments a setup was built that can be used in a single run mode and a recycle mode. The flow scheme of the system can be found in Figure 1-8. Gas supply was established with *Bronkhorst EL-FLOW* mass flow controllers for the gases CO_2, CH_4, H_2, N_2 and synthetic air which were provided by *Westfalen* and used without further purification. Water addition was done from a pressurized container by a *Bronkhorst LIQUI-FLOW* mass flow controller into heated capillary for controlled vaporization. The reactor itself was a stainless steel tube ($Ø_{in}$ = 8 mm, $Ø_{out}$ = 10 mm), heated by a *Watlow* ceramic fiber heater with custom made stainless steel liners for a uniform distribution of heat over the catalyst bed. The samples were fixed into an alumina tube ($Ø_{in}$ = 6 mm, $Ø_{out}$ = 7 mm) by two layers of quartz wool and this tube was then inserted into the steel reactor and sealed on the two endings to prevent lateral gas flow along the reactor walls.

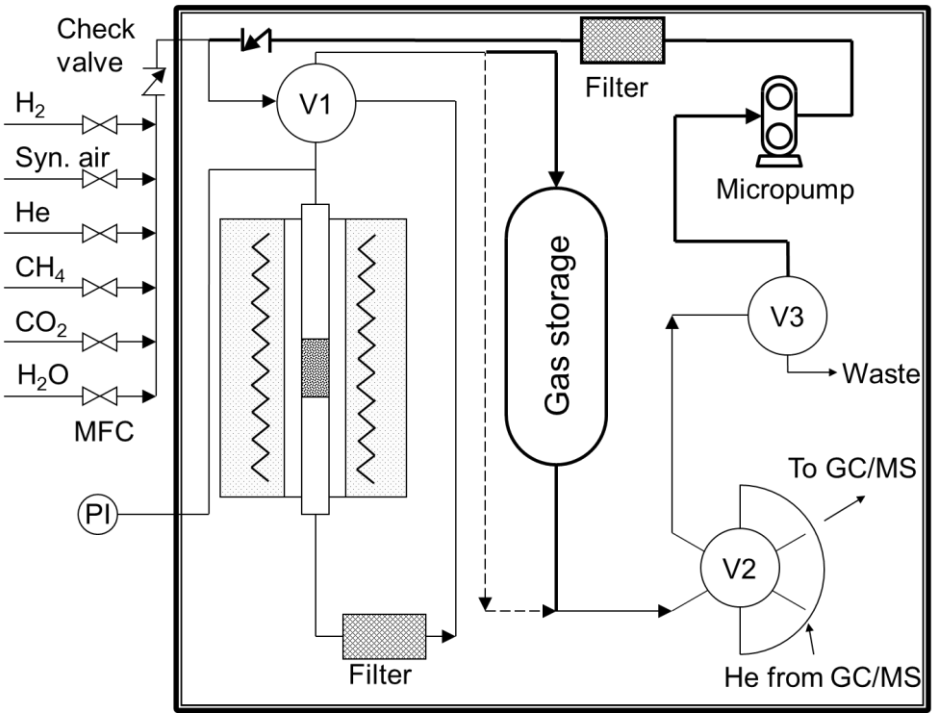

Figure 1-8 Flow sheet of the reaction setup with two different flow modes: recycle mode (bold) and single pass mode (dashed). Lines and components used in both methods are drawn in simple form.

Gas analysis was conducted with a combined *Shimadzu GC/MS-QP-2010 / GC-2010 Plus* system equipped with a molsieve and a HQ-plot column and a TCD, an FID and a quadrupole MS as detectors. Depending on the required mode of the system the gasses from the reactor were either led to waste or recycled back into the reactor (setting of valve V3 in Figure 1-8). For recycling the gasses were led to an *Ismatec Gear pump Reglo-ZS Digital* equipped with a suction shoe style pump head. The reactor oven, the

gas storage, the sample- and the recycle/waste valves as well as the micropump for recycling the gasses are located within a heat box and kept at 453 K to prevent water condensation during the reaction. For the recycle mode a gas storage vessel was inserted into the setup directly behind the reactor that increases the overall gas volume of the setup in this mode to 331 ml ($V_{sys)}$. Thus differential conversions could be maintained per cycle with the chance to observe very high conversion levels in the curse of the reaction. This feature of the setup was used during isotope labeling experiments in order to track the isotope composition of the components during the reaction. To measure reaction orders and temperature influences on the reaction kinetics the reactor was set to the single pass mode, which was capable of an easy and quick adaption of a broad set of conditions. Temperatures from 873 K to 1123 K ($T_{reactor}$) were applied with pressures up to 10 bars and a maximum flow of 260 ml_n/min.

In the recycle experiments, the gas chromatograph could provide the mole fractions of the individual gasses, x_i. These were multiplied with the system pressure p_{sys} at the time of measurement to obtain the partial pressures, p_i:

$$p_i = x_i p_{sys} \tag{1-13}$$

The partial pressure can be applied in the ideal gas law, which then gives the amount of the individual substance in the system (in mol).

$$p_i V_{sys} = n_i R T_{Reactor} \rightarrow n_i = \frac{p_i V_{sys}}{R T_{Reactor}} \tag{1-14}$$

Knowing the amount of every substance, one can calculate the elemental balance for C, H and O, which gives information on possible leakage or coke deposition during the reaction:

$$n_c = n_{CO_2} + n_{CH_4} + n_{CO} \tag{1-15}$$

$$n_O = 2n_{CO_2} + n_{H_2O} + n_{CO} \tag{1-16}$$

$$n_H = 4n_{CH_4} + 2n_{H_2} + 2n_{H_2O} \tag{1-17}$$

Especially from the ratios n_C/n_H, n_C/n_O and n_H/n_O it is easily visible if the carbon balance is closed or if carbon deactivation during the recycle experiments occurred. If so, the

ratio n_H/n_O remains constant, while the other two decrease constantly. In case the two ratios do not decline in parallel, one can conclude that the deposed carbon is hydrogen rich or oxygen and the respective element also disappears from the gas phase into the deposit. In the recycle experiments, the conversion is calculated from the corrected partial pressures of the gasses:

$$\mathrm{X_i} = \frac{\mathrm{p_{i,o}} - \mathrm{p_i}}{\mathrm{p_{i,0}}} \tag{1-18}$$

In the single pass experiments, the first thing to do was to correct the flow in the reactor ($\mathrm{x_i}$) by the volume expansion during the reaction to obtain the real flow ($x_{\mathrm{i,corr}}$). Therefore, the initial mole fraction of N_2 ($x_{N_{2,0}}$) was compared at every measurement with the current mole fraction of N_2 ($x_{N_{2,t}}$) and this ratio was multiplied with the set flow:

$$\mathbf{x_{i,corr}} = \mathbf{x_i}\frac{\mathbf{x_{N_{2,0}}}}{\mathbf{x_{N_{2,t}}}} \tag{1-19}$$

From the corrected mole fraction, the conversion of the component (X_i) could be calculated:

$$\mathrm{X_i} = \frac{\mathrm{x_{i,o}} - \mathrm{x_{i,corr}}}{\mathrm{x_{i,0}}} \tag{1-20}$$

To finally calculate turnover frequency (TOF), which equals the macroscopic conversion rate of substance I, r_i, from the conversion we need the flow per substance ($\dot{V}_I$), which we obtain from the settings of the flow meter.

$$\mathrm{TOF} = \frac{\mathrm{X_i}\dot{\mathrm{V}}_\mathrm{I}}{\mathrm{n_{Ni}}} = \mathrm{r}_i \tag{1-21}$$

Here n_{Ni} is the amount of active Ni centers available for reaction. These are the rudimentary calculations on which all further evaluation of results will be based. If any further calculations are necessary in particular, they will be explained in the individual chapters.

1.9 Scope of this thesis

The goal of this work is to present a bottom up approach to a consistent mechanistic picture of the dry reforming of methane. This employs the identification of the optimal catalyst, the investigation of its deactivation behavior and a kinetical description of the material. The work will be divided into three major parts:

Catalysts synthesis and characterization

The goal of the first chapter is to find the optimal composition for a hexaaluminate catalyst. This is done in two steps: 1) A ranking is made of the three hexaaluminate counter ions La^{3+}, Ba^{2+} and Sr^{2+} with respect to their influence on the optimal performance in dry reforming. The evaluation will be made based on activity and stability. 2) The LaNi-hexaaluminate synthesis route is optimized. Included into this section will be a comparative investigation on the physical and chemical properties of the materials synthesized by two pathways. The influence of the addition of polyethylene glycol (PEG) during the synthesis on the phase purity will be analyzed by XRD, SEM, TEM and sorption analysis. Finally, the differences in reactivity and the resistance against coking of the materials in dry reforming will be highlighted.

The carbon deposition as a function of the active metal – a comparison between Ni and Pt

Once the most active and stable material has been identified this catalyst will be investigated further in recycle experiments and the results of will be benchmarked against a Pt/ZrO_2 catalyst. Isotope labelling experiments, TPO and numeric calculations will reveal the similarities and especially the differences between the two materials. The importance of re-gasification of surface carbon for the stability is investigated in detail.

Kinetic and mechanistic model of the dry reforming of methane at elevated pressures

Finally, the kinetic behavior of the Ni material is examined and a description of the reforming mechanism is derived from the experimental results. The influence of the partial pressures of the reactants and the products are addressed and mathematical expressions for the surface species that can describe the kinetic behavior of the catalyst are presented. The importance of the RWGS, as the major side reaction of DRM, is highlighted.

1.10 Literature

[1] EIA, www.eia.gov/dnav/ng/hist/rngwhhda.htm, 2016.
[2] H. Andruleit, A. Bahr, C. Bönnemann, J. Erbacher, Bundeanstalt für Geowissenschaften und Rohstoffe (BGR) Hannover, 2012.
[3] M.-S. Fan, A.Z. Abdullah, S. Bhatia, ChemCatChem, 1 (2009) 192.
[4] W. Chu, W. Yang, L. Lin, Appl. Catal., A, 235 (2002) 39.
[5] K. Takehira, T. Shishido, P. Wang, T. Kosaka, K. Takaki, J. Catal., 221 (2004) 43.
[6] J. Wei, E. Iglesia, J. Catal., 225 (2004) 116.
[7] R.-N.J. R., S. Jens, R.J. K., Academic Press, New York, NY, ETATS-UNIS, 2002.
[8] E. Schwab, A. Milanov, S.A. Schunk, A. Behrens, N. Schödel, Chem. Ing. Tech., 87 (2015) 347.
[9] J.R. Rostrupnielsen, J.H.B. Hansen, J. Catal., 144 (1993) 38.
[10] M.C.J. Bradford, M.A. Vannice, Cat. Rev. - Sci. Eng., 41 (1999) 1.
[11] W. Wintruff, Kristall und Technik, 9 (1974) 391.
[12] L.C.S. Kahle, T. Roussière, L. Maier, K. Herrera Delgado, G. Wasserschaff, S.A. Schunk, O. Deutschmann, Ind. & Eng. Chem. Res., 52 (2013) 11920.
[13] J.R. Rostrup-Nielsen, T. Rostrup-Nielsen, Cattech, 6 (2002) 150.
[14] W. Hally, J.H. Bitter, K. Seshan, J.A. Lercher, J.R.H. Ross, in: B. Delmon, G.F. Froment (Eds.) Catalyst Deactivation, 1994, pp. 167.
[15] J.A. Lercher, J.H. Bitter, W. Hally, W. Niessen, K. Seshan, in: W.N.D.E.I. Joe W. Hightower, T.B. Alexis (Eds.) Stud. Surf. Sci. Catal., Elsevier1996, pp. 463.
[16] J. Zhang, H. Wang, A.K. Dalai, Appl. Catal., A, 339 (2008) 121.
[17] J.H. Bitter, W. Hally, K. Seshan, J.G. vanOmmen, J.A. Lercher, Catal. Today, 29 (1996) 349.
[18] P. Djinović, I.G. Osojnik Črnivec, B. Erjavec, A. Pintar, Appl. Catal., B, 125 (2012) 259.
[19] A. Horvárth, G. Stefler, O. Geszti, A. Kienneman, A. Pietraszek, L. Guczi, Catal. Today, 169 (2011) 102.
[20] D. San-José-Alonso, J. Juan-Juan, M.J. Illán-Gómez, M.C. Román-Martínez, Appl. Catal., A, 371 (2009) 54.
[21] K. Takanabe, K. Nagaoka, K. Nariai, K.-i. Aika, J. Catal., 232 (2005) 268.
[22] B. Steinhauer, M.R. Kasireddy, J. Radnik, A. Martin, Appl. Catal., A, 366 (2009) 333.
[23] S.R. de Miguel, I.M.J. Vilella, S.P. Maina, D. San José-Alonso, M.C. Román-Martínez, M.J. Illán-Gómez, Appl. Catal., A.
[24] S. Corthals, J. Van Nederkassel, H. De Winne, J. Geboers, P. Jacobs, B. Sels, Appl. Catal., B, 105 (2011) 263.
[25] D. Lee, P. Hacarlioglu, S.T. Oyama, Top. Catal., 29 (2004) 45.
[26] S.T. Oyama, P. Hacarlioglu, Y. Gu, D. Lee, Int. J. Hydrogen Energy, 37 (2012) 10444.
[27] F.M. Michael, F.M. Wilhelm, Angew. Chem., 106 (1994) 1738.
[28] N. Bodrov, L. Apel'Baum, M. Temkin, Kinet. Katal, 5 (1964) 696.
[29] I. Bodrov, L. Apel'baum, Kinet. Catal, 8 (1967) 379.
[30] L. Maier, B. Schädel, K. Herrera Delgado, S. Tischer, O. Deutschmann, Top. Catal., 54 (2011) 845.
[31] P.E.D. Morgan, D.R. Clarke, C.M. Jantzen, A.B. Barker, J. Am. Ceram. Soc., 64 (1981) 249.
[32] J. Wei, E. Iglesia, J. Catal., 224 (2004) 370.
[33] A. Yamaguchi, E. Iglesia, J. Catal., 274 (2010) 52.
[34] M.C.J. Bradford, M.A. Vannice, Appl. Catal., A, 142 (1996) 97.
[35] W. Akers, D. Camp, AlChE J., 1 (1955) 471.
[36] T. Horiuchi, K. Sakuma, T. Fukui, Y. Kubo, T. Osaki, T. Mori, Appl. Catal., A, 144 (1996) 111.

[37] T. Osaki, T. Horiuchi, K. Suzuki, T. Mori, Appl. Catal., A, 155 (1997) 229.
[38] Z.L. Zhang, X.E. Verykios, Catal. Today, 21 (1994) 589.
[39] M. Huang, S. Kaliaguine, S. Suppiah, Appl. Surf. Sci., 90 (1995) 393.
[40] S.G. Wang, D.B. Cao, Y.W. Li, J. Wang, H. Jiao, J. Phys. Chem. B, 110 (2006) 9976.
[41] Y.-A. Zhu, D. Chen, X.-G. Zhou, W.-K. Yuan, Catal. Today, 148 (2009) 260.
[42] S.-G. Wang, D.-B. Cao, Y.-W. Li, J. Wang, H. Jiao, Surf. Sci., 600 (2006) 3226.
[43] Z. Wang, X.M. Cao, J. Zhu, P. Hu, J. Catal., 311 (2014) 469.
[44] J. Wei, E. Iglesia, J. Phys. Chem. B, 108 (2004) 4094.
[45] B. Quiroga, M. Martha, C. Luna, A. Eduardo, Ind. & Eng. Chem. Res., 46 (2007) 5265.
[46] E. Kikuchi, S. Tanaka, Y. Yamazaki, Y. Morita, Bulletin of The Japan Petroleum Institute, 16 (1974) 95.
[47] G. Jones, J.G. Jakobsen, S.S. Shim, J. Kleis, M.P. Andersson, J. Rossmeisl, F. Abild-Pedersen, T. Bligaard, S. Helveg, B. Hinnemann, J.R. Rostrup-Nielsen, I. Chorkendorff, J. Sehested, J.K. Nørskov, J. Catal., 259 (2008) 147.
[48] Y. Zhang, Q. Li, H. Li, Y. Cheng, J. Zhang, X. Cao, J. Cryst. Growth, 310 (2008) 3884.
[49] B. Fidalgo, J.A. Menéndez, Fuel Process. Technol., 95 55.
[50] S.-K. Ryi, J.-S. Park, D.-K. Kim, T.-H. Kim, S.-H. Kim, Journal of Membrane Science, 339 (2009) 189.
[51] S. Corthals, T. Witvrouwen, P. Jacobs, B. Sels, Catal. Today, 159 12.
[52] I.P. Silverwood, N.G. Hamilton, J.Z. Staniforth, C.J. Laycock, S.F. Parker, R.M. Ormerod, D. Lennon, Catal. Today, 155 319.
[53] I.P. Silverwood, N.G. Hamilton, C.J. Laycock, J.Z. Staniforth, R.M. Ormerod, C.D. Frost, S.F. Parker, D. Lennon, Phys. Chem. Chem. Phys., 12 (2010) 3102.
[54] J. Juan-Juan, M.C. Román-Martínez, M.J. Illán-Gómez, Appl. Catal., A, 301 (2006) 9.
[55] U. Olsbye, T. Wurzel, L. Mleczko, Ind. & Eng. Chem. Res., 36 (1997) 5180.
[56] D. Baudouin, U. Rodemerck, F. Krumeich, A.d. Mallmann, K.C. Szeto, H. Ménard, L. Veyre, J.-P. Candy, P.B. Webb, C. Thieuleux, C. Copéret, J. Catal., 297 (2013) 27.
[57] V.M. Gonzalez-Delacruz, R. Pereñiguez, F. Ternero, J.P. Holgado, A. Caballero, ACS Catal., 1 (2011) 82.
[58] J.A. Moulijn, A.E. van Diepen, F. Kapteijn, Appl. Catal., A, 212 (2001) 3.
[59] K. Takanabe, K. Nagaoka, K. Nariai, K.-i. Aika, J. Catal., 230 (2005) 75.
[60] N. Salhi, A. Boulahouache, C. Petit, A. Kiennemann, C. Rabia, J. Soc. Alger. Chim., 20 (2010) 121.
[61] Z. Hou, O. Yokota, T. Tanaka, T. Yashima, Appl. Catal., A, 253 (2003) 381.
[62] A.I. Tsyganok, M. Inaba, T. Tsunoda, K. Uchida, K. Suzuki, K. Takehira, T. Hayakawa, Appl. Catal., A, 292 (2005) 328.
[63] H.-S. Roh, H.S. Potdar, K.-W. Jun, Catal. Today, 93-95 (2004) 39.
[64] H.-S. Roh, K.Y. Koo, W.L. Yoon, Catal. Today, 146 (2009) 71.
[65] J.-S. Chang, D.-Y. Hong, X. Li, S.-E. Park, Catal. Today, 115 (2006) 186.
[66] X. Li, J.-S. Chang, E. Lee, S.-E. Park, React. Kinet. Catal. Lett., 67 (1999) 383.
[67] X. Li, J.-S. Chang, S.-E. Park, React. Kinet. Catal. Lett., 67 (1999) 375.
[68] W. Shen, H. Momoi, K. Komatsubara, T. Saito, A. Yoshida, S. Naito, Catal. Today, 171 (2011) 150.
[69] K. Wang, X. Li, S. Ji, B. Huang, C. Li, ChemSusChem, 1 (2008) 527.
[70] C. Daza, O. Gamba, Y. Hernández, M. Centeno, F. Mondragón, S. Moreno, R. Molina, Catal. Lett., 141 (2011) 1037.
[71] V.R. Choudhary, A.S. Mamman, Journal of Chemical Technology & Biotechnology, 73 (1998) 345.
[72] B. Fidalgo, L. Zubizarreta, J.M. Bermúdez, A. Arenillas, J.A. Menéndez, Fuel Process. Technol., 91 (2010) 765.

[73] Z. Xu, M. Zhen, Y. Bi, K. Zhen, Appl. Catal., A, 198 (2000) 267.
[74] K. Ikkour, D. Sellam, A. Kiennemann, S. Tezkratt, O. Cherifi, Catal. Lett., 132 (2009) 213.
[75] Z. Xu, M. Zhen, Y. Bi, K. Zhen, Catal. Lett., 64 (2000) 157.
[76] Nagaoka Katsutoshi, Seshan Kulathuiyer, Lercher Johannes A., A. Ken-ichi, Catal. Lett., 70 (2000) 109.
[77] J.H. Bitter, K. Seshan, J.A. Lercher, J. Catal., 183 (1999) 336.
[78] S. Therdthianwong, C. Siangchin, A. Therdthianwong, Fuel Process. Technol., 89 (2008) 160.
[79] F. Pompeo, N.N. Nichio, O.A. Ferretti, D. Resasco, Int. J. Hydrogen Energy, 30 (2005) 1399.
[80] M. Gasperin, M.C. Saine, A. Kahn, F. Laville, A.M. Lejus, J. Solid State Chem., 54 (1984) 61.
[81] K.E. M. Machida, H. Arai, Bull. Chem. Soc. Jpn, 61 (1988) 3659.
[82] M. Machida, K. Eguchi, H. Arai, J. Catal., 123 (1990) 477.
[83] N. Iyi, S. Takekawa, S. Kimura, J. Solid State Chem., 83 (1989) 8.
[84] T.H. Gardner, J.J. Spivey, E.L. Kugler, D. Pakhare, Appl. Catal., A, 455 (2013) 129.
[85] T.H. Gardner, D. Shekhawat, D.A. Berry, M.W. Smith, M. Salazar, E.L. Kugler, Appl. Catal., A, 323 (2007) 1.
[86] G. Groppi, M. Bellotto, C. Cristiam, P. Forzatti, P.L. Villa, Appl. Catal., A, 104 (1993) 101.
[87] G. Groppi, C. Cristiani, P. Forzatti, Appl. Catal., B, 35 (2001) 137.
[88] M.H. Han, Y.S. Ahn, S.K. Kim, S.K. Shon, S.K. Kang, S.J. Cho, Mater. Sci. Eng., A, 302 (2001) 286.
[89] J. Wang, Z. Tian, J. Xu, Y. Xu, Z. Xu, L. Lin, Catal. Today, 83 (2003) 213.
[90] E.E. Svensson, M. Boutonnet, S.G. Järås, Appl. Catal., B, 84 (2008) 241.
[91] F. Yin, S. Ji, P. Wu, F. Zhao, C. Li, J. Mol. Catal. A: Chem., 294 (2008) 27.
[92] J. Wang, Y. Liu, T. Cheng, W. Li, Y. Bi, K. Zhen, Appl. Catal., A, 250 (2003) 13.
[93] T.H. Gardner, J.J. Spivey, E.L. Kugler, A. Campos, J.C. Hissam, A.D. Roy, Journal of Physical Chemistry C, 114 (2010) 7888.

2 Synthesis and Characterization of Dry Reforming Catalysts

Firstly, the influence of the counter ions Ba^{2+}, Sr^{2+} and La^{3+} is compared in Ni-hexaaluminates. La^{3+} provides the most stable activity, though it has reduced activity compared to the other materials. Higher calcination temperatures negatively affect the activity and stability.

Secondly, La-containing Ni-hexaaluminate materials were synthesized by re-crystallization and a polyethylene glycol supported route. Phase composition, stability against reduction and performance in the dry reforming reaction were tested revealing significant differences. The PEG supported synthesis produces much more hexaaluminate phase in the as synthesized materials and increases the material´s stability as well in the reduction as under the reforming conditions. Simultaneously the effect of active metal content in the materials was investigated, revealing an optimum in composition and performance at 5 wt.-% of Ni.

2.1 Introduction

One major drawback that prevented successful application of dry reforming up to date is the severe coke deposition due to the high carbon content in the gas phase. Noble metal catalysts are less prone to coking and but they are usually too expensive to serve as active metal in large scale processes [1, 2]. Ni has been under investigation for years as active metal in DRM, because of its well-known ability to activate C-H bonds. Numerous concepts have been proposed to diminish the deposition of carbon on Ni while simultaneously preserving a high activity in dry reforming, like the right choice of support [3-5], a variety of dopants [6-8] or mixed oxides [9-11]. Bitter et al. proposed the particle size of the active metal to be the key to stable base metal catalysts. They presented a series of Ni catalyst with varying particle sizes and at a diameter of the particles that was smaller than 2 nm the materials could prevent coking and simultaneously maintained a decent activity [12]. Thus, the state of Ni present on the catalysts appears to be utmost importance for a stable operation in DRM and one way to tailor the surface Ni is the right choice of the support. Temperature stability is another mandatory property any technically applied catalyst has to provide in order to maintain constant results over a long time. Hexaaluminates (HA) have been proven to exhibit both, excellent resistance against thermal stress and the possibility to maintain stable operation of DRM [13, 14]. The crystals consist of two main components: a spinel plane and a stabilizing mirror plane, in to which mono-, di- or trivalent cations are incorporated. There are two main unit cell configurations that differ in the composition of their mirror planes and the general formula: magnetoplumbite and *β*–alumina. Takekawa et al. discussed the dependency of the HA structure on the size and the charge of the cation already in 1989 in detail. They found that all cations need a minimum ionic radius (~1.1 Å) to stabilize the structure, but monovalent ions always form β-alumina while di- and trivalent can stabilize either one of the two possible structures. Such cations with ionic radii between 1.1 Å and 1.33 Å form magnetoplumbite and above this threshold β-alumina will be the stable form. The most commonly used stabilizing agents for the mirror plane are Ba^{2+} (forming β-alumina), Sr^{2+} or La^{3+} (forming magnetoplumbite) [15]. If employed in the synthesis, Ni exchanges with Al in the spinel blocks and can stabilized within the structure. One reason for the increased thermal stability of the structure is, that the ion and charge migration is stronger hindered across these layers than along them.

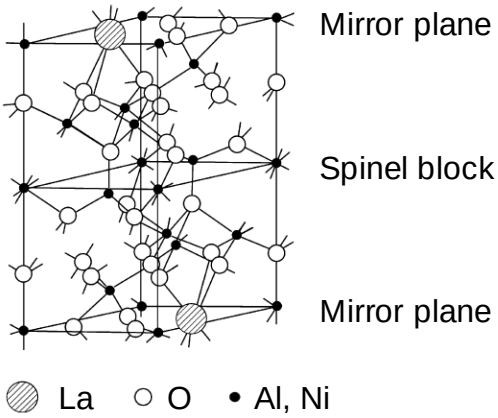

Figure 2-1 Crystal structure of magnetoplumbite employing La^{3+} as counter ion [16]

Gardner et al. investigated the influence of the stabilizing ions extensively with respect to the structure [17] but also to the activity in high energy demanding processes like partial oxidation [18] and reforming [16]. They could provide evidence that the employed materials can withstand the thermal stress of these processes very well and thus provide stable activities over long times on stream. Diverse synthesis methods have been proposed for the production of hexaaluminates and they all have in common that high temperature treatment is a key step in the procedure. The alumina goes through a phase transformation from α- to β-alumina at a temperature of at least 1323 K and then forms the HA phase [13, 18]. Thus, to obtain pure hexaaluminate materials temperatures well above 1323 K need to be employed for several hours, which is very energy demanding. Such preparation methods would be favored that can produce phase-pure HA with less energy input. Thus, the usage of organic components, like polyethylene glycol (PEG) or urea, has been under investigation for years in the synthesis of hexaaluminates [19-21].

In this chapter, an approach will be presented to produce stable hexaaluminate DRM catalysts. The section will be separated in to two parts: Firstly, we will investigate the impact of the counter ions Ba^{2+}, Sr^{2+} and La^{3+} on the activity and coking stability of the catalysts. Subsequently, a second generation of materials will be produced and tested employing the post promising counter ion. Here, two characteristics will be in special focus: The Ni-content and the influence of PEG during the synthesis. Both parameters are tested with respect to their influence on phase composition, reduction stability and behavior in DRM.

2.2 Part 1: Identification of the role of the hexaaluminate counter-ion

This section covers the question, which of the three elements Ba, La or Sr is the ideal counter ion in dry reforming hexaaluminate-catalysts with respect to the optimum of catalytic activity and stability against coke deposition. In addition, the issue of calcination temperature and duration is discussed briefly.

2.2.1 Experimental

2.2.1.1 Spray-drying synthesis

Ni–hexaaluminates were prepared based on the freeze drying preparation route to obtain, at relatively low temperature, a high hexaaluminate phase content with high specific surface area. The nitrate salts of Ni and Ba, La or Sr were dissolved in deionized water in a beaker. The solution was stirred vigorously to obtain a “homogeneous” slurry after the addition of pseudo-boehmite in powder form (Disperal® from Sasol). After 15 min of ageing, the slurry was added dropwise into liquid N_2 under stirring into a dish shaped Dewar flask. The frozen solid was then freeze-dried for 96 h at 243 K under a pressure of 200 Pa in a stainless-steel dish. The resulting precursor was then calcined at the respective temperatures of 1473 K for 2.5 h or 1873 K for 30 h in a muffle furnace under air.

An overview of the samples reported herein together with their structural properties is given in table 2-1.

Table 2-1 Summary of the samples prepared by freeze drying with La, Sr and Ba as counter ions at 1473 K and 1873 K, along with the BET surface and the content of Hexaaluminate phase as given in [22]

Short name	Stoichiometry	Calcination Temp. [K]	Calcination Time [h]	BET surface area [m²/g]	Hexaaluminate phase content [wt.-%]
LaNi1 1600	La1Ni1Al11O19	1873	30	< 0.1	90
LaNi0.5 1600	La1Ni0.5Al11.5O19	1873	30	< 0.1	98
LaNi0.25 1600	La1Ni0.25Al11.75O19	1873	30	< 0.1	98
LaNi1 1200	La1Ni1Al11O19	1473	2.5	8.5	84
LaNi0.5 1200	La1Ni0.5Al11.5O19	1473	2.5	10.8	88
LaNi0.25 1200	La1Ni0.25Al11.75O19	1473	2.5	14.6	89
SrNi1 1200	Sr1Ni1Al11O19	1473	2.5	24.6	83
SrNi0.5 1200	Sr1Ni0.5Al11.5O19	1473	2.5	22.3	81
SrNi0.25 1200	Sr1Ni0.25Al11.7O19	1473	2.5	26.0	80
BaNi1 1200	Ba1Ni1Al11O19	1473	2.5	24.5	73
BaNi0.5 1200	Ba1Ni0.5Al11.5O19	1473	2.5	20.9	93
BaNi0.25 1200	Ba1Ni0.25Al11.75O19	1473	2.5	13.8	87

2.2.1.2 Activity and stability testing

For the catalytic test reactions, 20 mg of the catalyst (500–710 mm) were diluted in SiC (80 mg) of the same size and placed in an aluminium oxide tube of 6 mm inner and 7 mm outer diameter, which was fixed into a stainless-steel reactor of 8 mm inner diameter and sealed on the outside to avoid gas passing between the aluminiumoxide and the steel tubing. Heating was performed under inert gas atmosphere (N_2) and the samples were pre-treated at 1073 K in a stream of 20% H_2 in N_2 for 2 h under atmospheric pressure. Catalytic tests were conducted at 1 MPa with a CH_4/CO_2 ratio of unity and 10 vol-% N_2 was used as an internal standard at a temperature of 1123 K. Gases emerging from the reactor were fully recycled (closed loop) by using a microgear pump (Ismatec) delivering a recycling flow of 100 standard cubic centimetres per minute through gas storage under isochoric operating conditions. The composition of the gas was analysed in a coupled GC/GC–MS system from Shimadzu supplied with an HP-Plot_Q (0.53 mm x 30 m) and a molecular sieve (0.54 mm x 30 m) column for component separation with flame ionization detector, temperature conductivity detector, and Quadrupole MS detection. A description of the recycle system can be found in a later section.

The performance indicators for the comparison of the catalysts are the dry reforming activity and the rate of deactivation. The selected measure for the DRM activity is the total CH_4 conversion after 600 min recycle-runtime. At the end of the experiment reaction approaches thermodynamic equilibrium over most of the catalysts. Therefore, as another parameter established to describe the coke deposition, is the loss in CO molar fraction over time.

2.2.2 Results and discussion

2.2.2.1 Structural properties

All materials, regardless of the counter ion used or the Ni-content, have comparably low surface areas for catalytic materials, which is due to the high calcination temperatures employed. Especially on the LaNix 1600 materials, which were submitted to temperatures of 1873 K for 30 h, the outer surface is essentially unmeasurable (i.e. < 0.1 m^2/g). The extreme calcination procedure causes the outer surface to collapse completely, but it also leads to very pure materials that contain more than 90 wt.-% of hexaaluminate phase. All other materials feature surface areas between 8.5 and 26 m^2/g and hexaaluminate phase contents between 70 and 93 wt.-%. The surface areas in the La^{3+}-hexaaluminates are generally smaller than the ones in the Sr^{2+}- or the Ba^{2+}-containing materials, which might be attributed to the lower charge of the latter ones.

A detailed comparison of the structural properties and a reduction mechanism for such Ni-hexaaluminates has previously been published [22].

2.2.2.2 Dry reforming activity and coke stability

Two independent parameters were defined to compare the catalysts: Catalytic activity of the materials and their stability against coking under such harsh conditions. For a catalyst to provide optimal performance the optimum those individual factors needs to be found. The activity is directly indicated by comparing the CH_4 conversion after 600 min time on stream (see Figure 2-2a) in the recycle reactor system. As can be observed from Figure 2-2b, the mole fraction of CO goes through a maximum and constantly decreases after on. A strong decline in CO mole fraction was always accompanied with a steep coke deposition. Thus, the decrease in mole fraction over time, $\triangle C_{co}/\triangle T$, was a suitable parameter for the carbon deposition.

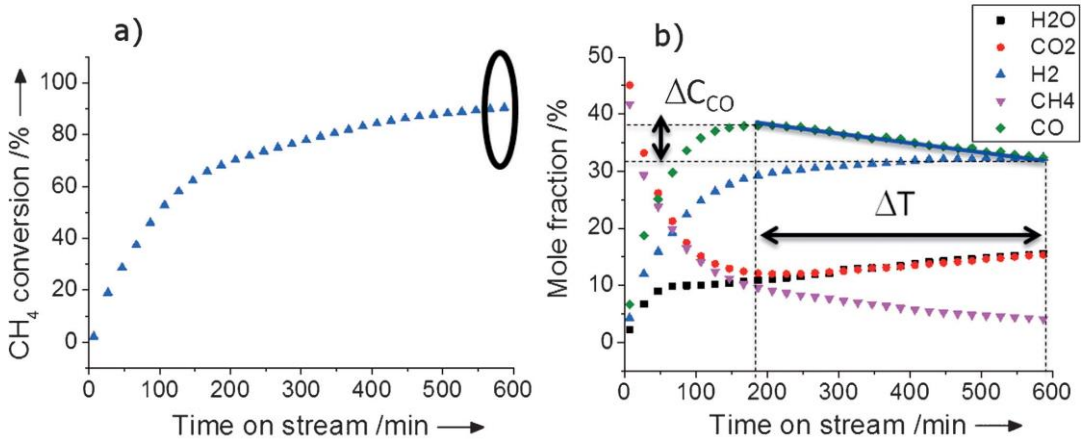

Figure 2-2 Example description of the parameters for activity and coking stability of the catalysts. a) The overall conversion after 600 min recycle-runtime resembles the activity of the samples. b) the coefficient $\triangle C_{co}/\triangle T$ indicates the stability of the material against coking, respectively the deactivation stability.

All samples were tested and the detailed kinetic results, along with a description of the turnover frequencies, have been published in [23]. Figure 2-3 exhibits the assessment of the performances of the individual samples in dry reforming at elevated pressures. The activity has been plotted against the deactivation and three categories of compounds can be identified:

- Moderately active and stable
- Highly active but unstable
- Highly active and stable

All samples of Ba^{2+} and Sr^{2+}, regardless of the content of Ni display very high activity in the reforming reaction, however the deactivation of the samples vary significantly. While the two catalysts with very low contents of Ni (BaNi0.25 1200 and SrNi0.25 1200) are stable against coking, all other materials deactivated severely. It is likely that the low Ni content of these materials render accordingly stable Ni particles, which have been reported to be less prone to coking already by Lercher et al. [12] and also Gardner [13].

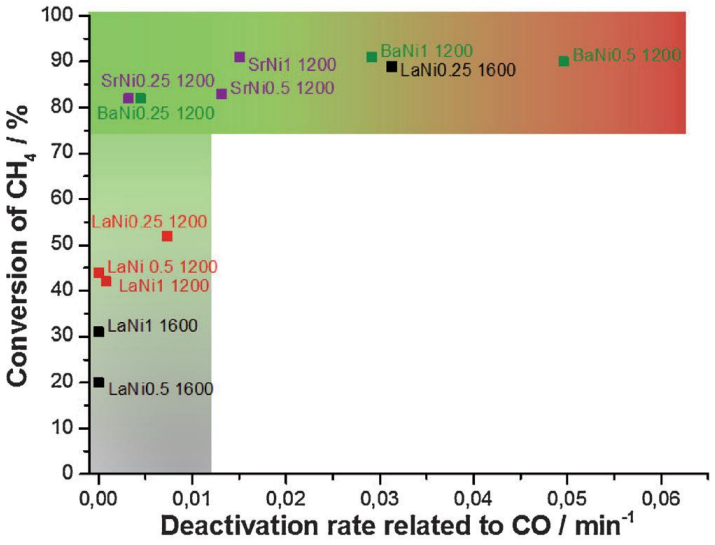

Figure 2-3 Comparison of the samples containing Sr (■), Ba (■) and La calcined at 1473 K (■) and 1873 K (■) [23]

Another picture is drawn for the La containing materials, which were all only of moderate activity – except for LaNi0.25 1600. This material was extremely active but also deactivated severely. The tendency to higher activity and deactivation can also be

observed in LaNi0.25 1200. Thus, going below a certain threshold seems to expose more active centers in the La^{3+}-materials and simultaneously destabilizing the system against coking. However, it remains unclear if there are more centers active or those exposed centers provide more activity. The LaNi0.5 and LaNi1 materials show reduced activity but on the other hand, deactivation is quasi not measureable for those samples, which renders them very interesting for further applications.

2.2.3 Conclusions

To identify the best performing hexaaluminate in dry reforming, a tradeoff between high conversion, hence strong activity, and good stability against coking needs to be made. All materials that contain Sr^{2+} or Ba^{2+} as counter ion exhibit extensive activity with CH_4 conversion levels above 80% after 600 min of reaction. However, the samples deactivate stronger than the catalysts with La^{3+} as their counter ion in the crystal structure. This is especially true for medium and high Ni contents. A contrary trend is found for the samples with very low Ni contents, where the La^{3+} samples deactivate stronger than the ones containing Ba^{2+} or Sr^{2+}. The only La^{3+}-sample exhibiting significantly boosted activity, unfortunately, accompanied with very poor stability, is LaNi0.25 1600. Consequently, the only set in the series with low deactivation tendency, regardless its Ni content, are the La^{3+}-hexaaluminates calcined at 1473 K. Therefore, these samples are identified as the most promising candidates for the DRM process and will be focused on.

For further information on the structural and kinetic properties of the samples, please refer to [22] and [23].

2.3 Part 2: Refining the synthesis route

Having decided on La^{3+} as the counter ion of choice, the influence of the addition of polyethylene glycol during the synthesis procedure is being investigated. Two sets of materials were prepared with and without PEG as assisting component. The materials were tested with respect to their phase composition, their reduction stability and their behavior in single-pass dry reforming experiments. Ni contents were spread to a wider range than in the former experiments to emphasize the differences between the individual samples.

2.3.1 Experimental

2.3.1.1 Recrystallization synthesis

In the recrystallization synthesis the metal nitrates were mixed in stoichiometric compositions and solved in 100 ml deionized water at ambient temperature. The resulting mixture was stirred for 2 h to ensure complete dissolution, subsequently dried for 12 h at 353 K, then mortared and finally calcined for 6 h at 873 K and for 8 h at 1473 K. The resulting materials were had a light blue color, which intensified at higher Ni content.

2.3.1.2 Polyethylene glycol synthesis (PEG)

In the PEG assisted synthesis the materials were mixed and dissolved in 100 ml deionized water at ambient temperature and in a separate container polyethylene glycol (PEG) was dissolved in 100 ml of 2-propanole at 343 K. The aqueous mixture was added drop wise into the PEG solution and then stirred for 2 hours at 343 K before drying at 353 K for 12 h. After mortaring the resulting solid was calcined at 873 K for 6 h and at 1473 K for 8 h. Deep blue materials were obtained.

2.3.1.3 Structural properties

Specific surface area was determined in a *Sorptomatic 1990* system by N_2 sorption. Before measurement, the sample was outgassed for 2 hours at 523 K. Subsequently, it was cooled to 77 K and measurement was conducted at relative pressures (p/p^o) from 0.03-0.1.

Dispersion measurements were conducted in the same setup but measurements the samples were pre-reduced in a stream of H_2 at 1073 K, transferred into the system and again treated at 101.3 kPa of stagnant H_2 at 673 K for 3 hours. After evacuation of the

system (to < 0.1 Pa) at constant temperature for 30 min the measurement was conducted at 308 K. For every increment in the pressure range of 0.57-1.02 kPa an equilibration time of 3-5 min was used. A second isotherm was measured after finishing the first run and evacuating the system to a pressure of below 10^{-1} Pa for 1 hour. By extrapolating the linear part of the difference isotherm (the second isotherm subtracted from the first run) to zero pressure the amount of calculated hydrogen was calculated. To calculate the Ni dispersion a stoichiometry for $H/Ni_{surface}$ of 1 was assumed [24].

2.3.1.4 X-ray diffraction (XRD)

The XRD patterns were obtained from a *Philips X´pert System* in a 2θ range from 15° to 70° with a step size of 0.017° and a time per step of 114.9 sec. Operating conditions of the Cu anode were 45 kV and 40 mA with a radiation of 154.2 Å wavelength. *HighScore Plus 3.0* (*PANalytical*) was used to compare the experimental results with patterns from the *Open Crystallographic Database (OCD)* and to conduct the Rietveld refinement of the samples.

2.3.1.5 Electron microscopy

To prepare for electron microscopy 2 mg of crushed sample was transferred into an Eppendorf cap filled with ethanol, dispersed in an ultrasonic bath and one drop of the resulting mixture was added to copper grid supported film. Transmission electron microscopy (TEM) images were collected on a *JEM-2010-JEOL microscope*. For the electron supply it had equipped a LaB_6 source with which the electrons were accelerated to 120 kV (0.2 nm microscope resolution). Scanning Electron microscopy (SEM) was done on a high resolution *FE-SEM, JSM 7500 F (JEOL) with EDX (Oxford)*.

2.3.1.6 Catalytic reactions

The activity and stability of the materials in dry reforming was tested in a high temperature reaction setup equipped with a stainless steel reactor tube ($Ø_{in}$ 8 mm, $Ø_{out}$ 10 mm) heated to 1123 K and pressurized to 1 MPa. Before testing the samples were ground, pressed and sieved to 500 – 710 µm. Subsequently they were mixed with SiC of the same particle size in a mass ratio of 1:4. 100 mg of the mixture was inserted into an AlO_x-tube ($Ø_{in}$ 6 mm, $Ø_{out}$ 7 mm) and fixed by two layers of quartz wool. The so-prepared tube was then introduced into the steel reactor and sealed at the ends to prevent lateral gas flow along the steel reactor walls. Reactor pressure was controlled

with a back-pressure-regulator and *Bronkhorst* flow meters were used to set the gas flow. Activation of the catalysts was done at 1073 K in a stream of 20% of H_2 in N_2 with an overall flow of 100 ml_n/min at a pressure of 1 MPa. Stability tests were then conducted in a gas stream of 45 ml_n/min of CO_2, 45 ml_n/min of CH_4 and 10 ml_n/min of N_2 as internal standard. All lines in the setup were heated to 453 K to prevent water condensation during the experiments. The product composition was measured with a *Shimadzu 2010* GC system equipped with a molsieve and a HQ-Plot column for gas separation and an FID as well as a TCD detector.

2.3.2 Results

2.3.2.1 Structural Properties

The specific surface area, the dispersion of the Ni particles of the materials have been tested by nitrogen and hydrogen adsorption. The results of the measurements have been summarized in Table 2-2. Six different catalysts were produced and characterized. The nomenclature followed a combination of the specific synthesis route (recrystallization = RC, polyethylene-glycol assisted synthesis = PEG) and the Ni loading (1 wt.-%, 5 wt.-% and 10 wt.-%). This means, the material produced by the recrystallization method containing 1 wt.-% Ni is e.g. named RC1 and the catalyst from the polyethylene glycol synthesis containing 5 wt.-% Ni is named PEG5, respectively.

Table 2-2 Structural properties of the HA materials synthesitzed with and without polyethylene glycol [1] reduced form

Sample	Stoichiometry	Ni content	BET surface	Dispersion [1]
		[wt.-%]	[m²/g]	[%]
RC1	$LaNi_{0.1}Al_{11.9}O_{19}$	1	4.5	< 1
RC5	$LaNi_{0.7}Al_{11.3}O_{19}$	5	2.9	< 1
RC10	$LaNi_{1.4}Al_{10.6}O_{19}$	10	3.6	< 1
PEG1	$LaNi_{0.1}Al_{11.9}O_{19}$	1	10.7	< 1
PEG5	$LaNi_{0.7}Al_{11.3}O_{19}$	5	7.1	< 1
PEG10	$LaNi_{1.4}Al_{10.6}O_{19}$	10	3.5	< 1

The surface areas of the RC materials range from 2.9 m²/g (for RC5) to 4.5 m²/g (for RC1) but to not have a clear trend, while the PEG materials decrease from 10.7 m²/g to 3.5 m²/g in surface area with increasing Ni loading. However, all of the surface areas are very low, which can be traced back to the high calcination temperatures that were applied to obtain the phase transition from α- to β-alumina and to form the magnetoplumbite phase. Additionally, there is no measureable porosity in the materials, regardless of the Ni content applied. As a consequence, the measurable dispersion of the samples is also very low. The Ni-dispersion is less than 1%, which is even at the lower limit of accuracy for the measurement.

2.3.2.2 X-Ray Diffraction

XRD patterns of the as-synthesized materials reveal the good crystallinity of all materials, as very sharp reflexes are observed (Figure 2-4). In all samples the typical signals for HA can be observed though none of the materials consists purely this structure and additional signals are present. To obtain the phase composition of the individual samples Rietveld refinement has been conducted and the results for all samples have been summarized in Table 2-3. The structures for $LaNiAl_{11}O_{19}$ and $LaAl_{12}O_{19}$ merely differ in the occupancy with Al or Ni of two atomic-positions in the unit cell. Therefore, the main signals for $LaNiAl_{11}O_{19}$ and $LaAl_{12}O_{19}$ (at 31.1°, 34.0° and 36.1°) are the same and discrimination of those structures in a Rietveld refinement would cause a significant error [25, 26]. Thus to the sum of those two structures will from now on be referred as hexaaluminate (HA) phase.

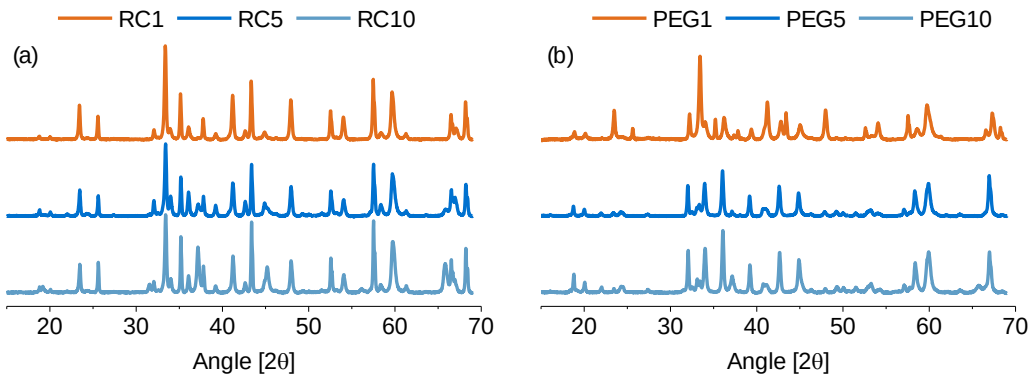

Figure 2-4 X-ray diffraction patterns of the as synthesized materials from recrystallization and PEG synthesis

In RC1, RC5 and RC10 the elements Al, La and O are mainly bound in the two phases Al_2O_3 (35.2°, 43.3°, 57.5° [27]) and $LaAlO_3$ (33.4° [28]), but their content diminishes with increasing Ni concentration. In RC5 and RC10 additionally significant amounts of $NiAl_2O_4$ (37.0°, 65.6° [29]) are present and at a concentration of 10 wt.-% there is even some pure Ni (44.7° [30]) detectable. The composition seems to have an optimum at 5 wt.-% of Ni, with respect to the content of HA. The weight percent of HA in RC5 is 27% and therefore higher than for the RC1 (20%) or for RC10 (14%).

Table 2-3 Results of the Rietveld analysis of the XRD patterns of the as-synthesized materials

Sample	HA	Al_2O_3	$LaAlO_3$	$NiAl_2O_4$	Ni^0
	[wt.-%]	[wt.-%]	[wt.-%]	[wt.-%]	[wt.-%]
RC1	20	63	17	-	-
RC5	27	51	12	10	-
RC10	14	50	10	25	1
PEG1	53	27	20	-	-
PEG5	96	-	3	1	-
PEG10	86	-	2	10	2

Similar trends are obtained for the PEG materials with the main difference that there is a much higher content of HA phase in the samples present. The HA phase content again goes through a maximum of 96 % for PEG5, while in PEG1 there is only 53 % HA and in PEG10 there can be 86 % of HA found. With increasing Ni loading the corundum vanishes (from 27 % in PEG1) as well as the $LaAlO_3$ does (from 20 % in PEG1 to 2 % in PEG10). At low loadings there is neither pure Ni nor spinel present but both contents increase when increasing the Ni loading (e.g. to 10 % for spinel and 2 % for the pure Ni^0 in PEG10). The syngas production atmosphere contains CH_4, CO and H_2 at high

temperatures and is therefore strongly reducing. To test the stability of the set of materials under such conditions the samples have been treated for 2 hours in a stream of pure hydrogen at 1073 K and then were examined again by XRD (Figure 2-5).

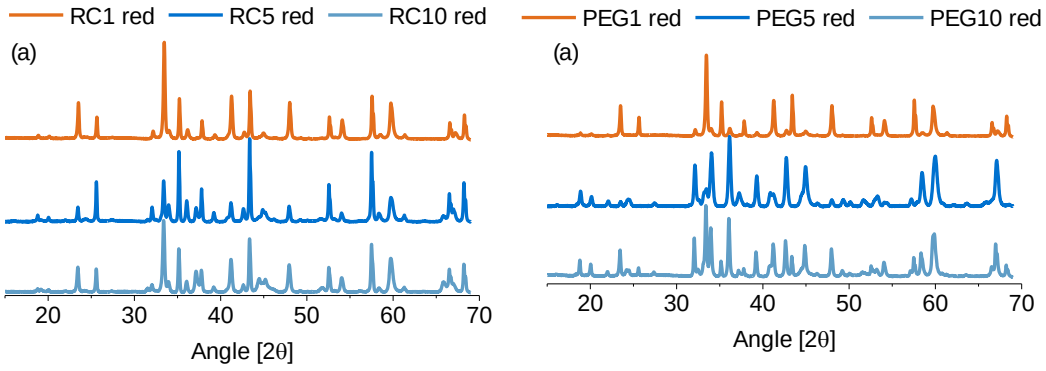

Figure 2-5 X-ray diffraction patterns of the catalysts after reduction in a stream of hydrogen at 1073 K

The patterns indicate that the H_2-treatment did not destroy the crystallinity of the samples, while the composition changed – in parts severely. The composition of the phases, as calculated by Rietveld refinement, is given in Table 2-4.

Table 2-4 Phase composition of the catalysts after reduction in a stream of hydrogen at 1073 K

Sample	HA [wt.-%]	Al_2O_3 [wt.-%]	$LaAlO_3$ [wt.-%]	$NiAl_2O_4$ [wt.-%]	Ni^0 [wt.-%]
RC1	14	62	23	-	1
RC5	18	68	6	6	2
RC10	12	55	14	15	4
PEG1	14	62	23	-	1
PEG5	91	-	3	6	-
PEG10	66	17	12	-	5

Reduction removes Ni from the oxide structures (HA and $NiAl_2O_4$) in the RC materials and leaves them diminished. Consequently, the content of Ni^0 after reduction increases with higher loading. This removal breaks up the HA and the spinel phases, leaving significantly more Al_2O_3 and $LaAlO_3$ in the material. Very similar results are obtained for the two materials PEG1 and PEG10 after reduction. Both significantly lose HA phase content (29 % less in PEG1 and 20 % less in PEG10) and build up Ni^0, Al_2O_3 and $LaAlO_3$. In addition, the PEG10 loses its complete content of $NiAl_2O_4$. The one material that

behaves out of line is PEG5. There is no Ni found even after 2 hours of reduction and the HA phase is very well preserved. The sample merely loses 5 % of its HA phase and forms $NiAl_2O_4$ structure. The rest of the sample stays unaltered.

It is not possible to obtain the Ni content in the hexaaluminate phase directly but one can calculate the fraction of Ni in the individual phases HA, $NiAl_2O_4$ and Ni^0 from the phase content of the two latter and the overall Ni concentration. The results of this calculation are given in Table 2-5. It is obvious that PEG1 and RC1 have all the Ni bound in the HA before reduction but cannot stabilize it and thus form Ni^0 during the treatment. In RC5 there are 60 % of Ni bound in spinel and merely 40 % remain for the HA. During the reduction treatment Ni^0 forms in equal amounts from HA and spinel. In the end the Ni is bound to 20 % in HA, 40 % in $NiAl_2O_4$ and 40 % in Ni^0. On the other hand, PEG5 fixes almost all the Ni in the HA, leaving less than 10 % in the spinel phase. Reduction releases 40 % from the HA, forming $NiAl_2O_4$, leaving exactly half of the Ni in the HA and half of it in the $NiAl_2O_4$. The most remarkable difference in the composition can be observed between RC10 (10 % in HA) and PEG10 (50 % Ni in AH). Here the rest of the Ni is bound in $NiAl_2O_4$ and Ni^0. Interestingly the contents of Ni in HA do not change during reduction but the $NiAl_2O_4$ reduces strongly in both materials.

Table 2-5 Content of Ni in the individual phases before and after reduction as calculated from the $NiAl_2O_4$ and Ni^0 content.

	As-synthesized			After reduction		
	HA [wt.-%]	**$NiAl_2O_4$ [wt.-%]**	**Ni^0 [wt.-%]**	**HA [wt.-%]**	**$NiAl_2O_4$ [wt.-%]**	**Ni^0 [wt.-%]**
RC1	100	-	-	-	-	100
RC5	40	60	-	20	40	40
RC10	10	80	10	10	50	40
PEG1	100	-	-	-	-	100
PEG5	90	10	-	50	50	-
PEG10	50	30	20	50	-	50

2.3.2.3 Electron microscopy

The shapes of the catalyst surfaces were investigated by scanning and transmission electron microscopy (SEM and TEM). As RC5 and PEG5 exhibit the most significant difference in the structure at the same Ni loading, these materials have been selected and the resulting SEM pictures are shown in Figure 2-6. RC5 contains many small primary particles that reflect the inhomogeneity in the phase composition of the material. Contrary to this, PEG5 mainly consists of hexagonal patterns that are very typical for the HA crystal [17] and only smaller crystallites of less well-structured material. These are the minor contributions of the Al_2O_3 that is still left in the material besides the HA phase.

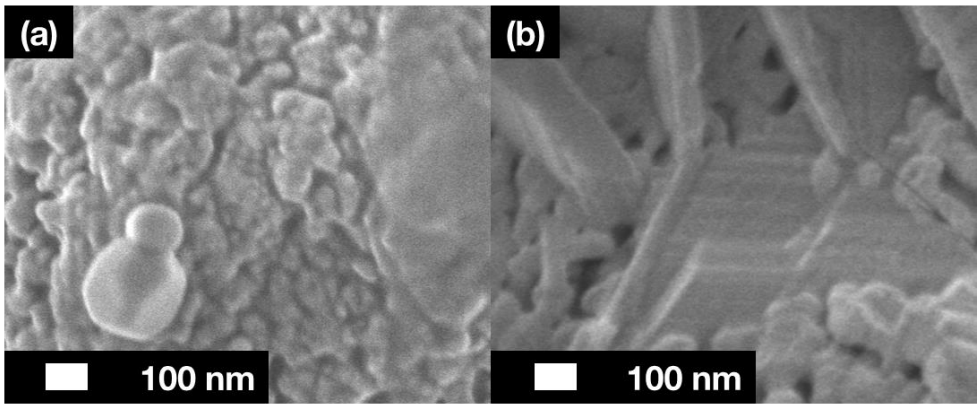

Figure 2-6 SEM pictures of the two materials RC5 and PEG5 with clearly better crystallinity for the PEG material

Transmission electron microscopy also reveals the differences in composition of the two selected materials RC5 and PEG5 Figure 2-7. While the RC5 only contains unstructured matter (Figure 2-7(a)), in the PEG5 material large arrays of parallel stacks can be observed (Figure 2-7(b)). To check whether the layers observed in PEG5 are really part of the HA crystal the interlayer distance has been compared to the size of the lattice planes involved and the 13 Å measured from the TEM measurement is in decent agreement with the distance of the (002) planes of 11 Å given in the literature [25].

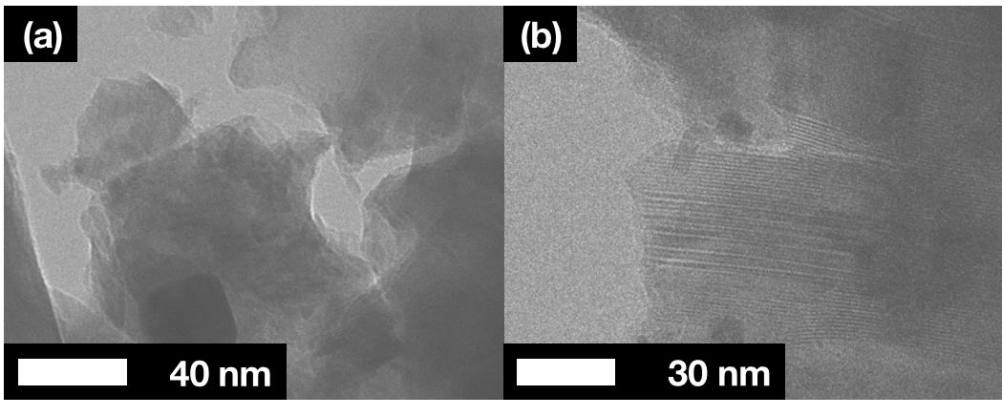

Figure 2-7 TEM pictures of the fresh RC5 (a) and PEG5 (b) sample

2.3.2.4 Reforming activity

The reforming activity of the samples was tested at 1123 K and 1 MPa, which are assumed to be close to reasonable settings for a technical application of DRM. Under the chosen conditions the thermodynamically possible conversion of CO_2 is 92 % and for CH_4 it is 84 %. Regardless of the differences in the catalytic results, that will be

discusses later on, all materials had three things in common: 1) Conversion of CO_2 is higher than for CH_4. 2) H_2, CO and H_2O are found as products in the gas stream. 3) The resulting H_2/CO ratio is less than unity. The formation of H_2O together with the low H_2/CO ratio hints to the reverse water gas shift reaction (RWGS, (2-1)) to that proceeds in parallel to the DRM reaction.

$$CO_2 + H_2 \rightleftharpoons H_2O + CO \qquad \Delta H^0_{298K} = 41\ \mathrm{kJ/mol} \qquad (2\text{-}1)$$

This side reaction alters the H_2/CO ratio in the product gas stream and is much faster than the DRM reaction. As it is usually considered quasi-equilibrated under DRM conditions [31] it cannot serve as indicator in the deactivation measurements discussed here.

At the start of the experiment RC1 and PEG1 exhibit 43 % conversion of CO_2 (Figure 2-8, a) and 31 % of CH_4 (Figure 2-8, b), respectively. Both materials deactivate strongly with a faster initial loss in activity in the PEG material. After 600 min of reforming the conversions dropped to 28 % in CO_2 and to 19 % in CH_4. The main difference between the two materials is that the PEG1 deactivates during the first 200 min and has a constant activity after on. RC1, on the other hand, maintains higher conversions levels at the beginning but it suffers a constant loss in activity over the complete time on stream. Additionally, the deactivation of RC1 does not come to an end, but appears to continue also after 600 min of reaction.

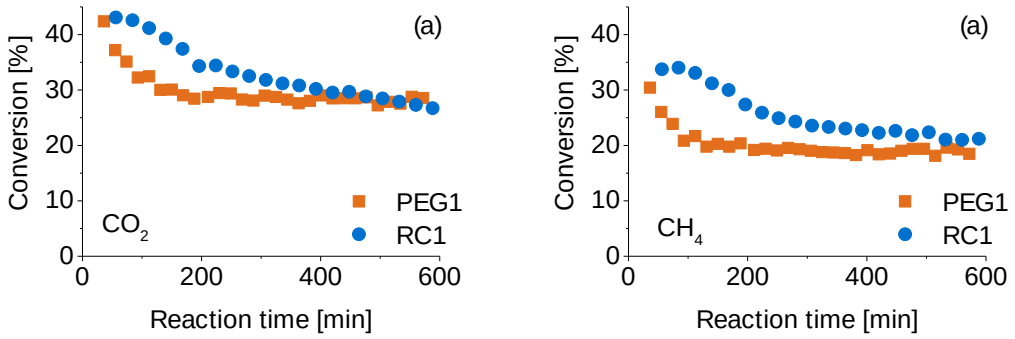

Figure 2-8 Both materials containing 1 wt.-% Ni (■ PEG1, ● RC1) exhibit very high initial activity in the conversion of CO_2 (a) and CH_4 (b), respectively but suffer strong deactivation.

Both, RC 5 and PEG5 exhibit very little deactivation, as can be observed from Figure 2-9. RC5 even goes through a very distinct initial phase of activation. The conversion of RC5 increases within 300 min from 20 % to 25 % for CO_2 (Figure 2-9, a) and from 10 % to 18 % for CH_4 (Figure 2-9, b) and stays almost constant for another 200 min. After 500 min slight deactivation sets in but the loss is merely one percent of conversion. PEG5 also activates however not as pronounced as RC5. After this initial increase from 32 % to 36 % the material converts CO_2 very steadily with a minor loss in activity of 2 % over 600 min. The CH_4 conversion increases at the same time from 22 % to 26 % and subsequently also loses 2 % of activity. Thus at the end of the experiment the conversion of CH_4 has dropped to 24 %. The conversion of both, CO_2 and CH_4 is always higher over PEG5 than on RC5.

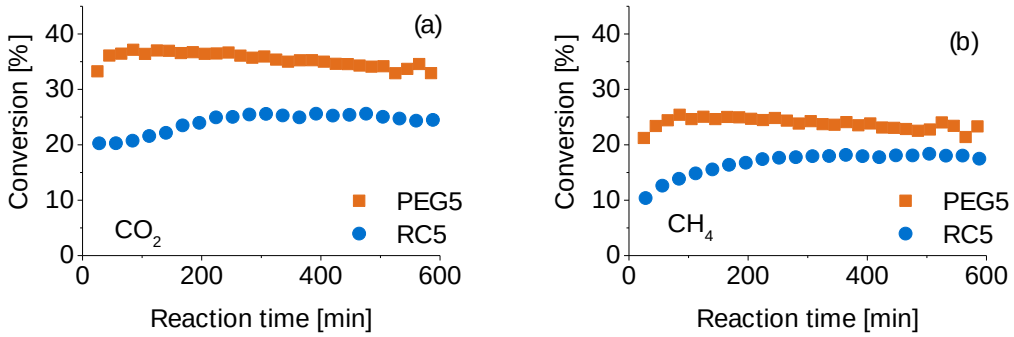

Figure 2-9 Stable conversions are observed on the 5 wt.-% Ni materials (■ PEG1, ● RC1) for CO_2 (a) and CH_4 (b) conversion.

RC10 and PEG10 exhibit a short initiation phase in the conversions of CO_2 (Figure 2-10, a) and CH_4 (Figure 2-10, b). The conversion over RC10 steeply increases over 100 min from 14 % to 32 % in CO_2 and from 8 % to 23 % in CH_4. The conversion over PEG10 starts at 35 % (CO_2) and 23% (CH_4) and increases to 39 % (CO_2) and 26 % (CH_4) after 20 min. After their initiation both materials start to deactivate and their behavior follows the one already seen for the 1 wt.-% Ni containing catalysts. PEG10 rapidly loses activity until it reached a constant conversion level of 27 % in CO_2 and 17 % in CH_4. The catalyst can maintain this conversion after on all through the experiment. RC10 deactivated similarly but could not stabilize its activity later on. After 600 min of reaction the activity of RC10 dropped to 22 % conversion in CO_2 and 15 % in CH_4.

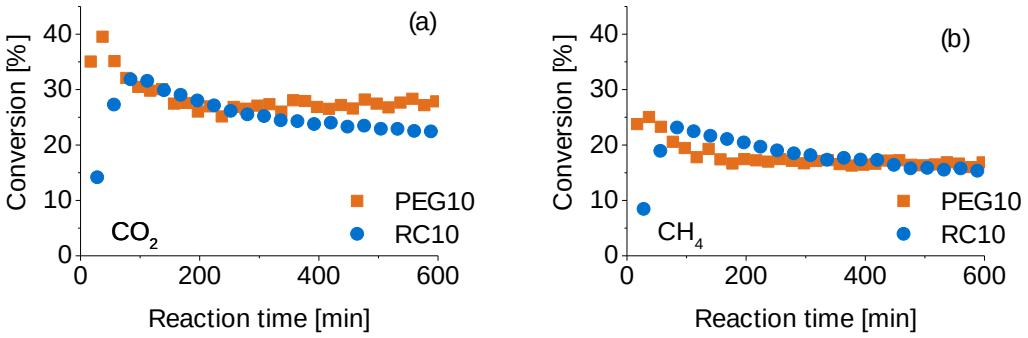

Figure 2-10 Deactivation behavior of the catalytic materials with 10 wt.-% Ni synthesized following the recrystallization (●) and the PEG synthesis (■). Conversions of CO_2 (a) and CH_4 (b) exhibit initial activation followed by constant deactivation over RC10 and a finally stable activity on the PEG10 material.

2.3.2.5 Carbon deposition

The carbon deposed during 10 hours of DRM over the two materials RC5 and PEG5 was checked by electron microscopy. In Figure 2-11 the RC5 material is shown and its complete outer surface is covered in carbon. The region on the lower right corner, which is free of coke (Figure 2-11 (a)), has presumably not been exposed to the gas phase during reaction and was uncovered afterwards during the preparation of the sample for SEM. Enlarging the picture (Figure 2-11 (b)) clearly shows that the surface is strongly covered with whiskers and a smooth layer, which is likely to be graphitic carbon.

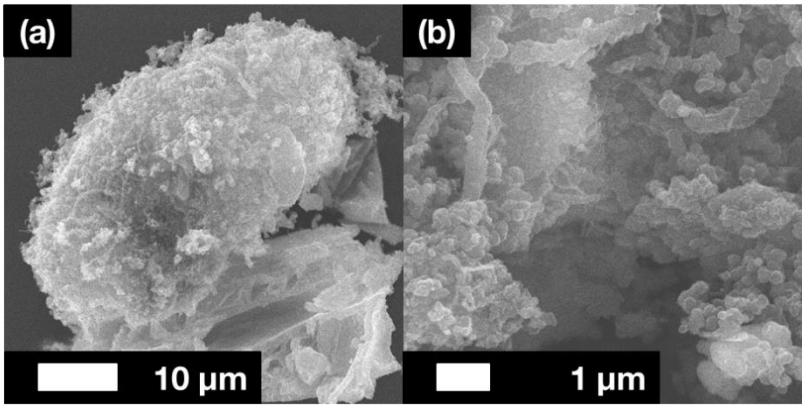

Figure 2-11 SEM picture of the RC5 material after the DRM reaction. (a) Clearly visible are the carbon deposits on the outer surface of the material. (b) Enlargement of the picture with a close look at the various carbon deposits visible on the catalyst after reaction.

A very different picture give the measurements of PEG5 after reaction. The outer surface of the catalysts is almost free of coke, despite strong formation of carbon whiskers during the reaction. Those whiskers found in Figure 2-12 (a) are also presented in the TEM

picture Figure 2-12 (b). As this picture shows, the fibers are hollow with an inner diameter of $Ø_{in}$ = 20 nm and an outer aperture of $Ø_{out}$ = 35 nm. The particles found on the catalysts surface have an average diameter of 30 nm. Nickel is a metal that is well known and widely applied for its ability to form CNT´s under the influence of CH_4. Possible mechanisms explaining the formation of such fibers include the movement of C on or through the Ni particle and the subsequent detachment of the coke from the metal into the fiber. An elder explanation was that the C dissolves within the Ni and wanders through the particle to form the fiber [32]. More recently the theory was developed that the carbon moves on the Ni surface without dissolving in the particle and then builds up the whiskers. The consequence of both mechanisms is that the metal particle migrates within the tip of the tube that it is forming [32]. The similarity in the diameters of the particles and those of the carbon whiskers suggest that they really are carbon-nano tubes and that they are formed via carbon migration on or through the Ni particle.

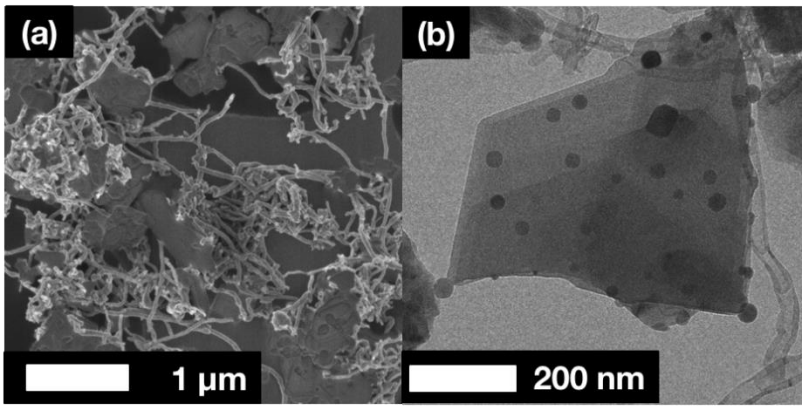

Figure 2-12 Electron microscopy pictures of PEG5 after 10 hours in DRM. (a) Only CNT´s as carbon deposits are visible in the SEM picture. The surface of the catalyst is almost completely free of coke. (b) Ni particles of the same size as the formed hollow CNT´s are present on the catalysts surface. The hexagonal structure of the support is still visible.

2.3.3 Discussion

The physio-chemical properties of all samples are almost the same. The outer surfaces of the catalysts do not exceed values of 11 m²/g and there are no pores detectable by sorption measurements. Additionally, the dispersion of Ni does not exceed 1 %. All of these characteristics can be referred to the very high calcination temperatures applied during synthesis. Those are mandatory to obtain a phase transition of the α- to β-Al_2O_3 and thus to form the HAs. At temperatures of 1473 K the materials lose most of their outer surface to sintering and leave very little centers accessible. This is well known for

HAs, so the key difference among the materials is the phase composition of the crystal itself [17].

The fraction of the HA phase varies strongly within the produced materials, ranging from 14 % to 96 %. The HA phase content in PEG1 is 30 % higher than in RC1. In the synthesis of PEG5 and PEG10 the HA phase even increases its content about 70 % (from RC5 and RC10, respectively). Temperatures of 1473 K are comparatively low in hexaaluminate synthesis [16, 33] and increased temperature during the treatment would probably also increase the content of pure hexaaluminate. Nevertheless, higher temperatures always mean higher energy demand in the production process and at lower calcination temperatures the PEG enhances the formation of the HA phase significantly. Additionally, the Ni content has a substantial effect on the phase composition. The as-synthesized PEG1 merely contains 53 % of HA phase while the rest of the material is Al_2O_3 and $LaAlO_3$. It seems there is not enough Ni present to form more HA phase, hence the La, Al and O get stored into the two other phases. On the other hand, the HA phase cannot uptake the complete 10 wt.-% of Ni in the PEG10 and thus dispenses it into $NiAl_2O_4$ and Ni^0. The optimum Ni content is at 5 wt.-% with a yield of 96 % of HA in the material. The trend to a higher HA content in the RC5 sample is also clearly detectable, though it does not reach as high HA wt.-% as the PEG5.

The sole increase of the HA content does not automatically lead to more temperature stable materials as the reduction experiments show. Under the influence of a hydrogen-rich stream all the materials decompose parts of their HA phase into other structures. While the RC materials and PEG5 still stay mostly unaltered, PEG1 and PEG10 lose about 30 % of their HA into other phases. After reduction PEG1 has nearly the same phase composition as the RC1 sample, which leads to the assumption this might be a stable configuration under these conditions. PEG10 also loses 30 % of the HA phase but with an initial content of 85 % it still contains much more HA after the treatment than RC10. It additionally loses its free $NiAl_2O_4$ during the procedure and sets free $LaAl_2O_3$, Al_2O_3 and Ni.

Apparently a concentration of 5 wt.-% Ni in the material stabilizes the magnetoplumbite phase very effectively as under the treatment with H_2 still more than 90 % of the HA phase is preserved. The high phase purity can be assumed to be the reason for the good resistance against re-structuring under the in influence of the reducing agent. Fewer impurities also mean less structural stress and therefore the material does not undergo significant changes.

It can be deduced from the calculations of the Ni contents in the individual phases, that the addition of PEG into the synthesis mixture positively influences the incorporation of Ni into the HA phase as the content throughout the series increases from RC to PEG. Additionally, it seems that there is a maximum threshold that can be incorporated into the HA as the PEG5 and the PEG10 both have 5 wt.-% of Ni in this phase. Doubling the Ni content in the synthesis does not linearly increase the fraction of Ni in the HA, but in PEG10 the excess metal forms $NiAl_2O_4$ and Ni^0. It seems that the optimal content of Ni to form $LaNiAl_{11}O_{19}$ is 5 wt.-%. So this is most probably the explanation for the high HA content, found in PEG5. From the Ni contents of the HA in PEG1 and PEG10 it becomes obvious why both materials lose so much of their HA during reduction. Both materials contain Ni deficient $LaAl_{12}O_{19}$, which seemingly cannot withstand the reductive atmosphere and transforms into Al_2O_3 and $LaAlO_4$.

The various materials exhibit strong differences among one another in their behavior in dry reforming, which can be referred to the way the Ni is bound into the materials. RC5, RC10 and PEG5 show the most distinct period of activation and in parallel those materials exhibit the largest fraction of $NiAl_2O_4$ after reduction. Ni^0 is assumed to be more active in DRM than Ni^{2+} [34] so the initial activation period in those materials might indicate further reduction of spinel. On the other hand, the fraction of Ni^0 cannot be the only factor for a sample´s activity in DRM. The maximum conversion of RC1 and PEG1 is higher than the one over RC10 and PEG10 though the latter contains up to 5 times more Ni^0. Additionally, PEG5 is the most stable materials and at the same time the only sample that does not exhibit Ni^0 after reduction. XRD demands crystallite arrays of a definite size to be able to detect certain phases [35], and together with the finding of arrangements in TEM, which very likely are Ni particles (Figure 2-12 (d)), one can assume that minor parts of the Ni in PEG5 get reduced from the HA and $NiAl_2O_4$ and form very small Ni^0 arrays. During the initiation phase presumably more Ni gets reduced, forming the later visible particles. After 600 min of DRM there can be CNT´s found on PEG5 that are much larger than 2 nm. Thus, during the reaction more Ni must get reduced, sinter to large particles and subsequently form carbon whiskers.

The varying reactivity of the materials reflects also in the carbon deposition that occurs during reaction. The two materials tested as references, RC5 and PEG5, exhibit severe carbon deposition but the kind of coke formed is very different on the two materials. The outer surface of RC5 is completely covered in inhomogeneous clusters of carbon. CNT´s and graphitic deposits are both present. On the other hand, PEG5 itself is almost free of carbon, while the vicinity of the catalyst is crowded with CNT´s that clearly have grown out of the materials surface. The dissimilarities in the carbon deposition hint to different

forms of Ni on the catalyst. While in PEG5 the Ni is contained only in one phase, in RC5 there are several phases that contain the metal. On those phases various types of carbon can be formed. RC5 contains more Ni^0, while the content of $NiAL_2O_4$ is almost the same in both materials. Thus the larger amount of free Ni on the surface can be referred to as the reason of the more severe carbon deposition on RC5.

2.3.4 Conclusions

To obtain phase pure hexaaluminates at relatively low calcination temperatures and short calcination times one possibility is to add PEG into the synthesis mixture. With PEG present during the temperature treatment the phase purity of all tested materials increased significantly. For producing Ni-containing hexaaluminates it is of importance to utilize the right content of Ni to improve the result. A loading of 1 wt.-% is not enough to produce phase pure hexaaluminate, so Al_2O_3 and $LaAlO_3$ will be formed from the excess material. On the other hand, 10 wt.-% Ni cannot be incorporated into the hexaaluminate completely, leaving $NiAl_2O_4$ and Ni^0 in the sample. Thus, the optimal content of Ni to form $NiLaAl_{11}O_{19}$ is 5 wt.-% of Ni, which forms a material that contains to 95 % of the desired HA phase. The increased phase purity reflects into the stability of the materials in the DRM reaction with a comparably higher and more stable conversion over the PEG materials and significant changes in the activity of the RC materials. The carbon deposed on the PEG materials does not cover the catalysts surface but grows out of it in the form of CNT´s. On the other hand, the RC materials form whiskers and layered carbon on the surface leading to the ongoing deactivation of the materials.

2.4 Literature

[1] K. Seshan, W. Hally, J.H. Bitter, J.A. Lercher, Catalysis and Adsorption in Fuel Processing in Environmental Protection, Wydawnictwo Politechniki Wrocławskiej 1996, pp. 33.

[2] J.R. Rostrupnielsen, J.H.B. Hansen, J. Catal., 144 (1993) 38.

[3] D. Liu, X.Y. Quek, W.N.E. Cheo, R. Lau, A. Borgna, Y. Yang, J. Catal., 266 (2009) 380.

[4] C. Daza, O. Gamba, Y. Hernández, M. Centeno, F. Mondragón, S. Moreno, R. Molina, Catal. Lett., 141 (2011) 1037.

[5] K. Wang, X. Li, S. Ji, B. Huang, C. Li, ChemSusChem, 1 (2008) 527.

[6] T. Xiao, T. Suhartanto, A.P.E. York, J. Sloan, M.L.H. Green, Appl. Catal., A, 253 (2003) 225.

[7] J.A.C. Dias, J.M. Assaf, Catal. Today, 85 (2003) 59.

[8] J.D.A. Bellido, J.E. De Souza, J.-C. M'Peko, E.M. Assaf, Appl. Catal., A, 358 (2009) 215.

[9] C.E. Daza, J. Gallego, J.A. Moreno, F. Mondragón, S. Moreno, R. Molina, Catal. Today, 133-135 (2008) 357.

[10] S. Corthals, T. Witvrouwen, P. Jacobs, B. Sels, Catal. Today, 159 12.

[11] S. Corthals, J. Van Nederkassel, H. De Winne, J. Geboers, P. Jacobs, B. Sels, Appl. Catal., B, 105 (2011) 263.

[12] J.A. Lercher, J.H. Bitter, W. Hally, W. Niessen, K. Seshan, in: W.N.D.E.I. Joe W. Hightower, T.B. Alexis (Eds.) Stud. Surf. Sci. Catal., Elsevier1996, pp. 463.

[13] T.H. Gardner, J.J. Spivey, E.L. Kugler, D. Pakhare, Appl. Catal., A, 455 (2013) 129.

[14] K. Ikkour, D. Sellam, A. Kiennemann, S. Tezkratt, O. Cherifi, Catal. Lett., 132 (2009) 213.

[15] N. Iyi, S. Takekawa, S. Kimura, J. Solid State Chem., 83 (1989) 8.

[16] W. Wintruff, Kristall und Technik, 9 (1974) 391.

[17] T.H. Gardner, J.J. Spivey, E.L. Kugler, A. Campos, J.C. Hissam, A.D. Roy, Journal of Physical Chemistry C, 114 (2010) 7888.

[18] T.H. Gardner, D. Shekhawat, D.A. Berry, M.W. Smith, M. Salazar, E.L. Kugler, Appl. Catal., A, 323 (2007) 1.

[19] J. Wang, Y. Liu, T. Cheng, W. Li, Y. Bi, K. Zhen, Appl. Catal., A, 250 (2003) 13.

[20] Z. Xu, M. Zhen, Y. Bi, K. Zhen, Appl. Catal., A, 198 (2000) 267.

[21] G. Groppi, C. Cristiani, P. Forzatti, Appl. Catal., B, 35 (2001) 137.

[22] T. Roussière, K.M. Schelkle, S. Titlbach, G. Wasserschaff, A. Milanov, G. Cox, E. Schwab, O. Deutschmann, L. Schulz, A. Jentys, J. Lercher, S.A. Schunk, ChemCatChem, 6 (2014) 1438.

[23] T. Roussière, L. Schulz, K.M. Schelkle, G. Wasserschaff, A. Milanov, E. Schwab, O. Deutschmann, A. Jentys, J. Lercher, S.A. Schunk, ChemCatChem, 6 (2014) 1447.

[24] C.S. Brooks, G.L.M. Christopher, J. Catal., 10 (1968) 211.

[25] F. Laville, M. Perrin, A.M. Lejus, M. Gasperin, R. Moncorge, D. Vivien, J. Solid State Chem., 65 (1986) 301.

[26] M. Gasperin, M.C. Saine, A. Kahn, F. Laville, A.M. Lejus, J. Solid State Chem., 54 (1984) 61.

[27] L.W. Finger, R.M. Hazen, J. Appl. Phys., 49 (1978) 5823.

[28] A. Nakatsuka, O. Ohtaka, H. Arima, N. Nakayama, T. Mizota, Acta Crystallographica Section E Structure Reports Online, 61 (2005) i148.

[29] H.S.C. O'Neill, W.A. Dollase, C.R. Ross, Phys. Chem. Miner., 18 (1991) 302.

[30] R.W.G. Wyckoff, Interscience Publishers, New York, 1965.

[31] P.E.D. Morgan, D.R. Clarke, C.M. Jantzen, A.B. Barker, J. Am. Ceram. Soc., 64 (1981) 249.

[32] M. Meyyappan, D. Lance, C. Alan, H. David, Plasma Sources Sci. Technol., 12 (2003) 205.
[33] Z. Xu, M. Zhen, Y. Bi, K. Zhen, Catal. Lett., 64 (2000) 157.
[34] M.-S. Fan, A.Z. Abdullah, S. Bhatia, ChemCatChem, 1 (2009) 192.
[35] W. Borchardt-Ott, Springer-Verlag, Berlin, 1997.

2.5 License and contributions

Significant sections of part 1 of chapter have been previously published in **ChemCatChem** under the topic "*Structure-Activity Relationships of Nickel-Hexaaluminates in Reforming Reactions Part I: Controlling Nickel Nanoparticle Growth and Phase Formation*". Reuse of the publication in this thesis has been granted by John Wiley and Sons under licensing number **3831540694005** (March 2016).

Authors of the publication are:

T. Roussière, S. Titlbach, G. Wasserschaff, S. A. Schunk*
hte AG, the high throughput experimentation company
Kurpfalzring 104, 69123 Heidelberg, Germany

K. M. Schelkle
Organisch-Chemisches Institut
Universität Heidelberg
Im Neuenheimer Feld 270, 69120 Heidelberg, Germany

A. Milanov, E. Schwab, G. Cox
GCC/PG, BASF SE
Carl-Bosch-Straße 38, 67038 Ludwigshafen, Germany

L. Schulz, A. Jentys, J.A. Lercher
Department of Chemistry and Catalysis Research Center
Technische Universität München
Lichtenbergstraße 4, 85748 Garching, Germany

O. Deutschmann
Institute for Chemical Technology and Polymer Chemistry
Karlsruhe Institute of Technology
Engesserstraße 20, 76131 Karlsruhe, Germany

Experimental design was result of a joint discussion of all partners under the lead of hte and BASF and the Karlsruhe Institute of Technology. Synthesis and structural characterization of the catalyst was accomplished in the laboratories of hte in close cooperation with Universität Heidelberg. Evaluation and interpretation of the experimental results and drafting the reduction mechanism was achieved in joint discussion amongst all involved partners.

Furthermore, significant sections of part 1 of chapter have been previously published in **ChemCatChem** under the topic "*Structure–Activity Relationships of Nickel–Hexaaluminates in Reforming Reactions Part II: Activity and Stability of Nanostructured Nickel–Hexaaluminate-Based Catalysts in the Dry Reforming of Methane*". Reuse of the publication in this thesis has been granted by John Wiley and Sons under licensing number **3831540504545** (March 2016).

Authors of the publication are:

T. Roussière, G. Wasserschaff, S. A. Schunk*
hte AG, the high throughput experimentation company
Kurpfalzring 104, 69123 Heidelberg, Germany

L. Schulz, A. Jentys, J.A. Lercher
Department of Chemistry and Catalysis Research Center
Technische Universität München
Lichtenbergstr. 4, 85748 Garching, Germany

K. M. Schelkle
Organisch-Chemisches Institut
Universität Heidelberg
Im Neuenheimer Feld 270, 69120 Heidelberg, Germany

A. Milanov, E. Schwab
GCC/PG, BASF SE
Carl-Bosch-Straße 38, 67038 Ludwigshafen, Germany

O. Deutschmann
Institute for Chemical Technology and Polymer Chemistry
Karlsruhe Institute of Technology
Engesserstr. 20, 76131 Karlsruhe, Germany

Synthesis and characterization of the samples was done by hte in close cooperation with BASF and Universität Heidelberg. Catalytic experiments were executed by Technische Universität München in close consultation with hte. Interpretation of the results and evaluation of the characteristics were done in a close collaboration of all partners under the lead of hte and Technische Universität München.

3 Coke Deposition in Dry Reforming of Methane

The reaction pathways on Ni and Pt based catalysts leading to coke formation in dry reforming were investigated. Using isotope labelled reactants (i.e., $CH_4 + {}^{13}CO_2 \rightleftharpoons 2\ CO + 2\ H_2$) showed that initially ${}^{13}CO_2$ is faster converted than CH_4 and that this higher activity leads to a higher concentration of ${}^{13}CO$ compared with ${}^{12}CO$ in the product stream, suggesting little isotope scrambling among products at this stage. Gasification of carbon deposits was found to be an important pathway enhancing the catalyst stability. Analysis of the pathways leading to carbon deposits suggest that coke is formed predominantly via reverse Boudouard reaction on Ni, while both metals contribute to CH_4 dissociation. The pronounced reversibility of the C-H and C-O bond formation and cleavage was also shown by the presence of ${}^{13}CH_4$ formed from ${}^{13}CO_2$ and ${}^{12}CO$ formed from ${}^{12}CH_4$. Numeric calculations complementing the experimental results led to the proposal of a reaction pathway for the surface reactions, accounting for the differences between Ni and Pt.

3.1 Introduction

Reforming is the key industrial technology to convert a large variety of carbon sources into either hydrogen or syngas, i.e., mixtures of H_2 and CO of varying stoichiometry. The latter can be transformed into products of value, like methanol or hydrocarbons as base platform chemicals for energy carriers or other chemical intermediates [1]. Synthesis gas production from CH_4 and CO_2 (dry reforming of methane, DRM) can be used to convert components in natural gas and CO_2 to a product with a H_2/CO ratio of one in a highly endothermic reaction (1). Other suitable sources for DRM of mixtures of CH_4 and CO_2 like bio-gas or emissions from landfill should also be mentioned in this context as potential feedstock.

$$CO_2 + CH_4 \rightleftharpoons 2\,H_2 + 2\,CO \qquad \Delta H^0_{298K} = 247\ \mathrm{kJ/mol} \qquad (3\text{-}1)$$

DRM produces the synthesis gas with the lowest H_2/CO ratio among all reforming reactions and from the downstream side a handful of processes exist, which need a carbon monoxide rich input feed such as the iron based Fischer-Tropsch process. DRM can also be utilized to reduce the H_2/CO ratio in the overall mix of steam reforming, methane partial oxidation and autothermal reforming [2]. The high concentration of carbon species in dry reforming and the absence of water shift the thermodynamic limit of carbon formation into the range of the standard process conditions of DRM, especially if the reaction is performed at elevated pressures [3]. Thus, carbon deposition is thermodynamically favored and, in consequence, catalysts tend to rapidly deactivate and accumulate carbonaceous deposits at a high rate. In addition to the target reaction a significant number of (detrimental) side reactions involving reactants as well as products can occur.

$$CO_2 + H_2 \rightleftharpoons H_2O + CO \qquad \Delta H^0_{298K} = 41\ \mathrm{kJ/mol} \qquad (3\text{-}2)$$

$$2\,CO \rightleftharpoons CO_2 + C \qquad \Delta H^0_{298K} = -171\ \mathrm{kJ/mol} \qquad (3\text{-}3)$$

$$H_2O + CH_4 \rightleftharpoons 3\,H_2 + CO \qquad \Delta H^0_{298K} = 206\ \mathrm{kJ/mol} \qquad (3\text{-}4)$$

$$CH_4 \rightleftharpoons C + 2\,H_2 \qquad \Delta H^0_{298K} = 75\ \mathrm{kJ/mol} \qquad (3\text{-}5)$$

$$CO + H_2 \rightleftharpoons C + H_2O \qquad \Delta H^0_{298K} = 131\ \mathrm{kJ/mol} \qquad (3\text{-}6)$$

The side reactions with the highest impact on the product composition are the reverse water gas shift reaction (RWGS, (3-2)) and the Boudouard reaction (3-3). Water formed

in the RWGS can subsequently react with methane via steam reforming (3-4), producing a H_2 rich synthesis gas compared to the DRM. Cracking of methane (3-5), on the other hand, is an elementary step of DRM, leading to coke formation on the surface. Thus, methane cracking has to be considered as one of the key reactions in the formation of carbonaceous deposits and the deactivation of the catalyst by coking. The partial hydrogenation of CO (i.e., the reverse reaction of carbon gasification (3-6)) is another pathway that produces carbon deposits, especially at high concentrations of CO and H_2 [1, 4].

Thermodynamically, the deposition of coke is favored at lower temperatures, requiring the use reaction conditions above 873 K to minimize catalyst deactivation [5]. The deposition of coke becomes more favorable at higher pressures (especially above 10 bar), which are however essential for the overall process economics, as it reduces the number of compression steps required for the downstream processes typically operating at pressure levels between 20 and 70 bar. Noble metals, such as Pt or Ru show a lower tendency to coking compared to base metals [4, 6-8], but the significantly lower cost of base metal catalysts such as Ni make them preferred active components for industrial catalysts.

Ni is particularly prone to build up carbon-nano-tubes (CNT) under dry reforming conditions. These carbon deposits may limit the access to the active metal, may lead to reactor plugging, and in the worst case to destruction of reactor pipes. The rate of carbon formation has been associated with two key reactions, the recrystallization of carbon at the base metal surface and the dissociation of CH_4 at Lewis acid - base sites of the support [8]. With respect to the first, carbon nanotubes have been found to require a minimum size of the metal particles of above 2 nm to be formed under these conditions. Dissociation of CH_4 leading to coke formation can be minimized by reducing the concentration of Lewis acid sites on the support. It is obvious that at the high temperatures used for reforming, it is challenging to synthesize thermally stable catalysts and metal particles, which do not exceed the upper limit of 2 nm. Alternative conceptual approaches to enhance catalyst stability such as poisoning of the metal (SPARG process) and other means to reduce buildup of carbon at the catalyst have been vividly explored [9-13].

The high reaction temperatures, necessary for reaching sufficient conversion levels, require highly thermo-stable catalysts and we have previously reported new approaches to generate such catalysts based on Ni-containing hexaaluminates [14, 15]. The structure of hexaaluminates consists of spinel blocks into which active metals, e.g., Ni,

are inserted. Cation-containing (e.g. La^{3+}, Ba^{2+}, Sr^{+}) mirror planes between the spinel blocks further stabilize the structure. The layered structure of hexaaluminates provides a high thermal stability, making them attractive for high temperature processes [16-21]. As La^{3+} stabilized Ni-hexaaluminate have been identified as being particularly promising, they are explored and compared to Pt based catalysts with respect to the mechanism of carbon deposition, because the insight into this aspect of the reaction is important for further developments.

Thermodynamics guide to low pressures and high temperatures to favor DRM over carbon deposition. DRM has been mechanistically explored for many years [3, 7, 22, 23], however, most studies addressing coke deposition have been carried out at atmospheric pressure [24-26]. Cui et al. showed the temperature dependence of the DRM mechanism in a temperature range of 823 to 1123 K [27]. The authors postulated that the surface reaction of adsorbed CH_x with surface oxygen (originating from CO_2) becomes rate determining above 923 K, with the decomposition of CH_4 to CH_x* and H* being a fast step in the reaction network.

This fact points to the possibility that carbon deposition may involve reactions at these temperatures, which are thermodynamically less favored than the reactions involved in typical coke build up. Detailed studies have been reported by the group of Iglesia [28, 29], using isotope labeling to probe the importance of such reaction steps. In contrast to Cui et al. the activation of the C-H bond in CH_4 was identified as the rate determining step in CO_2 and H_2O reforming over Group VIII metals. In consequence, all other steps must have been faster under these conditions. Little is known about the impact of a higher overall pressure on CH_4 dissociation as well as the other reaction pathways. The ratio between the rates of reactions leading to the buildup and the removal of carbon species will determine the rate of coke formation on the catalyst surface.

The goal of this work is, therefore, to explore the pathways by which carbon deposition occurs at elevated pressure. A high-temperature stable Ni-hexaaluminate catalyst and a Pt/ZrO_2 catalyst are compared. To study the pathway of coke deposition, $^{13}CO_2$ was used to trace the origin of carbon formation. Using a previously established network of elementary surface reactions [30, 31], reaction pathways on Pt- and Ni-based catalysts were theoretically analyzed. The nature and concentration of carbon deposited were investigated by temperature programmed oxidation and electron microscopy. From the combination of the experiments and the theoretical calculations a reaction mechanism with special focus on pathways for buildup and removal of carbon deposits has been established for both metals.

3.2 Experimental

3.2.1 Synthesis

The Ni-hexaaluminates were synthesized following ref. [19]. Stoichiometric amounts of the metal nitrates (La, Ni, Al) were dissolved in water and then transferred into a solution of polyethylenglycole (PEG) in isopropanol. After drying the sample was calcined in air at 873 K (2 hours) and 1473 K (8 hours), to yield the Ni-hexaaluminate (confirmed by X-ray diffraction). The Pt/ZrO_2 catalyst has been synthesized and supplied by *hte GmbH*.

3.2.2 Chemisorption measurements

The fraction of catalytic active sites on the Pt/ZrO_2 catalyst was determined by TPO, according to the procedure described in [30]. The Ni dispersion measurements were done on samples pre-reduced in a stream of H_2 at 1073 K, and transferred into an automatized Sorptomatic 1990 system where the samples were reduced for another 3 hours at 101.3 kPa of H_2 at 673 K. The measurement was conducted at 308 K after evacuation of the system to less than 0.1 Pa. Each pressure increment (range 0.57-1.02 kPa) was equilibrated for 3-5 minutes. After the first run the sample was evacuated for 1 hour to a pressure below 0.1 Pa a second isotherm was measured. By extrapolating the linear part of the difference between the two isotherms to zero pressure the amount of adsorbed H_2 was calculated. The dispersion of Ni was determined assuming a dissociative H_2 adsorption (stoichiometry of 1 for $H/Ni_{surface}$) [32].

3.2.3 Scanning Electron Microscopy (SEM) and Transmission Electron Microscopy (TEM)

A high resolution FE-SEM (JEOL JSM 7500 F) with EDX (Oxford) was used to study the samples by SEM. TEM images were collected on a JEM-2010-JEOL microscope equipped with a LaB_6 electron source. The emerging electrons were accelerated with a voltage of 120 kV. The resolution of the microscope was 0.2 nm. The samples were dispersed in ethanol using an ultrasonic bath and subsequently applied drop wise to a copper grid supported film. The preparation methods for electron microscopy were identical for both techniques.

3.2.4 Kinetic experiments

The kinetic experiments were carried out in a recirculating system at an initial pressure of 1.0 MPa using a gear pump (Micropump Z-1830) to recycle the gases. The catalyst bed consisted of 20 mg of active material diluted in 80 mg of SiC held in place by two layers of quartz wool. The catalysts were reduced for 2 h at 1073 K using 20 vol.-% H_2 in N_2 (100 ml/min). The feed composition was 15 vol.-% CH_4, 15 vol.-% CO_2 and 70 vol.-% N_2. The experiments were carried out with gas mixtures of $^{12}CO_2$-$^{12}CH_4$-N_2 and $^{13}CO_2$-$^{12}CH_4$-N_2. In the experiments without isotope labelled reactants the system was flushed with N_2 at atmospheric pressure (100 kPa) and then filled to 250 kPa with $^{12}CO_2$, to 400 kPa with $^{12}CH_4$, and finally to 1.0 MPa with N_2. For experiments with isotope labelled reactants, the system was first evacuated using a membrane pump (*Vacuubrand*). 150 kPa of $^{13}CO_2$ and 150 kPa of $^{12}CH_4$ were dosed into the system and finally the reactor was pressurized to 1.0 MPa with N_2. To obtain a uniform distribution of the reactant in the system the gasses were recycled through the system in the bypass mode for 1 hour before starting the reaction. The product composition and the isotope composition was analyzed by an online GC-GC/MS system (Shimadzu 2010 and Shimadzu 2010 Plus) and a combination between FID and TCD. The gases in the system were recycled with a recycling ratio near infinity (i.e., only negligible amounts of gas were removed from the system for gas analysis) and conversion per cycle was kept below 5% by maintaining a flow of 200 ml/min. The reactor system (V_{total} = 345 ml) was kinetically described as a batch reactor.

3.2.5 Temperature programmed oxidation (TPO)

The source of the coke formation was studied by TPO of the samples after reaction with isotope labelled $^{13}CO_2$ and $^{12}CH_4$. The samples were ground, placed in a quartz tube and after conditioning at ambient temperature for 30 min in a flow of 20 vol.-% O_2 in He (30 ml/min) heated in a ceramic oven (*Horst GmbH*) to 1273 K with a rate of 10 K/min. To identify the source of coke formation the evolving gases were analyzed by a mass spectrometer (*Balzers QME 200*) following the partial pressures for m/z 44 for $^{12}CO_2$ and m/z 45 for $^{13}CO_2$.

3.2.6 Reaction flow analysis

Reaction flow analysis was used to identify the main pathway for the conversion of the reactants and the formation of the products. The recently developed surface reaction mechanisms for dry reforming on Pt [30] and Ni [31] were extended to include reactions

with isotopic labeled compounds, which were treated without accounting for kinetic isotope effects (i.e. the same rate constants were used for reactions with ^{12}C and ^{13}C). The reaction mechanism for Pt contains 12 gas-phase and 19 surface species, including 3 isotopes in the gas phase and 7 in the surface species that can undergo together 106 reactions. The Ni reaction mechanism contains 88 reactions among 9 gas-phase species (3 isotopes) and 23 surface species (9 isotopes). The derivation of the rate constants is described in forthcoming papers. The general methodology is described in refs. [30] and [31] for Pt and Ni, respectively.

For reactions on the catalytic surface, the molar production rate, $\dot{s}_i$, of a chemical species *i* can be expressed by

$$\dot{s}_i = \sum_{k=1}^{K_s} \nu_{ik} k_{f_k} \prod_{j=1}^{N_g+N_s} c_j^{\nu'_{jk}} \qquad \nu_{ik} = \nu''_{ik} - \nu'_{ik} \tag{7}$$

Here, K_s is the number of surface reactions including adsorption and desorption, c_i are the concentrations of the different species given in mol m^{-2} for the N_s adsorbed species and in mol m^{-3} for the N_g gaseous species, ν'_{ik} and ν''_{ik} are the stoichiometric coefficients of the left and right side of the reaction equation and k_{f_k} is the (forward) rate constants of reaction *k.*

In a reaction flow analysis, the individual contributions of a single reaction *k* to the production or depletion of a chemical species *i* are analyzed. A simple presentation of the results of such an analysis are the percentages of the depletion of a single species *i* by a certain reaction *k*, i.e.,

$$E_{ik}^{flux} = -100\% * (\nu_{ik} k_{f_k} \prod_{j=1}^{N_g+N_s} c_j^{\nu'_{jk}}) / \dot{s}_i \quad \text{for all } \nu_{ik} < 0. \tag{8}$$

Usually, only the most significant reactions are given in the reaction analysis.

3.3 Results

3.3.1 Structural properties

The structural properties of the catalysts after pretreatment in 20 vol.-% H_2 in N_2 are compiled in Table 3-1. The BET surface areas of the two catalysts were 7 m^2/g for the Ni-hexaaluminate and 8.5 m^2/g for the Pt/ZrO_2. The dispersion after the pretreatment in

H_2 at 1073 K for 2 h was 0.5 % for the Ni-based and 8.5 % for the Pt-based catalysts. The pretreatment and reaction temperatures were above the Tamman-Temperature of Ni (863 K), which together with the very low specific surface area of the support is speculated to have contributed to the sintering of the Ni particles to an average size of 20 nm. To account for the low dispersion of Ni, the metal loading of the Ni samples was chosen to be 5 times higher than for Pt in order to result in the same concentration of active sites on both samples.

Table 3-1 Structural properties of the catalysts after activation

Material	Metal loading [wt.-%]	Surface area [m^2/g]	Dispersion [%]	Active metal [$mol/g_{catalyst}$]
Ni	5	7	0.5	$4.3 \cdot 10^{-6}$
Pt	1	8.5	8.5	$4.4 \cdot 10^{-6}$

3.3.2 Kinetic results

The partial pressures of the main gas phase components during DRM over Pt/ZrO_2 are shown in Figure 3-1. The reactions involved are not volume constant and, therefore, the pressure inside the system increased throughout time on stream. To account for this, the partial pressures were normalized to the partial pressure of N_2 added as marker component. The depletion of the reactants CH_4 and CO_2 was accompanied by the evolution of CO, H_2 and H_2O, indicating that dry reforming and RWGS occurred in parallel. Therefore, the initial formation rate of CO was slightly higher compared to that of H_2.

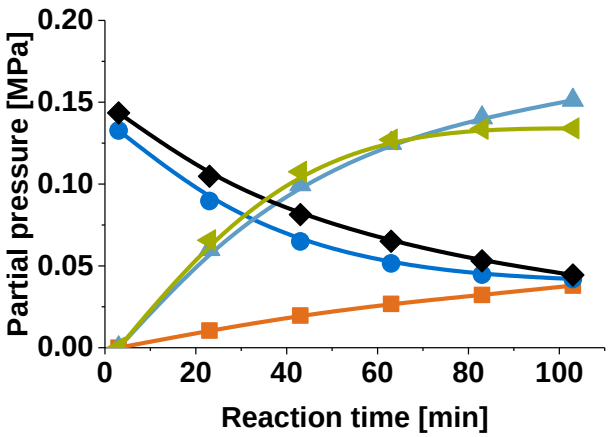

Figure 3-1 Gas phase composition as a function of reaction time for the dry reforming over Pt/ZrO_2 (◆ CH_4, ● CO_2, ◀ CO, ▲ H_2, ■ H_2O) at 1123 K and 1.0 MPa total pressure

The results obtained with the Ni catalyst are shown in Figure 3-2. At the start of the reaction, the CO_2 concentration decreased faster than that of CH_4 and, simultaneously, the CO concentration increased in a more pronounced way. On Ni catalysts the activation of methane was slower compared to Pt, which resulted in a lower H_2/CO ratio (Figure 3-2). With longer reaction time the concentrations of CO_2 and CH_4 as well as of H_2 and CO converged towards the equilibrium values on both catalysts.

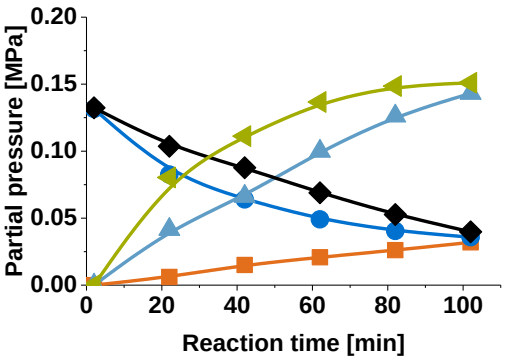

Figure 3-2 Gas phase composition for the dry reforming over the Ni aluminate catalyst at 1123K and 1.0 MPa (◆ CH_4, ● CO_2, ◀ CO, ▲ H_2, ■ H_2O)

During the reaction a significant concentration of H_2O was formed. At the same time, the concentration of H_2 was not sufficiently lower than that of CO in order to be able to relate the formation of H_2O to the RWGS only. Note that over Pt the H_2 concentration even exceed the CO concentration at the end of the reaction. To investigate the distribution of C, O and H in the products formed, the mass balances for the reactions over Pt and Ni were calculated and are shown in Figure 3-3 and Figure 3-4. Over Pt an initial decrease of about 5% in the mass balances for O and H was observed over the reaction time. The C balance decreased constantly and reached about 93% at the end of the reaction, while the balances for H and O slightly increased and reached 98% towards the end of the reaction.

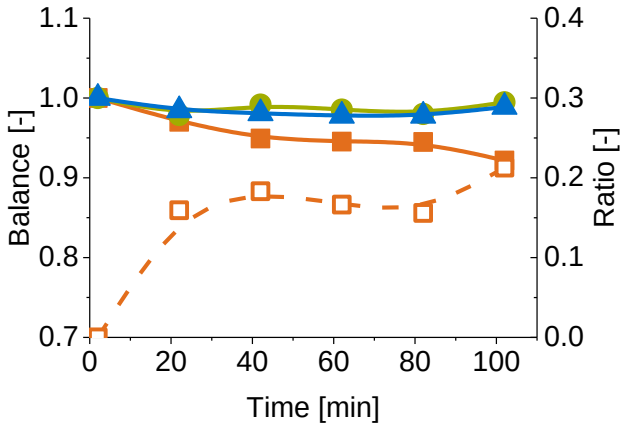

Figure 3-3 Gas phase mass balance of carbon (■), hydrogen (▲) and oxygen (●) in the reaction over Pt (left axis) and (□) ratio between C species deposited on the catalyst per CH_4 converted (right axis)

On Pt carbon species were immediately formed in the beginning of the reaction, while on Ni a short imitation period was observed before coke formation started. Over Ni the C balance was initially almost completely closed, while the H and O balances decreases about 5%. After 40 minutes the C mass balance started to decrease rapidly reaching 86% at the end of the reaction, while the H and O balances increased to around 97%.

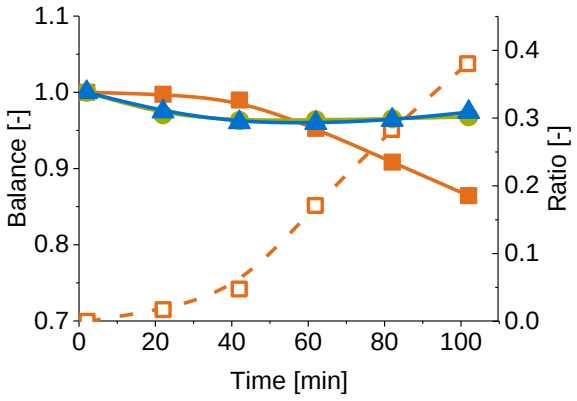

Figure 3-4 Gas phase mass balance of carbon (■), hydrogen (▲) and oxygen (●) in the reaction over Ni (left axis) and (□) ratio between C species deposited on the catalyst per CH_4 converted (right axis)

This reflects in the ratio of deposed carbon to converted CH_4, also plotted in Figure 3-3Figure 3-4. Pt initially forms rather much carbon from the converted reactants, but after this phase of 20 min, the ratio does not change any more. Contrary the Ni catalyst builds up rather little carbon at the beginning of the reaction but the deposition compared to the converted CH_4 starts off during reaction and increases with a steep slope from then on. This shows that the reaction over the noble metal proceeds steadier and therefore the carbon deposition is reduced. Finally, a significant fraction of carbon (about

0.4 mol C per mol CH_4 converted) is formed during the reaction over the Ni catalyst, while on Pt the coke formation was lower (about 0.2 mol C per mol CH_4 converted). The small decrease in the O and H mass balances indicates that the coke species formed also contain a small concentration of H and O (about 0.05 mol H and 0.02 mol O per mol CH_4 converted).

3.3.3 Reaction rate calculation

The reaction rates normalized to the concentration of accessible metal atoms are compiled in Table 3-2. The initial rate of CO_2 consumption as well as the initial formation rate of CO (from CO_2 and CH_4) were similar for both catalysts. In contrast, the rates for the consumption and formation of the three hydrogen containing components (i.e., CH_4, H_2 and H_2O) differed significantly. The activation for CH_4 was 1.5 times faster on Pt than on Ni. H_2 was produced with a rate of 57mol/(sec*mol_{metal}) on Pt, while on Ni only 33 mol/(sec*mol_{metal}) was observed. The same applied for the formation of water produced from hydrogen via the secondary RWGS, i.e. 11 mol/(sec*mol_{metal}) for Pt and 5 mol/(sec*mol_{metal}) for Ni based catalysts.

Table 3-2 Initial reaction rates for the reaction at 1123 K and 1.0 MPa

Turnover frequency [mol/(sec*mol(metal)]	CH4	CO2	CO	H2	H2O
Pt	37	39	64	57	11
Ni	24	40	63	33	5

With increasing reaction time, the conversion and formation rates diminish as the concentrations in the gas phase approached the thermodynamic equilibrium. The resulting rates can be found in the supplementary information.

3.3.4 Isotope labelling experiments

To study the mechanism of coke deposition and its removal from the catalyst surface the reaction was carried out with isotope labeled $^{13}CO_2$. Six potential gas phase components can be formed from the reaction between $^{13}CO_2$ and $^{12}CH_4$, i.e., $^{12}CO_2$, $^{13}CO_2$, $^{12}CH_4$, $^{13}CH_4$, ^{12}CO and ^{13}CO. The kinetic results of DRM are plotted in Figure 3-5 and Figure 3-6 for Pt and Ni, respectively. During the conversion of $^{13}CO_2$ and $^{12}CH_4$ on the Pt based catalyst significant amounts of ^{12}CO and ^{13}CO were formed. Note that the concentration of ^{13}CO increased more rapidly than the one of ^{12}CO. As shown by the formation of water, RWGS occurred simultaneously and therefore, more CO was initially formed from $^{13}CO_2$ than from $^{12}CH_4$. The ratio between the concentrations of these two CO isotopes

approached unity at higher conversion levels and additionally small amounts of $^{12}CO_2$ and $^{13}CH_4$ were formed

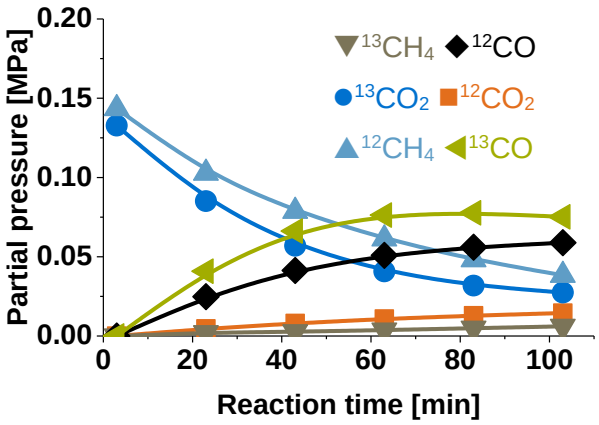

Figure 3-5 Isotope composition in the reaction of $^{13}CO_2$ with $^{12}CH_4$ over Pt/ZrO_2 at 1123 K and 1 MPa.

The concentration profiles for the reactants and products of the DRM reaction over Ni (Figure 3-6) differed slightly from those over Pt. The rate of methane activation was slower and as a consequence the ^{12}CO concentration (formed from $^{12}CH_4$) increased less pronounced than the concentration of ^{13}CO (formed from $^{13}CO_2$). During the reaction on Ni ^{13}CO was always present in excess and the formation of $^{13}CH_4$ and $^{12}CO_2$ was slower. Compared to the reactions on Pt the concentration of $^{13}CH_4$ hardly increased during the first 60 minutes.

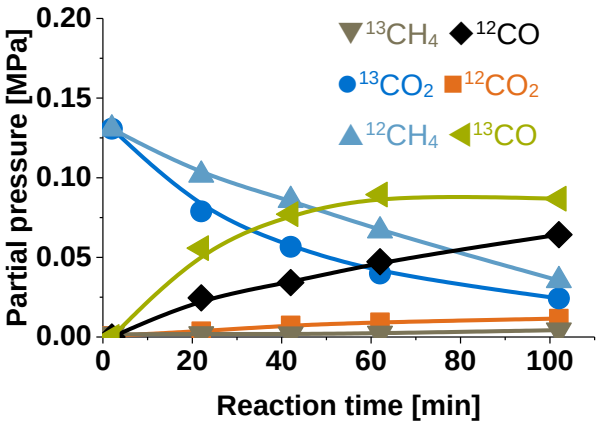

Figure 3-6 Isotope composition in the reaction of $^{13}CO_2$ with $^{12}CH_4$ over the Ni catalyst at 1123 K and 1 MPa.

The rates for the consumption and formation of the isotope labeled reactants and products can be found in Table 3-3. The rate of $^{13}CO_2$ conversion and the rate of CO formation (including ^{13}CO and ^{12}CO) were similar on both catalysts. The ratio between ^{13}CO and ^{12}CO, however, was lower on the Pt catalyst. The rate of CH_4 conversion was identical to that of the experiments with unlabeled reactants, while the rate of CO_2 conversion was slightly higher. The (initial) formation of $^{13}CH_4$ and $^{12}CO_2$ indicates a rapid isotope scrambling on Pt and Ni under these conditions.

Table 3-3 Initial production and conversion rates for all gas phase carbon components in the reaction of $^{13}CO_2$ with $^{12}CH_4$

Turn over frequency [mol/(sec*mol$_{metal}$)]	$^{13}CO_2$	$^{12}CH_4$	$^{12}CO_2$	$^{13}CH_4$	^{13}CO	^{12}CO	H_2	H_2O
Pt	43	37	3.5	0.4	39	26	57	11
Ni	42	24	2.3	0.2	44	19	33	5

To eliminate the time dependence from the isotope scrambling, the isotope ratios are displayed as a function of the CH_4 conversion in Figure 3-7. In order to determine the isotope contents, the concentrations of the isotope labeled carbon species were normalized to the total concentration of the respective species, as given in equations (3-7) - (3-9).

$$\frac{^{13}CO_2}{CO_2} = \frac{c(^{13}CO_2)}{c(^{12}CO_2) + c(^{13}CO_2)} \quad (3\text{-}7)$$

$$\frac{^{13}CH_4}{CH_4} = \frac{c(^{13}CH_4)}{c(^{12}CH_4) + c(^{13}CH_4)} \quad (3\text{-}8)$$

$$\frac{^{13}CO}{CO} = \frac{c(^{13}CO)}{c(^{12}CO) + c(^{13}CO)} \quad (3\text{-}9)$$

The $^{13}CO_2$ content decreased over Pt (Figure 3-7, a) as well as over Ni (Figure 3-7, b) from a value near 1 (i.e., the reaction was started with pure isotope labeled $^{13}CO_2$). On the other hand, the ratio for CH_4 started from a value near 0 and increased at higher conversion levels (larger than 50 % on Pt and larger than 60 % on Ni), indicating that a small concentration of $^{13}CH_4$ is produced in the reactions. The ^{13}CO concentration was always higher than that of ^{12}CO and approached an equal level on both catalysts at

higher conversion. At low conversion levels the ratio of $^{13}CO/^{12}CO$ was higher on Ni than on Pt, which reflects the more difficult activation of $^{12}CH_4$ with respect to $^{13}CO_2$.

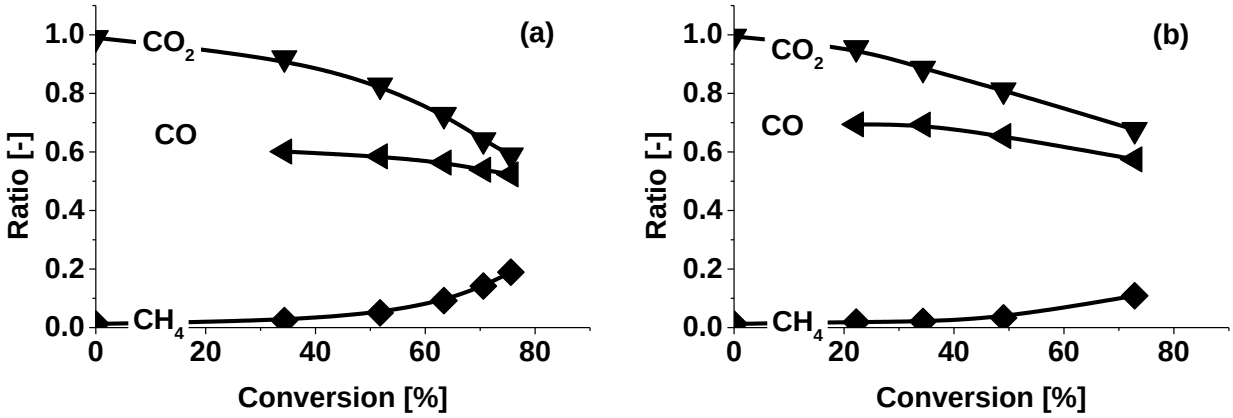

Figure 3-7 Isotope ratio for Pt (a) and the Ni (b) catalyst. For both materials the scrambling of the isotopes of CO_2, CH_4 and CO was similar, while the process was faster on Pt than on Ni.

3.3.5 Reaction flow analysis

The reaction mechanism used includes the elementary reaction steps in the reaction of CH_4 and CO_2 during reforming (dry and steam), water-gas shift, carbon formation, methane cracking and gasification of carbon by steam. Reaction pathways for the formation of surface carbon are also described. The results of the reaction flow analysis for dry reforming on Pt and Ni based catalysts are shown in Figure 3-8. The kinetic data and equilibrium constants used were taken from refs. [30] and [31].

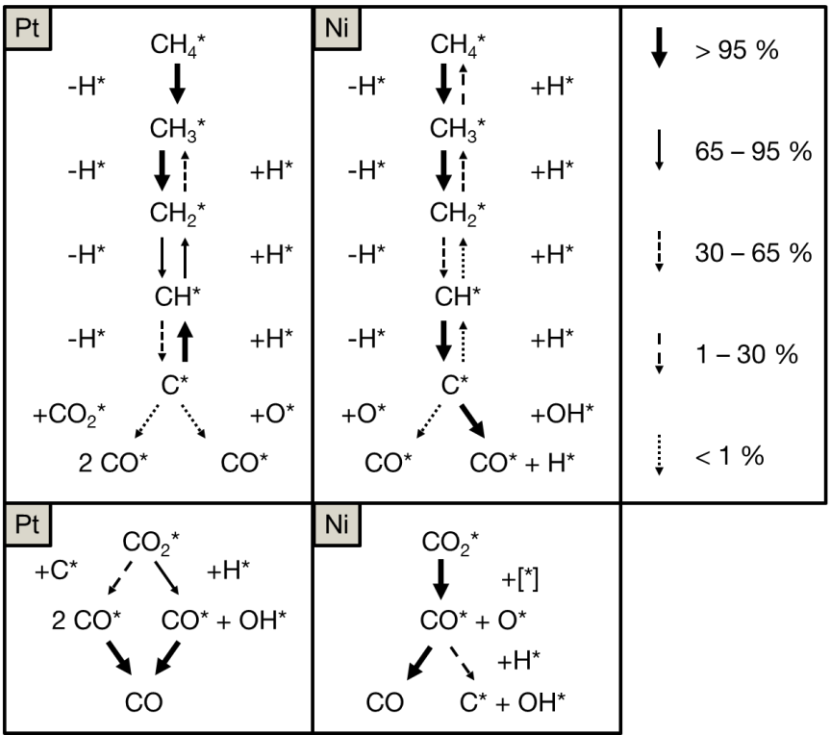

Figure 3-8 Reaction flow analysis for CO_2 and CH_4 showing the differences in the mechanisms for the DRM reaction on the two active metals. The arrows describe the importance of the respective reaction for the specific surface species. The thicker the arrow is displayed the more probable it is that the reaction proceeds along this reaction route according to Eq. 8. This graph includes only surface reactions; adsorption and desorption steps are not included.

On Pt the reaction pathway for CH_4 is seen to proceed via a dissociative adsorption and the successive cleavage of C-H bonds to lead to adsorbed C* and H* species. CO_2 may react to CO* and surface C* (Boudouard reaction) or to CO* and OH* surface species (RWGS reaction). In both cases the reaction of CO_2* to CO* requires a co-reactant to proceed. The C* species on the surface formed from CH_4 are oxidized to CO* by the reaction with CO_2* or O* surface species. For Ni the reaction mechanism includes the reactions of partial oxidation, steam and dry reforming of methane and is based on the key reaction intermediate which is adsorbed atomic oxygen O*. The reaction on Ni proceeds via the successive cleavage of the C-H bonds of CH_4 to yield CH_x surface species and in contrast to Pt, C* is the prominent surface species, which reacts with OH* to form CO and* and H*. Note that although this reaction pathway has significantly higher probability reactions of C* with O* or H* are not excluded.

The reaction flow analysis predicts the overall surface concentration of CO_2-derived species to be larger for Ni than for Pt. Under the given conditions adsorbed CO_2*-Pt reacts with 0.1 % probability to other surface species, while to 99.9 % it desorbs into the gas phase. On the other hand, CO_2*-Ni reacts with a probability of 82.7 % to other

species, while desorption occurs with a probability of 17.3 %. One has to note here that desorption of CO_2 is not considered in Figure 3-8, and therefore, the numbers displayed are the total contributions of the individual surface reactions (of the 0.1 % on Pt and the 82.7 % on Ni). For CH_4 a difference was not observable between the two metals as desorption only occurs to a minor extent and thus the coverage of the metal in CH_4 can be assumed to be similarly high. Exact values for the probabilities of desorption and surface reactions can be found in the supplementary information.

3.3.6 Temperature programmed oxidation

TPO of carbon formed during DRM (using $^{13}CO_2$ and $^{12}CH_4$ as reactants) was used to determine the source and concentration of carbon deposited on the catalyst. The TPO profiles of the two catalysts after 2 h of DRM are shown in Figure 3-9 (a) for $^{12}CO_2$ (formed from $^{12}CH_4$) and (b) for $^{13}CO_2$ (formed from $^{13}CO_2$). Both TPO profiles of ^{12}C and ^{13}C deposited on Ni and Pt showed a main peak at 893 K, which is typical for the oxidation of carbon with a nano-tube structure. Only minor contributions were observed between 613 and 623 K, attributed to oligomeric and polymeric carbon [33]. This indicates that, regardless of the kind of active metal (Ni or Pt) or the source of carbon (CH_4 or CO_2), the majority of the carbon species is present on the catalyst surface in the form of carbon-nano-tubes.

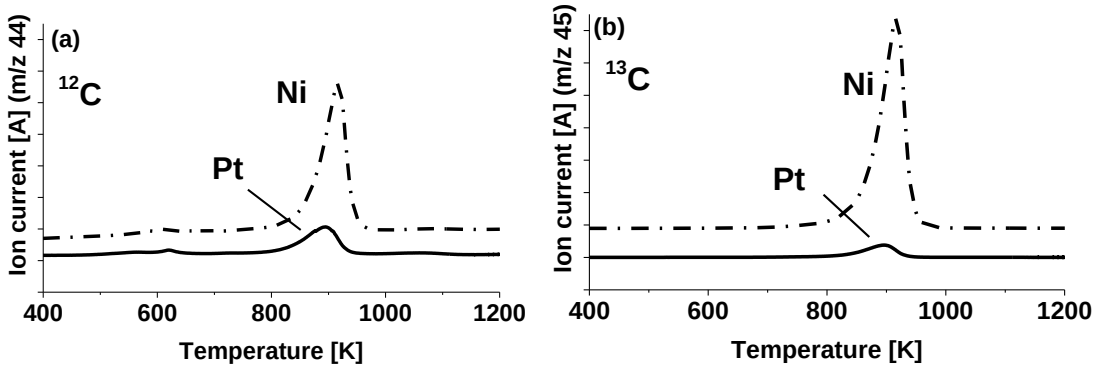

Figure 3-9 TPO profiles of the coke species formed on Ni (dashed) and Pt (solid) for (a) ^{12}C and for (b) ^{13}C after 2 h of reaction between $^{13}CO_2$ and $^{12}CH_4$ at 1123 K. For terms of visibility an offset has been added to the Ni data.

We hypothesize that, due to their higher structural order, carbon whiskers contain less H and O than oligomeric and polymeric carbon residues. TPO shows that a significantly higher amount of carbon is present on Ni than on Pt after conversion of 133 mg CH_4 in the DRM reaction. Taking into account different response factors for the masses 44

($^{12}CO_2$) and 45 ($^{13}CO_2$), the calculated ratio between $^{12}C/^{13}C$ was 0.36 on Ni, which indicates that 73% of the carbon present was created from the isotope labeled $^{13}CO_2$ and 27% originated from $^{12}CH_4$. For Pt a higher fraction of ^{12}CO was observed during the TPO, with more than 97% of the coke formed from the $^{12}CH_4$ and less than 3% from $^{13}CO_2$.

3.3.7 Electron microscopy

Scanning electron microscopy of the Ni catalyst shows the high stability of the material under the severe reaction conditions. The hexagonal patterns of the structure were observed before (Figure 3-10.1a) and after (Figure 3-10.1b) the DRM experiments. Additionally, carbon nano-tubes were resent after the reaction.

As it has been shown that carbon grows from the surface of the Ni containing material, but does not cover the metal surface [34], we hypothesize that the surface of the catalysts is mostly free of carbon deposits despite the fact that a substantial concentration of coke was deposited. The size and shape of the primary ZrO_2 particles before (Figure 3-10.2a) and after (Figure 3-10.2b) reaction also indicated only minor structural changes. The edges of the grains, however, were smoother after the reaction and minor amounts of coke deposits in the form of carbon-nano-tubes were observable.

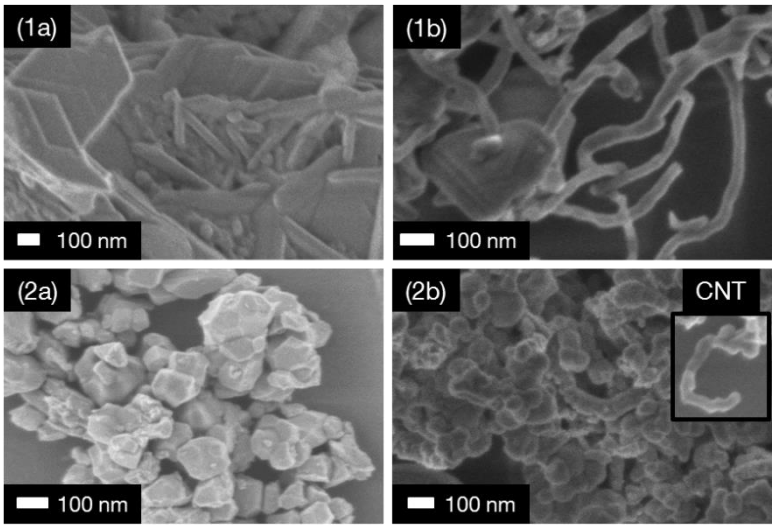

Figure 3-10 SEM of the Ni (1) and the Pt (2) catalysts before (a) and after (b) reaction

3.3.8 Transmission electron microscopy

The size and shape of the metal particles, created during pretreatment and reaction, were investigated by TEM. In the as-synthesized Ni material (Figure 3-11.1a) the layered structure of the hexaaluminate crystals is clearly visible. The distance between the layers of about 12 – 13 Å is in agreement with the (002) lattice plane distance of 11 Å for La^{3+} stabilized Ni-hexaaluminates [35]. After reaction, large metallic Ni particles were observed (Figure 3-11.1b), while the layers in the oxide were not visible. This indicates that Ni has been removed from the hexaaluminate structure during pretreatment and reaction and that aluminum filled the voids generated in the crystal structure. Because the contrast provided by Al in TEM measurements is much lower than that of Ni, we expect that the layered structure is still present, but not visible. Additionally, fibrous forms were observed, which were attributed to the carbon nanotubes formed during dry reforming.

In agreement with SEM, the support of the Pt/ZrO_2 catalyst did not markedly change (Figure 3-11.2). Platinum oxide (2a) on the surface was reduced and small Pt particles of only 2-4 nm were formed under the DRM conditions (2b). Features attributable to carbon were not observed.

Figure 3-11 TEM pictures of the Ni and the Pt catalyst. Before reaction the Ni-hexaaluminate structure is good visible (1a) and after reaction large particles larger than 20 nm have been formed (1b). In the as-synthesized Pt (2a) those particles are not visible, that one can see after reaction (2b).

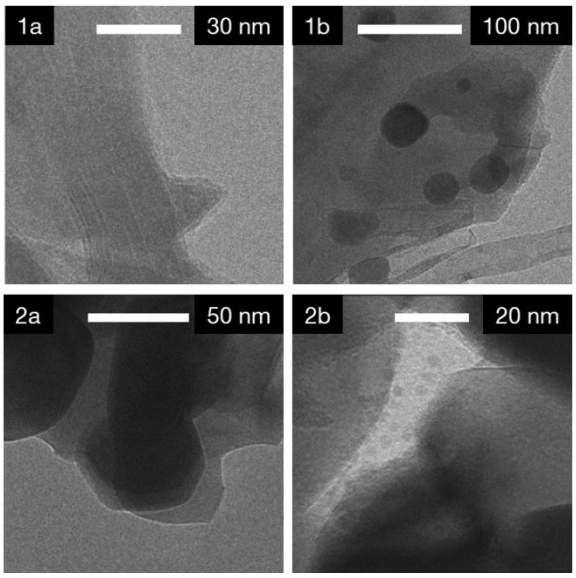

Figure 3-12 TEM pictures of the Ni and the Pt catalyst. Before reaction the Ni-hexaaluminate structure is good visible (1a) and after reaction large particles larger than 20 nm have been formed (1b). In the as-synthesized Pt (2a) those particles are not visible, that one can see after reaction (2b).

3.4 Discussion

While both metals are active and selective in DRM, the difference in the catalytic properties with respect to the individual reaction steps between Pt and Ni was remarkable. For both metals the particle size was sufficiently large to be able to exclude a direct influence of the support on the catalytic rates [3, 8].

First, the initial rates will be discussed (Table 2). The initial rates of CO_2 conversion were identical on both catalysts. While the rate of CH_4 conversion on Pt was almost equal to that of CO_2 conversion, it was significantly lower on Ni which can be related to an energetically more difficult CH cleavage [36, 37]. The turnover frequency to form CO must be the sum of these two rates. However, the rate of CO formation was only 64 s^{-1} compared to 76 s^{-1} as expected from the sum of the two rates. Similarly, the formation rate of hydrogen containing species (H_2 and H_2O) with 68 s^{-1} was below the value of 74 s^{-1}, which would be expected based on the conversion rate of CH_4. This is in line with the fact that a substantial fraction of carbon has not been converted to synthesis gas, but was deposited as carbon on the catalyst. The difference between H_2 expected and observed points to the fact that the carbon deposited contains still a fraction of hydrogen associated with it. Such hydrogen cannot be present on carbon whiskers or fibers.

For the Ni based catalyst the difference between CO_2 and CH_4 rates were much larger, but the sum of these two reaction rates was almost perfectly equal to the rate of CO formation, pointing on first sight to only a minimal fraction of independent formation of coke from one of the reactants. The difference between the observed (38 s^{-1}) and the estimated H_2/H_2O formation rates (48 s^{-1}), led us to conclude that a larger concentration of carbonaceous deposits containing hydrogen must exist in this case. Such a larger concentration is in line with the expected tendency of Ni to form surface carbon. It should be emphasized that the excellent agreement between CO formation rates (63 s^{-1}) and the consumption rates of CH_4 and CO_2 (64 s^{-1}) implies that this carbon formed must also contain oxygen. The concentration of H_2O increases steadily with time on stream even though conversion of CH_4 and CO_2 slows down at lower concentrations. This indicates that H and O might be released from the surface bound (H and O rich) polymeric carbon in the form of water, forming the highly ordered whiskers observed in the TPO and SEM after reaction. The mass balances also confirm that the coke species contain a certain fraction of H and O. On Pt coke is formed with a constant rate leading to a steady decrease in the C mass balance over the reaction time. On Ni an induction period for the coke formation was observed, afterwards the coke formation in the form of carbon nanotubes started with a higher rate compared to Pt. This observation suggests that the

formation of carbon deposits by reverse Boudouard reaction from CO* surface species is favored by high product concentrations. During the reaction the mass balances for O and H increased towards the end of the reaction as a result of the conversion of H and O rich coke species into carbon nano tubes.

The reaction flow analysis indicates that CH_4 decomposes on both metals to carbon via C-H bond cleavage. The preferred surface species are CH* and CH_2* on Pt and C* on Ni. On Pt the C* surface species are oxidized with surface O* species to CO* or react with adsorbed CO_2* to CO* via the Boudouard-reaction. C* is oxidized on the Ni surface to CO* with OH* species, formed from the decomposition of H_2O, while the direct oxidation of C* with O* to CO* is only a minor reaction route. The conversion of CO_2 on Pt mainly occurred by a reaction with H* to form CO* and OH* surface species, while the Boudouard-reaction towards CO* took place with lesser probability. In contrast on Ni the main reaction route of CO_2 is the dissociative adsorption to form CO* and O* surface species, while no co-reactant is needed for the activation of CO_2*. Reactions that lead from CO* directly to C* do not occur on Pt, while C* can be formed on Ni from CO* and H* creating additional OH*. Several effects are influencing the significantly higher coke formation on Ni compared with Pt: (a) possible carbon formation from CO*, (b) lower probability on Ni for hydrogenation of C*, (c) the primary removal route of surface carbon species via the reaction of C* with OH* and (d) the overall higher carbon concentration due to reduced desorption probability of CO_2*. It should be emphasized that the network of the reaction flow analysis contained a much larger variety of reaction paths, but only the ones discussed here were sufficiently rapid to be significant in the overall kinetics.

TPO of the catalysts after reaction with isotope labelled $^{13}CO_2$ and $^{12}CH_4$ showed that CO_2 and CH_4 contribute to coke formation and that the source of the main fraction of the coke varied with the catalytically active metal. For Ni, 73 % of the coke species resulted from the dissociation of CO_2 and only one fourth from the dissociation of $^{12}CH_4$. The fact that a significant fraction of CO_2 dissociated via CO* to C* suggests that the interaction of Ni with CO* must be sufficiently strong to allow full dissociation. These results are in line with the lower desorption probability of CO_2 on Ni compared to Pt and leads to the conclusion that the surface carbon coverage (also in CO* and CO_2*) is significantly higher on the base metal. On Pt the latter reaction pathway was concluded to less important, i.e., it accounted for only 2 % of the total carbon deposited. We therefore speculate that the higher fraction of carbon species formed from CO_2* is one of the reasons for the higher carbon deposition on Ni.

The formation of $^{13}CH_4$ and $^{12}CO_2$ during DRM of $^{13}CO_2$ and $^{12}CH_4$ led us to conclude that all reactions were fully reversible at high conversions, which is in line with earlier experiments using CD_4 [28]. The lower CH_4 and similar CO_2 conversion rate on Ni compared with Pt led to a lower $^{12}CO/^{13}CO$ ratio on Ni. In order to form $^{13}CH_4$, $^{12}CO_2$, but also ^{12}CO and ^{13}CO under the conditions applied (i.e., reaction between $^{13}CO_2$ and $^{12}CH_4$), the reactants have to be dissociated to surface carbon. The concentration of $^{13}CH_4$ was very low, thus, the hydrogenation of carbon is concluded to be significantly slower than the dehydrogenation of CH_4*.

The gasification of C* is concluded to be more facile on Pt, because the formation rates of $^{12}CO_2$ and $^{13}CH_4$ were twice as high as for Ni, which suggests that the higher stability of noble metal catalysts against coking under these conditions is related with the easier gasification of surface carbon. On Ni the concentration of $^{13}CH_4$ increased only very slowly during the DRM reaction, which indicates that the hydrogenation of surface carbon was more difficult. It is unclear at present, whether a lower concentration of H* or a larger energetic barrier is responsible for these lower rates, in line with the numerical calculations.

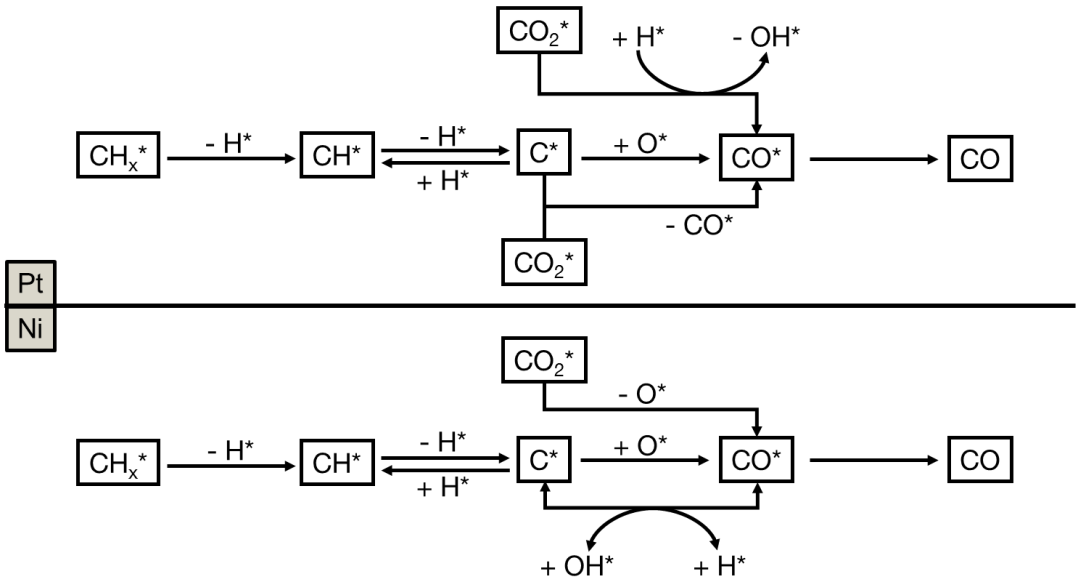

Figure 3-13 Block diagram of the reactions forming and removing carbon

While the significantly higher CO_2* concentration on the surface can be the reason for its notable contribution to the carbon formation, the differences in the total scrambling and the relative composition of the coke suggest different pathways on both metals, despite

C* species are common intermediates on both catalysts. It is also unclear whether a direct route or an indirect route will dominate. From the kinetic data, the investigations of the coke formed on the catalysts and the numeric calculations we propose a network of surface reactions leading from CO_2 and CH_4 to CO for both active metals, which is shown in Figure 3-13. While both reaction networks proceed via the complete dehydrogenation of CH_4, the removal of C* and the activation of CO_2* follow different pathways. On Pt the formation of C* from CO* is not possible, while CO* can react with H* to form C* and OH* on Ni. At high product concentrations the surface will be mainly covered with CO* and H* and therefore this reaction pathway possibly becomes a major route to carbon deposition on Ni.

3.5 Conclusions

Ni and Pt based catalysts were active in DRM, but the formation of coke was significantly higher on the base metal catalyst. For both metals the reaction proceeds via cleavage of the C-H bonds in CH_4, the preferred surface species were C*on Ni and CH* and CH_2* on Pt. The lower rate of CH_4 conversion on Ni compared to Pt is attributed to the energetically more demanding C-H bond cleavage on the base metal. In contrast the (initial) rates of CO_2 conversion were identical on both catalysts. The activation of CO_2 on Ni proceeds via a dissociative adsorption yielding to CO* and O* surface species, while on Pt the reaction proceeds with H*, formed via the CH_4 dissociation, to CO* and OH* surface species. The formation of surface carbon species from CO* is possible on Ni, while this reaction does not occur on Pt. TPO using isotope labeled reactants confirmed that on Ni the main fraction of coke was formed from dissociation of CO_2, while on Pt the main fraction of coke species was formed from the dissociation of CH_4. The generally lower formation of coke on Pt results from the higher gasification rate of C*species.

3.6 Acknowledgements

The authors gratefully acknowledge the funding financial support of the German government (Bundesministerium für Wirtschaft und Technologie, Fördernummer 0320327856D). We thank our project partners at Linde AG and the BASF SE fruitful discussions. Also Franz-Xaver Hecht for the chemisorption measurements, Eva Schachtl, Katia Rodewald and Martin Neukamm for the SEM and Elisabeth Hanrieder and Sebastian Grundner for the TEM measurements. We express special thanks to Matthias Steib for his help on the isotopic measurements.

3.7 Literature

[1] M.C.J. Bradford, M.A. Vannice, Cat. Rev. - Sci. Eng., 41 (1999) 1.
[2] K. Takehira, T. Shishido, P. Wang, T. Kosaka, K. Takaki, J. Catal., 221 (2004) 43.
[3] J.H. Bitter, K. Seshan, J.A. Lercher, J. Catal., 183 (1999) 336.
[4] M.-S. Fan, A.Z. Abdullah, S. Bhatia, ChemCatChem, 1 (2009) 192.
[5] S. Therdthianwong, C. Siangchin, A. Therdthianwong, Fuel Process. Technol., 89 (2008) 160.
[6] F. Pompeo, N.N. Nichio, M.M.V.M. Souza, D.V. Cesar, O.A. Ferretti, M. Schmal, Appl. Catal., A, 316 (2007) 175.
[7] J.A. Lercher, J.H. Bitter, W. Hally, W. Niessen, K. Seshan, in: W.N.D.E.I. Joe W. Hightower, T.B. Alexis (Eds.) Stud. Surf. Sci. Catal., Elsevier1996, pp. 463.
[8] W. Hally, J.H. Bitter, K. Seshan, J.A. Lercher, J.R.H. Ross, in: B. Delmon, G.F. Froment (Eds.) Catalyst Deactivation, 1994, pp. 167.
[9] N. Salhi, A. Boulahouache, C. Petit, A. Kiennemann, C. Rabia, J. Soc. Alger. Chim., 20 (2010) 121.
[10] A. Horvárth, G. Stefler, O. Geszti, A. Kienneman, A. Pietraszek, L. Guczi, Catal. Today, 169 (2011) 102.
[11] S. Corthals, J. Van Nederkassel, H. De Winne, J. Geboers, P. Jacobs, B. Sels, Appl. Catal., B, 105 (2011) 263.
[12] C. Daza, O. Gamba, Y. Hernández, M. Centeno, F. Mondragón, S. Moreno, R. Molina, Catal. Lett., 141 (2011) 1037.
[13] C. Crisafulli, S. Scirè, S. Minicò, L. Solarino, Appl. Catal., A, 225 (2002) 1.
[14] T. Roussière, K.M. Schelkle, S. Titlbach, G. Wasserschaff, A. Milanov, G. Cox, E. Schwab, O. Deutschmann, L. Schulz, A. Jentys, J. Lercher, S.A. Schunk, ChemCatChem, 6 (2014) 1438.
[15] T. Roussière, L. Schulz, K.M. Schelkle, G. Wasserschaff, A. Milanov, E. Schwab, O. Deutschmann, A. Jentys, J. Lercher, S.A. Schunk, ChemCatChem, 6 (2014) 1447.
[16] K. Ikkour, D. Sellam, A. Kiennemann, S. Tezkratt, O. Cherifi, Catal. Lett., 132 (2009) 213.
[17] Y. Zhang, Q. Li, H. Li, Y. Cheng, J. Zhang, X. Cao, J. Cryst. Growth, 310 (2008) 3884.
[18] Z. Xu, M. Zhen, Y. Bi, K. Zhen, Catal. Lett., 64 (2000) 157.
[19] Z. Xu, M. Zhen, Y. Bi, K. Zhen, Appl. Catal., A, 198 (2000) 267.
[20] T.H. Gardner, D. Shekhawat, D.A. Berry, M.W. Smith, M. Salazar, E.L. Kugler, Appl. Catal., A, 323 (2007) 1.
[21] T.H. Gardner, J.J. Spivey, E.L. Kugler, A. Campos, J.C. Hissam, A.D. Roy, Journal of Physical Chemistry C, 114 (2010) 7888.
[22] Nagaoka Katsutoshi, Seshan Kulathuiyer, Lercher Johannes A., A. Ken-ichi, Catal. Lett., 70 (2000) 109.
[23] W. Shen, H. Momoi, K. Komatsubara, T. Saito, A. Yoshida, S. Naito, Catal. Today, 171 (2011) 150.
[24] A.K. Avetisov, J.R. Rostrup-Nielsen, V.L. Kuchaev, J.H. Bak Hansen, A.G. Zyskin, E.N. Shapatina, J. Mol. Catal. A: Chem., 315 (2010) 155.
[25] J. Zhang, H. Wang, A.K. Dalai, Appl. Catal., A, 339 (2008) 121.
[26] B. Quiroga, M. Martha, C. Luna, A. Eduardo, Ind. & Eng. Chem. Res., 46 (2007) 5265.
[27] Y. Cui, H. Zhang, H. Xu, W. Li, Appl. Catal., A, 318 (2007) 79.
[28] J. Wei, E. Iglesia, J. Catal., 224 (2004) 370.
[29] A. Yamaguchi, E. Iglesia, J. Catal., 274 (2010) 52.

[30] L.C.S. Kahle, T. Roussière, L. Maier, K. Herrera Delgado, G. Wasserschaff, S.A. Schunk, O. Deutschmann, Ind. & Eng. Chem. Res., 52 (2013) 11920.
[31] L. Maier, B. Schädel, K. Herrera Delgado, S. Tischer, O. Deutschmann, Top. Catal., 54 (2011) 845.
[32] S.Y. Foo, C.K. Cheng, T.-H. Nguyen, E.M. Kennedy, B.Z. Dlugogorski, A.A. Adesina, Catal. Commun., 26 (2012) 183.
[33] S. Gaur, D.J. Haynes, J.J. Spivey, Appl. Catal., A, 403 (2011) 142.
[34] M. Meyyappan, D. Lance, C. Alan, H. David, Plasma Sources Sci. Technol., 12 (2003) 205.
[35] F. Laville, M. Perrin, A.M. Lejus, M. Gasperin, R. Moncorge, D. Vivien, J. Solid State Chem., 65 (1986) 301.
[36] R. Bisson, M. Sacchi, T.T. Dang, B. Yoder, P. Maroni, R.D. Beck, J. Phys. Chem. A, 111 (2007) 12679.
[37] S. Nave, B. Jackson, J. Chem. Phys., 130 (2009) 054701 1.

3.8 License and contributions

This chapter has been previously published in **Applied Catalysis A: General** under the topic "*On the coke deposition in dry reforming of methane at elevates pressures*". Reuse of the publication in this thesis has been granted by Elsevier under licensing number **3667180789131** (December 2015).

Authors of the publication are:

Linus A. Schulz, Andreas Jentys, Johannes A. Lercher*
Department of Chemistry and Catalysis Research Center
Technische Universität München
Lichtenbergstraße 4, 85747 Garching, Germany

Lea. C.S. Kahle, Karla Herrera Delgado, Olaf Deutschmann
Institute for Chemical Technology and Polymer Chemistry
Karlsruhe Institute of Technology
Engesserstraße 20, 76131 Karlsruhe, Germany

Stephan A. Schunk
the GmbH, the high throughput experimentation company
Kurpfalzring 104, 69123 Heidelberg, Germany

Synthesis of the Ni catalysts, N_2-sorption, electron microscopy, kinetic experiments and temperature programmed oxidation were conducted by Technische Universität München. Dispersion measurements, reaction flow analysis and its comparison to experimental data were done by Karlsruhe Institute of Technology. hte GmbH provided important input on the catalytic materials and on the design of experiments. Interpretation of the experimental results and the found reaction scheme were achieved in close cooperation of all involved partners.

4 Methane dry reforming on a Ni hexa-aluminate at elevated pressures

Rate dependencies of reactants (CO_2, CH_4) and products (H_2, CO and H_2O) during methane dry reforming and a mechanistic framework that describes the observed dependencies are established for a Ni-catalyst under severe deactivating conditions of high pressure (1 MPa) and temperatures (1123 K). Two distinct kinetic regimes were detected, each with unique dependencies for methane activation and reverse-water-gas-shift reactions. For CH_4/CO_2 ratios above two, CH_4 conversion rates increase proportionally with CH_4 and CO_2 pressures. As the CH_4/CO_2 ratio decreases below two, the CH_4 conversion rates become independent of CO_2 pressure. In both kinetic regimes across all CH_4/CO_2 ratios, the products H_2, CO, and H_2O do not influence the CH_4 conversion rates. These observed dependencies are consistent with kinetically relevant surface reaction of carbon containing species with the oxidants. Across all operating CH_4-to-CO_2 ratios, the reverse-water-gas-shift reaction is not equilibrated. At very low CO_2 partial pressures, the RWGS reaction is even completely suppressed because the low accessible H_2 on the surface. The lack of CH_4 activation rate inhibition indicates that Ni sites were nearly free of surface species under these conditions that lead to carbon deposition, apparently because the carbonaceous species migrates rapidly from the active sites where it is formed to organized carbon fibers.

1.1 Introduction

Dry reforming of methane (DRM, (4-1)) is an attractive route for producing pure CO or synthesis gas mixture with a higher carbon content. The reaction utilizes CH_4 and CO_2, both are found in natural gas, thus making the direct synthesis gas production feasible at remote gas exploitation sites without gas separation. Research activities on dry reforming during the last decades involved synthesizing coke resistant catalysts, exploration of optimal process parameters, and investigating the reaction mechanism [1-13]. The key challenge for this reaction is the deposition of coke on catalyst surfaces, because under nearly all reaction conditions, carbon formation is thermodynamically favored, thus, coking dictates the stability of the catalysts.

Base metals (such as Ni and Co) are known to be more prone to coking than noble metals under DRM conditions, but they are attractive candidates because of their much lower costs and larger abundances than noble metals. Despite the improvement on synthesizing stable Ni-based catalysts [14-19], a self-containing kinetic model at elevated temperatures and pressures has not yet been developed for such catalysts. One reason is the complex reforming reaction network that consists of the dry reforming and several relevant side reactions as given below:

$CH_4 + CO_2$	$\rightleftharpoons$	$2\ H_2 + 2\ CO$	$\Delta H^0_{298K} = 247\ kJ/mol$	(4-1)
$CO_2 + H_2$	$\rightleftharpoons$	$H_2O + CO$	$\Delta H^0_{298K} = 41\ kJ/mol$	(4-2)
$H_2O + CH_4$	$\rightleftharpoons$	$3\ H_2 + CO$	$\Delta H^0_{298K} = 206\ kJ/mol$	(4-3)
$C^* + H_2O$	$\rightleftharpoons$	$CO + H_2$	$\Delta H^0_{298K} = 131\ kJ/mol$	(4-4)
CH_4	$\rightleftharpoons$	$C^* + 2\ H_2$	$\Delta H^0_{298K} = 75\ kJ/mol$	(4-5)
$2\ CO$	$\rightleftharpoons$	$CO_2 + C^*$	$\Delta H^0_{298K} = -171\ kJ/mol$	(4-6)

In addition to the CH_4 dry reforming reaction (Equation 1), H_2, the main product of DRM (4-1), may react with the excess CO_2 in the gas stream to produce H_2O and CO in the reverse water-gas-shift-reaction (RWGS, (4-2)). H_2O can subsequently react with CH_4 or its derivatives via steam reforming (SRM, (4-3)) to form H_2 and CO (4-4). Finally, methane cracking (4-5) and the Boudouard reaction (4-6) may also occur concomitantly [20]. All these reactions not only have the same reactants and products, but also share their surface intermediates and presumably even their active sites [21].

Pressurization is usually advantageous in technical applications, so pressure effects need to be considered for a description of the system near technically relevant conditions. Dry reforming – as the main reaction in the network – forms four molecules out of two reactants, thus the overall conversion depends strongly on the system pressure and at high pressures, the conversion may become thermodynamically limited. Additionally, carbon formation in many cases is enhanced under pressure. Dry reforming is strongly endothermic (247 kJ/mol), whereas carbon deposition reactions are exothermic. Such thermodynamics led to the need of operating at temperatures exceeding 1000 K in order to reach acceptable yields and minimum carbon formation. Consequently, reforming reactors are usually operated at conditions beyond 1 MPa and 1000 K. The majority of kinetic studies of DRM, however, avoid such reaction conditions [22, 23]. The lack of kinetic details under these severe conditions require conclusions to be extrapolated over a significant parameter space.

On group VIII metals, several groups identified the CH_4 partial pressure as the sole factor of kinetic relevance in H_2O and CO_2 reforming and deduced from this information a mechanism in which the C-H bond cleavage is the rate-determining step (RDS). Usually, this mechanism follows the Langmuir-Hinshelwood scheme with surface reactions among adsorbed species [24-26]. Iglesia et al. worked on the kinetic description of reforming under a wide range of conditions on several active metals and also identified the irreversibly breaking of the first C-H bond as the RDS [6, 27, 28]. Additionally, the kinetic relevance of H_2O and CO_2 activation was excluded, thus, assuming that all oxidant activation steps in the network are quasi-equilibrated. On Ni, the cross-exchange between CD_4 and CH_4 demonstrates the reversibility of the reaction sequence $CH_{3(ads)} \rightleftharpoons CH_{2(ads)} \rightleftharpoons CH_{(ads)}$ at ambient pressure [3]. Alternatively, it was postulated that DRM reactions are structure sensitive and the CH_4 conversion rates increase when the metal particle size and the related surface atom coordination decrease. By tailoring accessible sites by either varying by the variation of the metal loading [7] or by sulfur poisoning [29] and concluded that smaller particles favor the structure-insensitive reforming reaction over the structure-dependent carbon deposition. Separate studies reported that the identity of support plays a kinetically significant catalytic role in CH_4 conversion, in addition to metal particle size. CO_2 is able to form carbonates on oxides such as La_2O_3 [30], Al_2O_3, TiO_2 and ZrO_2 [9], which subsequently participate in the catalytic reactions and become a part of the reaction network. This complexity points to the challenges for insight based catalyst development.

For the present study, highly temperature stable Ni-hexaaluminate has been chosen as catalytic material. Hexaaluminates are layered crystal materials consisting of spinel- and mirror-planes. The mirror planes separate the spinel layers and contain large cations such as Ba^{2+}, Sr^{2+} or La^{3+}, which stabilize the structure. Depending on the identity of the stabilizing cation, the crystal structure of the materials has either magnetoplumbite (e.g., La^{3+} or Sr^{2+}) or β-alumina (e.g. Ba^{2+}) structure. These materials have been applied in a large variety of high temperature applications such as partial oxidation, catalytic combustion, and dry reforming [18, 31-35]. In this study, we will be using a La-stabilized hexaaluminate material with Ni as the active metal.

In chapter 1 of this thesis a dry reforming reaction scheme for Ni-hexaaluminates and compared this to the reaction pathways on a Pt/ZrO_2 catalyst is presented. We showed that the Ni containing catalyst is comparable to Pt in activity, but at the same time it builds up more coke than Pt. Evidence points to the higher coke deposition on Ni to be related to the low rates of surface carbon gasification on Ni [21].

The model, however, did not provide the detailed kinetic description for the dry reforming reactions at elevated pressures. Here, we report on the kinetics of methane dry reforming at temperatures and pressures close to the technical application (1123 K, 1 MPa). Under conditions favoring carbon deposition, kinetic measurements were conducted that show the influence of the CO_2 and CH_4 reactants as well as the impact of the product gases H_2, CO, and H_2O on both the rates of CH_4 conversion and RWGS reaction. Based on these observations, a reaction network and a kinetic model were derived that identify the RDS and describing the use of Ni-based catalysts. A special focus has been put on describing the RWGS reactivities and their influences on the product compositions.

1.2 Experimental

1.2.1 Catalyst synthesis

$Ni(NO_3)_2 \cdot 6\ H_2O$ (Sigma-Aldrich, puriss, ≥98.5%), $Al(NO_3)_3 \cdot 9\ H_2O$ (Sigma Aldrich, puriss, ≥98.5%) and $La(NO_3)_2 \cdot 6\ H_2O$ (Sigma-Aldrich, puriss, ≥99.0%) were dissolved in stoichiometric amounts in deionized water and the resulting solution was added drop-wise into a solution of polyethylene-glycol contained in isopropanol. The mixture was dried, mortared and calcined in air at 873 K for 2 hours and 1473 K for 8 hours [18, 21]. The nominal Ni loading was 5 wt.-% and the one of La is 22 wt.-%.

1.2.2 Sorption measurements

Specific surface area (by N_2 adsorption) and metal dispersion (by H_2 adsorption) were measured in a Sorptomatic 1990 system. The specific surface area was determined form the adsorption of N_2 conducted at 77 K and relative pressures (p/p^0) from 0.03-0.10 after outgassing the samples in high vacuum for 2 hours at 523 K.

To obtain the Ni dispersion the sample was pre-treated in a stream of H_2 at 1037 K for 12 h and then transferred to the automatized system where the sample was reduced again for 3 hours at 673 K and 101.3 kPa before the measurement was performed at a pressure lower than 0.1 Pa and 308 K. The pressure increments in the range of 0.57-1.02 kPa were equilibrated for 3-5 min and after finishing the first measurement the system was re-evacuated for 1 h to a pressure below 0.1 Pa H_2 in order to remove weakly bound H_2 from the support. Afterwards a second isotherm was measured and the amount of adsorbed H_2 was calculated by the difference between the first and the second isotherms at zero pressure, by extrapolation of the linear part of the respective isotherms to zero pressure. For dispersion calculation an atomic ratio of H to surface Ni of unity was assumed [36].

1.2.3 Transmission electron microscopy

For the transmission electron microscopy (TEM) measurements, the samples were dispersed in EtOH using an ultrasonic bath, one drop of the dispersion was applied to a copper grid supported film and dried for 24 hours before transferring it into a JEM-2010-JEOL. This microscope was equipped with a LaB_6 electron source (120 kV acceleration voltage) and had a resolution of 0.2 nm.

1.2.4 Scanning electron microscopy

Scanning electron microscopy (SEM) was conducted in a high resolution FE-SEM, JSM 7500 F (JEOL) with EDX (Oxford). Sample preparation was equal as described for the TEM measurements.

1.2.5 Kinetic investigations

Rate and selectivity measurements were carried out using a stainless steel plug flow reactor at 1 MPa. Individual inlet partial pressures of the reactant gases were varied from 40 kPa to 300 kPa and diluted by N_2 at a constant overall flow of 260 ml_n/min. Gas flows were controlled by Bronkhorst digital mass flow controllers. The temperature of the catalyst bed was 1123 K and all lines of the setup were kept above 443 K to prevent water condensation. For the measurements, 3 mg of the catalyst were physically mixed with 97 mg of SiC particles and the mixture was inserted into an AlO_x tubing of 6 mm inner and 7 mm outer diameter. The catalyst bed was kept in place by two layers of quartz wool and the AlO_x tube was introduced into the stainless steel reactor (inner diameter 8 mm). To prevent gas contact to the outer stainless steel reactor wall, the outside of the AlO_x tubing was sealed with high temperature resistant rubber bands at the inlet and the outlet of the reactor. Before reaction, the catalyst was activated at 1073 K in a stream of 20 vol.-% H_2 in N_2 for 2 hours. To ensure stable conditions, the catalysts were additionally pre-treated in a stream of 50/50/160 ml/min of CH_4/CO_2/ N_2 for 5 hours at 1123 K and 1 MPa before conducting the kinetic tests. The evolving gases were analyzed in a combined Shimadzu GC-2010/Shimadzu GC-2010 Plus system containing an HQ-Plot and a molsieve column and a TCD detector.

1.2.6 CH_4 activation

The CH_4 activation experiments were conducted in the same reactor system and under comparable conditions as the other kinetic measurements, but the GC/MS analysis system was replaced by an online Pfeiffer Omni Star TM GSD 320 OC mass spectrometer. Before testing, the samples were reduced in an atmosphere of 20% H_2 in N_2 at 1073 K for 2 hours. The experiments were conducted with and without pretreatment of the sample in 50/50/100 ml_n/min of CH_4/CO_2/ N_2 at 1123 K and 1 MPa for 5 hours. Before the start of the experiment, the reactor was flushed with N_2 at 1123 K and 1 MPa and then set to the bypass mode. Subsequently the flow was changed to 100/100 ml_n/min CH_4/N_2 and the gas flow was stabilized. The reaction was initiated by

switching the flow from the bypass to reactor and observing the breakthrough of the CH_4 at the reactor outlet. The CH_4 conversion was followed by H_2 detection (m/z = 2).

1.3 Results and discussion

1.3.1 Structural analysis

The hexaaluminate was a non-porous material with a BET surface area of 7.1 m²/g. Ni dispersion was 0.5%, which means that the concentration of accessible Ni atoms on the surface was $4.3 \cdot 10^{-6}$ mol/$g_{catalyst}$ (5 wt.-% Ni). The combination of the low outer surface area of the support, its lack of pores, and the high reduction temperature of 1073 K led to Ni particles [37] with an average particle size of 22 nm (TEM and H_2 chemisorption). Dispersion measurements showed that the metal particles after reduction had an average size and minimum visible particles of 16 nm (Figure 4-1).

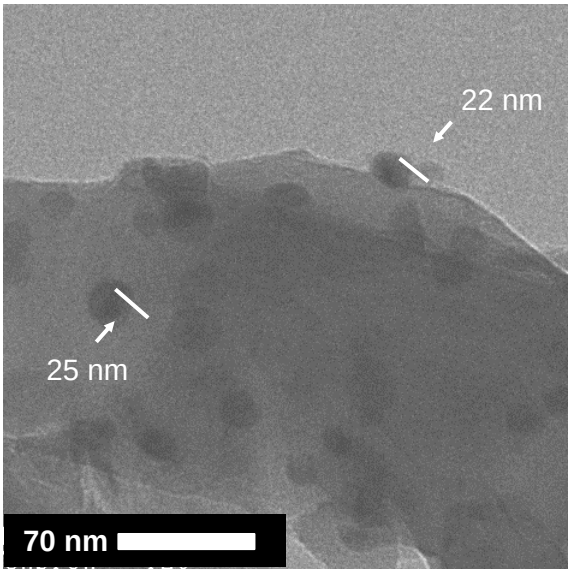

Figure 4-1 TEM image of a fresh Ni-hexaaluminate catalyst after treatment in 5 vol.-% H_2 in N_2 at 1073 K for 2 hours

1.3.2 Deactivation and carbon deposition

The long-term stability of the catalyst was tested by plug flow experiments in a constant gas flow of 45/45/10 ml_n/min of $CH_4/CO_2/N_2$ at 1123 K and 1 MPa. During the first 100 min of the reaction, moderate activation was observed, which led to increased conversion (Figure 4-2). After this initial phase, the catalyst converted both CH_4 and CO_2 at constant rates. The conversion of CO_2 (36 %) was substantially higher than that of CH_4 (24 %).

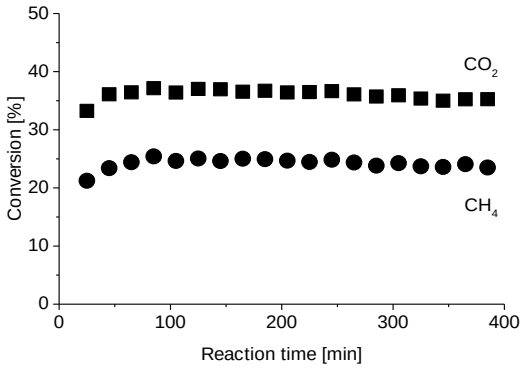

Figure 4-2. CO_2 and CH_4 conversion during CH_4-CO_2 (CH_4/CO_2 =1) reactions on a Ni/Hexaaluminate for 100 ml/min gas feed (1.54 x 10^6 cm^3 g_{cat}^{-1} $h^{-}1$) at 1123 K and 1 MPa system pressure.

TEM and SEM were taken after reactions and both prove clearly that the main form of carbon built up during reaction were carbon nano-tubes (Figure 4-3 and Figure 4-4). The TEM reveals that the Ni particles sinter further during reaction as the average particle size increases to more than 30 nm (from an initial average size of 22 nm). Furthermore, it is obvious that the nanofibers in the direct vicinity of the catalyst particle are hollow with an inner diameter similar to the size of the Ni particles. There is even one particle visible on the TEM micrograph that appears to be encapsulated within the carbon fiber (marked with a black arrow in Figure 4-3). As also can be observed from the figure, by far not all Ni particles on the catalyst surface are covered in carbon or CNTs, indicating that possibly also only part of the Ni participates in the carbon deposition.

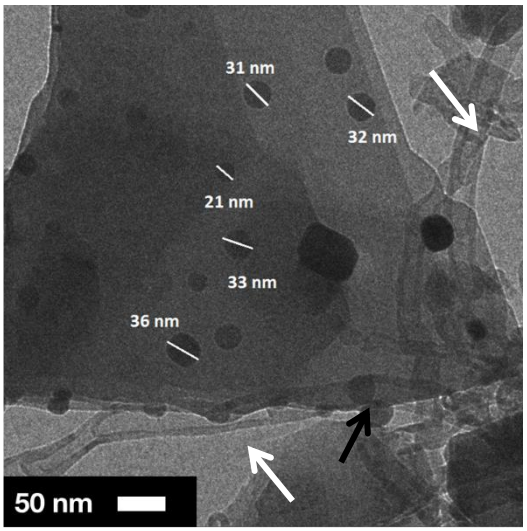

Figure 4-3 TEM picture of the spent catalyst after reaction under dry reforming conditions for 500 min (CH_4-CO_2 = 1, 1123 K, 1 MPa system pressure and 1.54 x 10^6 cm^3 $g_{cat}^{-1}h^{-1}$). The Ni particle size increased from 22 nm to more than 30 nm in average. Formation of carbon nanotubes in direct proximity to the particle is also visible (white arrows). One Ni particle is apparently encapsulated within such a carbon nano fiber (black arrow).

The same phenomenon was captured in the SEM micrograph in Figure 4-4. While the surfaces of the catalyst were largely free of carbon deposits after exposure to DRM for 500 min, severe carbon nanotube formation was observed. These carbon nanotubes have a diameter between 35 to 50 nm, as also found in the TEM micrograph in Figure 4-3 (marked with black arrows). In the contrary, the catalyst structure well preserved, and even the crystal facets are visible (white arrow). This hints to the fact that the predominant form of carbon deposition is the fixation into carbon-nano-tubes, while other carbon species such as graphite are insignificant.

The continuing coke formation and the absence of adverse effects of carbon deposition on CH_4 or CO_2 conversion rates during dry reforming have been previously reported also for Ni/Al_2O_3, and Ni/ZrO_2 catalysts as well as $Pt/\gamma\text{-}Al_2O_3$ catalysts under DRM up to 1273 K [38-40]. This is attributed to the involvement of different carbon species in the DRM and carbon formation routes. A portion of the carbonaceous intermediates is active in DRM, but the rest remains less active and forms persistent deposits [41].

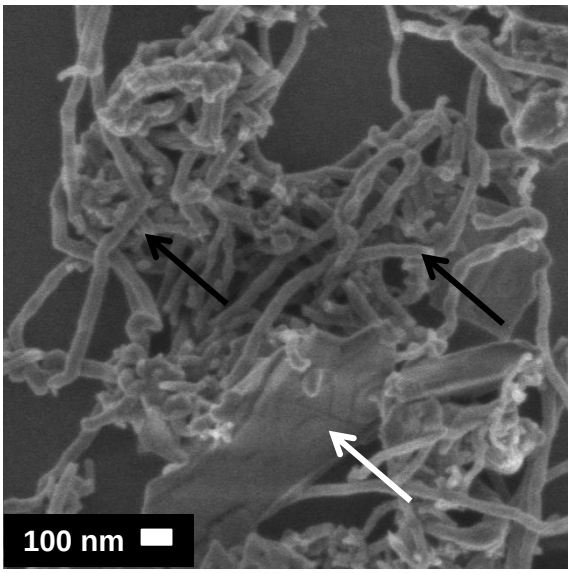

Figure 4-4. SEM picture of the carbon covered Ni-hexaaluminate catalyst after exposure to CH_4-CO_2 reactions at 1123 K and 1 MPa system pressure and 1.54 x 106 cm^3 $gcat^{-1}$ h^{-1} for 500 min. The white arrow marks the support´s crystallite facets that remain visible after reaction. The outer diameter of the carbon-nano tubes is between 40 and 50 nm (black arrows).

1.3.3 Activation of methane

Before discussing the DRM kinetics, we will compare the transient rate of methane decomposition between a fresh and a spent catalyst; the latter was exposed to the DRM conditions in a 1:1 CH_4-CO_2 mixture at 1123 K and 1 MPa system pressure and 1.54 x 10^6 cm^3 g_{cat}^{-1} h^{-1} for 500 min. This pretreatment of the catalyst under DRM conditions did not lower the rate of methane decomposition (Figure 4-5). The peak of H_2 (generated by decomposition of CH_4) was even slightly higher for the sample pretreated with DRM conditions than the fresh sample. The slightly higher activity on the pretreated sample agreed well with the modest increase in CH_4 and CO_2 conversion rate during the early time-on-streams (Figure 4-2). Note that the breakthrough of the gases was slightly faster over the pretreated sample, an indication that the overall reactor volume might be decreased after the pretreatment procedure. This volume reduction might be attributed to the carbon fiber formation as observed by SEM (Figure 4-4). The H_2 concentration decreased quickly after reaching a maximum, indicating deactivation. This is attributed to the fact that an increasing fraction of sites active for methane dissociation was covered with time on stream until the conversion stopped completely. This suggests that all active sites were covered after a short time on stream (encapsulation) and that CO_2 is required to remove the surface carbon. However, these conditions are different from other experiments, in which the Ni centers remain active after C-H bond cleavage. This might be attributed to the lack of oxygen in the reactor in this reaction system [21, 42, 43].

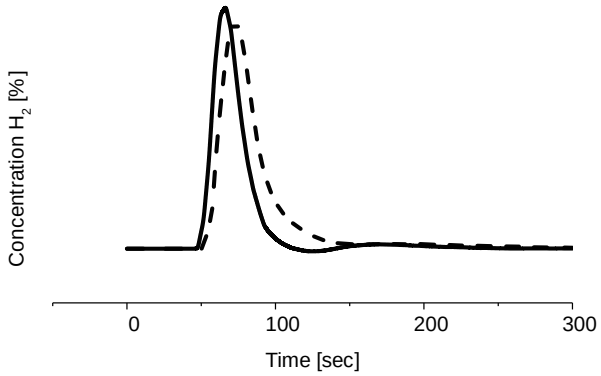

Figure 4-5. Breakthrough curves of H_2 set free from CH_4 decomposition on the surfaces of Ni-hexaaluminate without (dashed) and with (solid) pretreatment of the sample in CH_4-CO_2 mixtures at 1123 K and 1 MPa system pressure and 1.54 x 10^6 cm^3 g_{cat}^{-1} h^{-1} for 500 min.

1.3.4 Reactor heat loads and thermodynamic considerations

CH_4-CO_2 reactions on dispersed metal clusters occur via concomitant dry reforming, reverse water-gas-shift, and steam reforming reactions [Reactions (4-1)-(4-3)]. The reforming reactions [Reactions (4-1) and (4-3)] are highly endothermic. The strong endothermicity of the reforming reactions may cause local temperature and/or concentration gradients within the pellets and the catalyst bed; it also places thermodynamic constraints on the methane conversion rates, especially at low temperatures, which may influence the measurements of the forward methane conversion rates.

The highest rate of heat formation is estimated to be 1.6 $J*sec^{-1}$, based on reforming reactions in the reactor configurations in this study. This reactor heat load and a small reactor bed volume of 0.03 cm^3 together with a strong dilution of the catalyst within inert SiC is sufficient to ensure uniform temperature and concentration across the catalyst particles without any heat and mass diffusion limitation.

Under all conditions reported here, the steady-state CO_2 conversion was higher than that of CH_4 conversion and the H_2/CO ratio was always lower than unity. Additionally, H_2O was detected in the product gas stream. These effects are caused by the RWGS reaction (Equation (2)) that occurs in parallel to the DRM (Equation (1)). It influences the CO_2 conversion rate but does not affect the CH_4 conversion rate [44, 45]. Therefore, the DRM rate was determined only from the conversion of CH_4 but not from CO_2 conversion.

The dry reforming reaction is part of a reaction network in which the forward and backward reactions may be close to the thermodynamic limits. Thus, the experimentally

measured CH_4 conversion rate, $r_{net(CH_4)}$, equals the difference of the forward and backward rates of all reactions containing CH_4. To calculate the forward reforming rate, the approach to equilibrium (ATE) concept has been applied [6].

The extents of equilibria for the mentioned reactions are defined by their respective reaction quotients Q_i (where subscript *i*=SRM, DRM and RWGS denote steam reforming, dry reforming, and reverse water-gas-shift, respectively) given by the following expressions:

$$Q_{SRM}=\frac{[H_2]_{av}^3[CO]_{av}}{[CH_4]_{av}[H_2O]_{av}} \quad (4\text{-}7)$$

$$Q_{DRM}=\frac{[H_2]_{av}^2[CO]_{av}^2}{[CO_2]_{av}[CH_4]_{av}} \quad (4\text{-}8)$$

$$Q_{RWGS}=\frac{[H_2O]_{av}[CO]_{av}}{[CO_2]_{av}[H_2]_{av}} \quad (4\text{-}9)$$

where $[CO]_{out}$, $[H_2]_{out}$, $[H_2O]_{out}$, $[CO_2]_{out}$, and $[CH_4]_{out}$ are the outlet pressures and $[CO]_{av}$, $[H_2]_{av}$, $[H_2O]_{av}$, $[CO_2]_{av}$ and $[CH_4]_{av}$ are the average pressures of the components along the reactor. The equations (4-7)-(4-9) describe the approach-to-equilibrium values (η_i) for these reactions i (i=SRM, DRM, RWGS):

$$\eta_{SRM}=\frac{Q_{SRM}}{K_{SRM}}=\frac{[H_2]_{out}^3[CO]_{out}}{[CO_2]_{out}[H_2O]_{out}}\frac{1}{K_{SRM}} \quad (4\text{-}10)$$

$$\eta_{DRM}=\frac{Q_{DRM}}{K_{DRM}}=\frac{[H_2]_{out}^2[CO]_{out}^2}{[CO_2]_{out}[CH_4]_{out}}\frac{1}{K_{DRM}} \quad (4\text{-}11)$$

$$\eta_{RWGS}=\frac{Q_{RWGS}}{K_{RWGS}}=\frac{[H_2O]_{out}[CO]_{out}}{[CO_2]_{out}[H_2]_{out}}\frac{1}{K_{RWGS}} \quad (4\text{-}12)$$

In accordance to the calculations for reforming, the forward rate for dry reforming and the reverse water-gas-shift reaction is:

$$r_{DRM,f}=\frac{r_{net,\,CH4}}{1\text{-}\eta_{DRM}} \quad (4\text{-}13)$$

$$r_{RWGS}=\frac{r_{CO_2,net}-r_{DRM,f}}{1-\eta_{RWGS}}. \quad (4\text{-}14)$$

Rate and selectivity data reported here were measured over the pressure range of 20–190 kPa CH_4 and 30–200 kPa CO_2 at 1123 K and a constant space velocity of

5.2×10^6 ml·g^{-1}·h^{-1}. Under these reaction conditions, the approach-to-equilibrium values for CO_2 and H_2O reforming (η_{DRM} and η_{SRM}, respectively) are smaller than 0.003 for DRM and 0.02 for the concurrent SRM; the values for RWGS (η_{RWGS}) are between 0.02 and 0.6. These latter values indicate that the RWGS reaction has not attained chemical equilibrium, in contrast to earlier reports [3, 22, 44, 46, 47]. These differences are attributed to two effects: (1) the temperatures reported in the literature were frequently lower than in this study. Bermúdez et al. showed that the RWGS is promoted over the DRM at lower temperatures [48] and Wang et al. proposed the RWGS and DRM rates to converge above 1237 K, [49]. This means that under the reaction conditions of this study DRM and RWGS were approximately in the same range, in contrast to other studies. (2) The space velocity used in this work is much higher than those reported in the literature are. Our measurements were carried out at space velocities that were approximately one order of magnitude higher than most studies that led to RWGS equilibrium [44, 47] (Table 4-1). The highest space velocities reported in the literature were only half as high as the values used in this study ($5.2\cdot10^6$ ml·g^{-1}·h^{-1}) [3, 46]. The non-equilibrated RWGS led us to include the elementary steps related to RWGS in the kinetic evaluation of the DRM reaction. We note that ATE of RWGS under specific conditions increases to 0.6, even at such high space velocities used in our study. Such increases in ATE indicate the high rates of the water-gas-shift reaction.

Table 4-1 Comparison of the space velocities used in our CH_4-CO_2 studies to those applied in the literature and their effects on the ATE of RWGS

Source	Temperature [K]	Pressure [kPa]	CH_4/CO_2 ratio	Space velocity [ml g^{-1} h^{-1}]	RWGS equilibrated
Our data	1123	1000	0.2 – 5	$5.2\cdot10^6$	No
[3]	823, 873	100 – 1500	0.2-1.5	$2\cdot10^5$ – $1{,}8\cdot10^6$	Yes
[44]	673 – 873	100	1	10^4 – $2\cdot10^5$	Yes
[46]	773	100	1.1-1.2	$1.5\cdot10^5$-10^6	Yes
[47]	723 – 1173	100	1	$6\cdot10^4$	Yes
[48]	1073, 1173, 1273	100	1	$7.5\cdot10^2$ – $9.3\ 10^3$	No

1.3.5 Forward Rates of Methane Dry Reforming and Reverse-Water-Gas-Shift Reactions

In this section, we discuss the kinetic dependencies for methane dry reforming and reverse-water-gas-shift reactions. Figure 4-6 shows the forward DRM turnover frequencies (TOF) and Figure 4-7 shows the forward TOFs for the reverse-water-gas-shift reaction (Figure 4-7a) and its approach-to-equilibrium values (Figure 4-7b), η_{RWGS}, measured on the $Ni_{0.7}La_{1.3}Al_{11}O_{19}$ catalyst at 1123 K, 190 kPa CH_4, and varying CO_2 pressures (20–190 kPa). These reactant pressures correspond to mean operating

CH_4/CO_2 ratios of 0.9 to 6.2 (as also indicated in Figure 4-6). The two distinct kinetic dependencies are evident: (1) regime 1 for CO_2 pressure below 100 kPa and the related operating CH_4/CO_2 ratios above 2 and (2) regime 2 for CO_2 pressure above 100 kPa and the related operating CH_4/CO_2 ratios below 2. In regime 1 at low CO_2 pressures (<100 kPa; CH_4/CO_2 ratio > 2), forward methane TOFs increased proportionally with CO_2 pressure. As the CO_2 pressure increased to above 100 kPa and the related CH_4/CO_2 ratio decreased below 2 in regime 2, the rates became insensitive to CO_2.

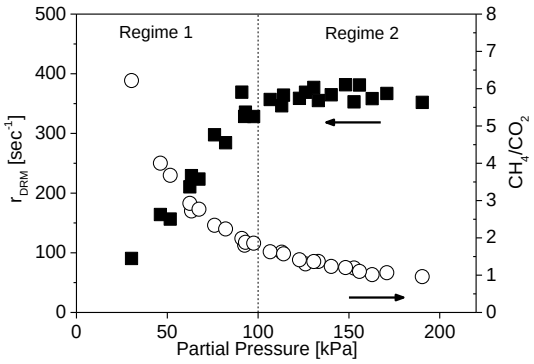

Figure 4-6. Influence of CO_2 partial pressure on the forward rate of methane dry reforming $r_{(DRM)}$ (■) and on operating CH_4/CO_2 ratios (○) on Ni-hexaaluminate catalyst (190 kPa of CH_4, 30-190 kPa CO_2, 1123K, 1MPa, balance N_2, Space velocity 4×10^6 cm^3 g_{cat}^{-1} h^{-1}, 3 mg catalyst physically mixed with 97mg SiC).

The transition of kinetic dependence from one regime to another is also evident in the reverse-water-gas-shift reaction. In regime 1, the rates of RWGS reaction remained essentially undetectable within the experimentally measurable limits, but as the operating CO_2 pressure and CH_4/CO_2 ratio reached the transition point (at $CH_4/CO_2 = 2$) to regime 2, the rates increased linearly with CO_2 pressure. This transition in rates, which depends on the operating CH_4/CO_2 ratios, suggests that CH_4/CO_2 ratios and the related carbon chemical potentials dictate the amount of the carbonaceous species on the Ni cluster surfaces. The transition reflects a shift in the coverages of Ni crystallite surfaces from largely covered with methane derived species (CH_x*) to uncovered, as the CH_x* removal rates via their oxidation by reactive oxygen species (O*) concomitantly increase.

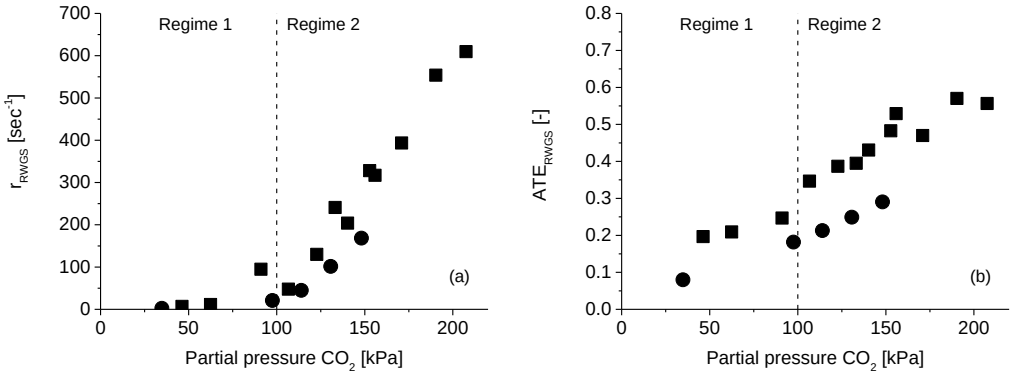

Figure 4-7 Effect of partial pressure of CO_2 on the (a) RWGS forward rate (r_{RWGS}) and the (b) RWGS approach-to-equilibrium values (ATE_{RWGS}) during methane reforming on $Ni_{0.7}La_{1.3}Al_{11}O_{19}$ catalyst (190 kPa (■) and 200 kPa (●) of CH_4, 30-200 kPa CO_2, 1123K, 1MPa, balance N_2, space velocity 4×10^6 $cm^3\,g_{cat}^{-1}\,h^{-1}$, 3 mg catalyst physically mixed with in 97mg SiC)

Over the pressure range of 25 kPa to 170 kPa CH_4, the forward turnover rates for DRM increase nearly proportionally with CH_4 pressure, i.e., from 77 sec^{-1} at 35 kPa to 400 sec^{-1} at 170 kPa of CH_4 (T = 1123 K). This change in CH_4 pressure does not influence the rates of RWGS reaction (Figure 4-9a), as CH_4 is neither a reactant nor a product for the RWGS reaction. The same holds true for the ATE of the RWGS (Figure 4-9b), which stays unaltered irrespective of the CH_4 pressure over the whole CH_4 pressure range from 35 kPa to 170 kPa.

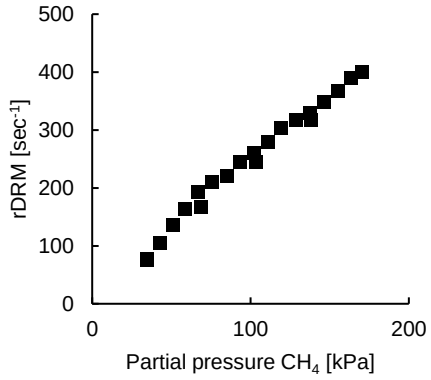

Figure 4-8 Forward rate of methane (r_{DRM}) during carbon dioxide reforming of methane (DRM) as a function of CH_4 pressure on $Ni_{0.7}La_{1.3}Al_{11}O_{19}$ catalyst (1 MPa; 35-170 kPa CH_4, 190 kPa CO_2, balance N_2; 1123 K, space velocity 4×10^6 $cm^3\,g_{cat}^{-1}\,h^{-1}$; 3 mg of catalyst physically mixed with 97 mg of SiC).

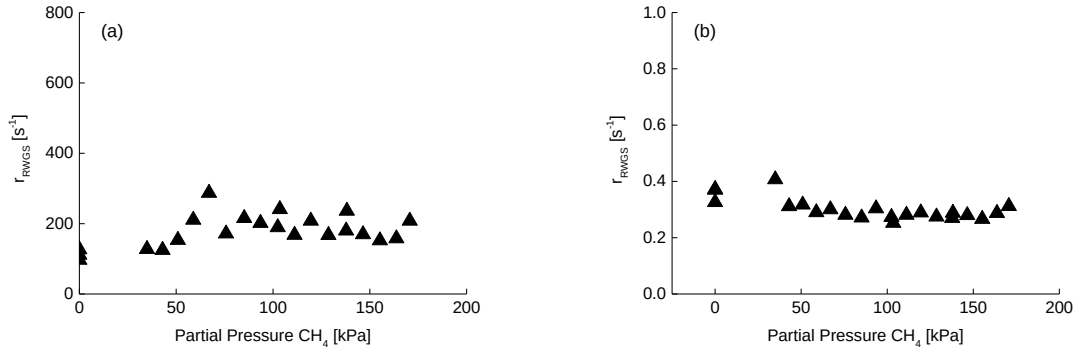

Figure 4-9 Effects of CH_4 pressure on (a) $r_{(RWGS)}$ and (b) $ATE_{(RWGS)}$ during carbon dioxide reforming of methane (DRM) on $Ni_{0.7}La_{1.3}Al_{11}O_{19}$ catalyst (1 MPa; 0-170 kPa CH_4, 190 kPa CO_2, balance N_2; 1123 K, space velocity 4×10^6 $cm^3\,g_{cat}^{-1}\,h^{-1}$; 3 mg of catalyst physically mixed with 97 mg of SiC).

The effects of H_2, CO, and H_2O on the forward DRM turnover rates are shown in Figure 4-10a, Figure 4-10b and Figure 4-10c, respectively. H_2 and CO pressures did not influence the DRM forward rates. In contrast, H_2O increased the overall CH_4 conversion rate, i.e., an increase in the H_2O pressure from 2 to 35 kPa led the rates to increase commensurately from 370 sec^{-1} to 450 sec^{-1}. But for the measurements one must be aware that (due to experimental constrains, the concentration of H_2O in the gas feed was more than double of the partial pressure that can thermodynamically be achieved in the pure dry reforming under the given conditions (without water-feed). Any increase in H_2O pressure above 50 kPa did not lead to further increase in CH_4 conversion rates. The CO_2 conversion decreased significantly with the addition of water and the conversion of CH_4 was, therefore, higher than the one for CO_2 (Figure 4-10c). This contrasts with what was observed for pure dry reforming and can be attributed to a reduced RWGS rate at these increased H_2O pressures as the H_2O formation via OH* from O* and H*, one of the key steps in the RWGS reaction, will be hindered at elevated partial pressures of H_2O. Therefore, it is hypothesized that the increase in CH_4 conversion rate, accompanied by a significant drop in CO_2 conversion, does not originate from dry but from additional steam reforming.

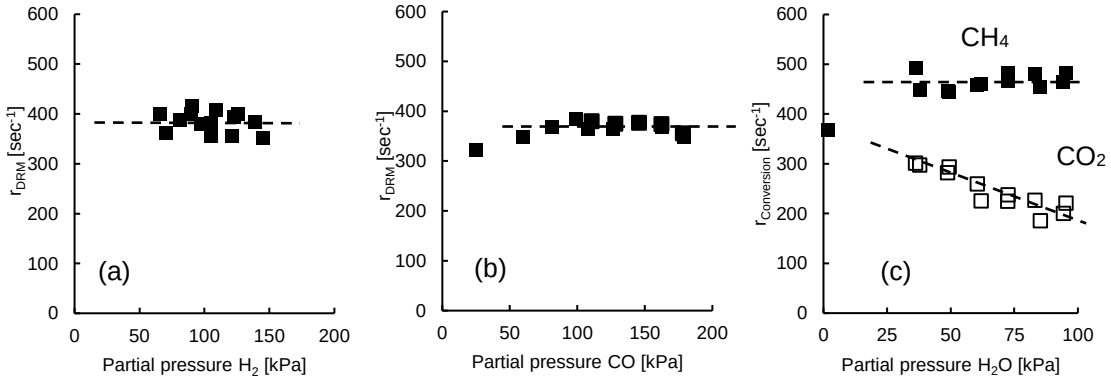

Figure 4-10. Effect of partial pressure of H_2 (a) and CO (b) on the forward rate of methane (r_{DRM}) and of H_2O (c) on the CH_4 and CO_2 conversion rates during carbon dioxide reforming of methane (DRM) on $Ni_{0.7}La_{1.3}Al_{11}O_{19}$ catalyst (1 MPa; 190 kPa CH_4, 190 kPa CO_2, balance N_2; 1123 K, space velocity 4×10^6 cm^3 g$_{cat}^{-1}$ h^{-1}; 3 mg of catalyst physically mixed with 97 mg SiC diluents; (a) 30-150 kPa H_2, (b) 25-180 kPa CO, (c) 35-100 kPa H_2O).

In regime 1 (CH_4/CO_2> 2), the forward CH_4 turnover rates ($r_{DRM,1}$, subscript DRM,1 denotes dry reforming in regime 1) increase with increasing CO_2 pressure:

$$r_{DRM,1} = k_{1,eff} \cdot p(CH_4)^0 \cdot p(CO_2)^1 \cdot p(CO)^0 \cdot p(H_2)^0 \cdot p(H_2O)^0 \quad (4\text{-}15)$$

$$r_{RWGS,1} \sim 0 \quad (4\text{-}16)$$

where $k_{1,eff}$ are the effective rate constant for the dry reforming reaction and p(X) are the partial pressures of species *X* (X=CH_4, CO_2, CO, H_2, or H_2O). The forward rates for reverse-water-gas-shift reaction were nearly zero (<10 sec^{-1}) (Figure 4-7). Lower rates for RWGS relative to those for reforming reactions are hypothesized to reflect the occupation of Ni surface sites by carbonaceous species (CH_x*). These Ni sites were unable to participate in the RWGS reactions. Although these sites are considered inactive for RWGS reactions, they are active towards the C-H bond activation and able to turnover CH_4. Zhang et al. proposed three different kinds of carbon on the surface of Ni catalysts and labeled them as C_α, C_β and C_γ [41]. These distinct types of carbon species were differentiated by the temperatures required for their oxidation during the temperature programmed oxidation (TPO), i.e., around 373 K for C_α, around 700 K for C_β, and above 700 K for C_γ. In an earlier work we have shown that the TPO peaks for C_β result from oligomeric/polymeric carbon and the peaks at higher oxidation temperatures originate from carbon-nano-tubes [21]. Both C_β and C_γ species, when formed on the Ni surfaces, led to a decrease in the reforming rate. In contrast, C_α was found to promote

reforming [41], because of the very low temperatures required for combusting the C_α carbon species during the TPO experiments and therefore their higher reactivities towards oxidation and removal as CO_x during reforming reactions., we hypothesize that they are surface CH_x groups that actively participate in the reforming reaction.

As the CH_4/CO_2 ratio decreased to below 2 (Regime 2), methane turnover rates became insensitive to CO_2 pressure (100-200 kPa, Figure 4-6) and increased proportionally with CH_4 pressure (Figure 4-8). In contrast to Regime 1, the forward rates of RWGS increased from nearly zero (at 100 kPa CO_2 pressure) to values higher than the dry reforming reaction (e.g., 675 s^{-1} RWGS vs. 380 sec^{-1} DRM at 200 kPa CO_2). These rate dependencies are captured with the following equations:

$$r_{DRM,2} = k_{2,eff} \cdot p(CH_4)^1 \cdot p(CO_2)^0 \cdot p(CO)^0 \cdot p(H_2)^0 \cdot p(H_2O)^0 \quad (4\text{-}17)$$

$$r_{RWGS,2} = k_{3,eff} \cdot p(CH_4)^0 \cdot p(CO_2)^1 \cdot p(CO)^0 \cdot p(H_2)^0 \cdot p(H_2O)^0 \quad (4\text{-}18)$$

where $k_{2,eff}$ and $k_{3,eff}$ are the effective rate constants for DRM and RWGS, respectively, and p(X) are the partial pressures of species *X* (X=CH4, CO_2, CO, H_2, or H_2O). The increase in the rate ratio of reverse-water-gas-shift reactions to dry reforming, $r_{DRM,2}/r_{RWGS,2}$, and the concomitant transition in the kinetic dependencies reflect a dynamic transition of the most abundant surface intermediates on Ni crystallite surfaces, i.e., from nearly saturated with CH_x* (regime 1) to unoccupied Ni sites (regime 2), as the CH_4/CO_2 ratio decreases. Figure 4-11 clearly shows the direct relation between the forward rates of CO_2 and CH_4 conversion and the point of transition between the regimes (100 kPa CO_2). At high CH_4/CO_2 ratios, the rates of CO_2 conversion equal those of CH_4 conversion, because dry reforming is the sole reactions and it occurs on Ni cluster surfaces fully occupied with the carbonaceous intermediates. On such surfaces, the rates of RWGS are insignificant. As the CO_2 pressure increases, above 100 kPa and the CH_4/CO_2 concomitantly decreases below 2, Ni sites become available on the surfaces and these sites participate in activating the CO_2 via RWGS reactions. As a result, the CO_2 conversion rates increase to values larger than those of CH_4 conversion, as shown in Figure 4-11. This difference between the CO_2 and the CH_4 conversion rates reflects the extent of RWGS reactions. The difference between the extents of DRM and RWGS becomes larger at the higher CO_2 pressures, predominantly because the rates of methane reactions do not vary with CO_2 pressures, but those of RWGS increase and eventually reach chemical equilibrium. Figure 4-7 demonstrates the CO_2 effects on these

rates and their extents to chemical equilibrium. Our measurements show the increase in the approach-to-equilibrium values for RWGS increase from 0 to 0.6. RWGS equilibrium was, however, not attained in our study, because of the high space velocity (Table 4-1), but was demonstrated by others at the much lower space velocities.

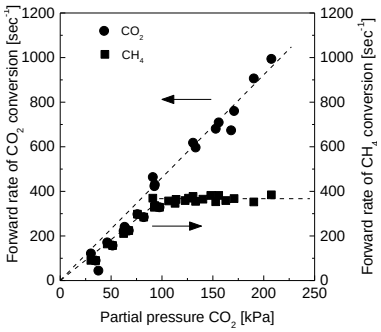

Figure 4-11 Effect of partial pressure of CO_2 conversion rates of methane (■) and CO_2 (●) on $Ni_{0.7}La_{1.3}Al_{11}O_{19}$ catalyst (1 MPa; 190 kPa CH_4, 30-190 kPa CO_2, balance N_2; 1123 K, space velocity 4×10^6 cm^3 g_{cat}^{-1} h^{-1}; 3 mg of catalyst physically mixed with 97 mg SiC diluents.)

1.3.6 Reaction mechanism and derivation of rate equation

In this section, we propose a sequence of elementary steps for DRM and RWGS (Scheme 1) that are consistent with the observed rate dependencies (Figure 4-6 to Figure 4-10) and the kinetic coupling of the DRM and RWGS reactions (Figure 4-11).

Scheme 1 Summary of the reaction steps in the kinetic model.

$CH_4 + 2*$	→	$CH_3* + H*$	Step 1
$CH_3* + *$	→	$CH_2* + H*$	Step 2
$CH_2* + *$	→	$CH* + H*$	Step 3
$CH*_a + *$	→	$C*_a + H*$	Step 4a
$C*_a + O*_a$	→	$CO* + *$	Step 5a
$CH*_b + O*_b$	→	$CHO*_b + *$	Step 4b
$COH*_b + *$	→	$CO* + H*$	Step 5b
$CO_2 + 2*$	→	$CO* + O*$	Step 6
$H* + O*$	→	$OH* + *$	Step 7
$OH* + H*$	⇌	$H_2O* + *$	Step 8
$H* + H*$	⇌	$H_2 + 2*$	Step 9
$CO*$	⇌	$CO + *$	Step 10

CH_4 dissociates irreversibly on a pair of Ni sites (*, Step 1) and forms adsorbed methyl (CH_3*) and hydrogen adatom (H*), as shown from our previous CH_4-CD_4 isotopic exchange experiments [21] and in agreement with refs. [3, 50, 51]. The CH_3* sequentially breaks its C-H bonds (Steps 2 and 3) and forms CH* intermediates. The $CH*_a$ species may undergo C-H bond cleavage, which leads to surface C* and H*. CO_2 adsorbs dissociative on Ni sites, forming chemisorbed CO* and reactive O* species (Step 6). The reactive $O*_a$ species oxidize the surface $C*_a$, forming CO*, which then desorbs as CO (Steps 4a, 5a and 10). $CH*_b$ may accept an $O*_b$ via an insertion step and form $COH*_b$ (Step 4b), which upon decomposition leads to CO* and H* (Step 5b). Based on density functional theoretical (DFT) calculations, CH* dissociation and the subsequent C* oxidation with O* is the preferred route on the Ni catalysts under the given conditions (i.e. 1123 K, 1 MPa) [21]. We do not, however, exclude the possibility of the other route to be kinetically relevant and, therefore, investigate both. The surface H*, generated from each C-H bond dissociation (Steps 1-3 and 4a), may recombine with O* to form a surface hydroxyl (OH*), which further reacts with a second H* to desorb as H_2O (Step 7 and 8). Two H* adatoms may combine and desorb as H_2 (Step 9). For the model, Steps 1 to 7, including 4a, 5a, 4b, and 5b are likely irreversible and Steps 8, 9, 10 are quasi-equilibrated. This catalytic sequence captures the formation of CO and H_2 (from dry reforming), H_2O (via reverse water-gas-shift reaction), and the subsequent steam reforming. One should note that as H_2O pressure increases, the reversibility of individual reaction steps (especially Step 7) might be altered. Our intention, however, was to describe the pure dry reforming reaction kinetics in which water was only generated via the RWGS.

We apply the pseudo-steady-state approximation on the closed catalytic sequence in Scheme 1 and derive from it the rate expressions for the forward methane conversion (via the DRM), forward reverse water-gas-shirt reaction, and overall CO_2 conversion. There are several scenarios imaginable:

(i) Methane turnover rates are limited by the activation of the CH_4 on the empty metal site-pairs (Step 1), thus, CH_4 conversion rates could be described as:

$$r_{DRM,1+2} = k_1 p(CH_4)[*]^2 \quad (4\text{-}19)$$

(ii) The reaction of surface-bound O* with either (a) C^*_a (Step 5a) or (b) CH^*_b (Step 4b) as the kinetically relevant step in the network. Simultaneously, the formation of water must be the key step in the RWGS reaction; so, Step 7 is the RDS for this reaction. This would render the turnover rate equations to be:

$$r_{DRM,a} = k_{5a}[C^*_a][O^*_a] \quad (4\text{-}20)\ (\text{Case a})$$

$$r_{DRM,b} = k_{4b}[CH^*_b][O^*_b] \quad (4\text{-}21)\ (\text{Case b})$$

$$r_{RWGS} = k_7[H^*][O^*] \quad (4\text{-}22)$$

$r_{DRM,1+2}$, $r_{DRM,a}$and $r_{DRM,b}$ are the forward turnover rate of CH_4 in the three different scenarios; k_1 is the rate constant of CH_4 activation on Ni sites; $p(CH_4)$ is the partial pressure of CH_4; $[*]$ is the fraction of empty sites; $[C^*_a]$, $[O^*_a]$, $[O^*_b]$, $[CH^*_b]$, $[H^*]$ and $[O^*]$ are the surface coverages of the respective species; k_{5a} is the rate constant for C^*_a reactions with O^*_a in case a; k_{4b} is the rate constant for CH^*_b reactions with O^*_b to form COH^*_b in case b; k_7 is the rate constant for the combination of H* and O* into OH* groups. These rate constants have also been defined in Scheme 1. The rates depend on the coverages and the identity of the reactive intermediates; thus, it is required to derive the rate dependence capturing the effects of their coverages. The surface coverages of the species and the number of empty sites are not accessible directly and therefore need to be described as functions of the partial pressures of the gasses. The sum of all coverages is defined as [T].

In the case of CH* dissociation and subsequent C* activation with O* (case **(a)**), $[T]_a$ is given by:

$$[\mathrm{T}]_a = 1 = [*] + [\mathrm{C^*_a}] + [\mathrm{CH_{x,a}{}^*}] + [\mathrm{CO^*}] + [\mathrm{H^*}] + [\mathrm{OH^*}] + [\mathrm{O^*_a}] \quad (4\text{-}23)$$

In the case **(b)** the surface species COH* needs to be considered, turning $[T]_b$ into

$$[\mathrm{T}]_b = [*] + [\mathrm{CH_{x,b}{}^*}] + [\mathrm{CH^*_b}] + [\mathrm{CO^*}] + [\mathrm{H^*}] + [\mathrm{OH^*}] + [\mathrm{O^*_b}] + [\mathrm{COH^*_b}] \quad (4\text{-}24)$$

In both equations, $[*]$ denotes free sites and [CO*], [OH*] and $[COH^*_b]$ are the surface coverages of the respective species. $[CH_{x,a}*]$ is the sum of the surface coverages of CH_3*, CH_2*, and CH* in case **(a)** and $[CH_{x,b}*]$ is the sum of the surface coverages of CH_3* and CH_2* in case **(b)**. As we do not distinguish at the start, which is the rate-determining step, we will establish all rate equations for the various scenarios and discuss later their fits with the experimental data.

The surface coverages of the species are not directly measurable and, therefore, the equations will be derived such that these surface coverages are expressed in terms of the partial pressures of the gases. The coverages for [H*], [CO*] and [OH*] are assumed to be equilibrated with respect to adsorption-desorption (and dissociation) in Steps 8, 9 and 10 of Scheme 1 per:

$$[\mathrm{H^*}] = \sqrt{\frac{\mathrm{p(H_2)}}{\mathrm{K_9}}}[*] \quad (4\text{-}25)$$

$$[\mathrm{CO^*}] = \frac{\mathrm{p(CO)}}{\mathrm{K_{10}}}[*] \quad (4\text{-}26)$$

$$[\mathrm{OH^*}] = \frac{\mathrm{K_8 p(H_2O)}}{\sqrt{\frac{\mathrm{p(H_2)}}{\mathrm{K_9}}}}[*] \quad (4\text{-}27)$$

where K_9 is the equilibrium constant for the dissociative adsorption of H_2, K_{10} is the equilibrium constant for the CO adsorption onto a Ni site, and K_8 is the equilibrium constant for the dissociative adsorption of H_2O as H* and OH* intermediates. For all other species, the pseudo steady state hypothesis is applied, indicating that the formation and consumption of the are equally fast and the coverage of the species remains constant.

For **Case (a)** (Step 4a and 5a) the coverage of $[O^*_a]$ and $[C^*_a]$ is described as

$$[\mathrm{O^*_a}] = \frac{\mathrm{k_6 p(CO_2)}[*]^2}{\mathrm{k_6}[\mathrm{C^*_a}] + \mathrm{k_7}[\mathrm{H^*}]} \quad (4\text{-}28)$$

$$[\mathrm{C^*_a}] = \frac{\mathrm{k_1 p(CH_4)}[*]^2}{\mathrm{k_{5a}}[\mathrm{O^*_a}]} \quad (4\text{-}29)$$

k_6 is the rate constant for the dissociative adsorption of CO_2 and k_{5a} is the rate constant for the reaction of C* from the surface with O*. Both equations are directly interdependent and by substitution, we obtain the terms (4-30) and (4-31):

$$[O^*_a] = \left(\frac{k_6 p(CO_2) - k_1 p(CH_4)}{k_7 \sqrt{\frac{p(H_2)}{K_9}}} \right) [*] \tag{4-30}$$

$$[C^*_a] = \left(\frac{k_1 k_7 \sqrt{\frac{p(H_2)}{K_9}}\, p(CH_4)}{k_{5a}(k_6 p(CO_2) - k_1 p(CH_4))} \right) [*] \tag{4-31}$$

The surface coverage of the hydrocarbons in case **(a)**, $[CH_{x,a}*]$, can be described as

$$[CH_{x,a}{}^*] = \left(\frac{k_1 p(CH_4)}{k_{x,a}} \right) [*] \tag{4-32}$$

where $k_{x,a}$ is the rate constant for the combination of the dehydration steps of CH_3*, CH_2* and CH* and k_1 of the activation of the CH_4 on the surface. As COH* is not contained as surface species in case **(a)**, we now have the relevant descriptions available and we can denote $[T]_a$ as given in equation (4-33):

$$[T]_a = 1 = \left(1 + \frac{k_1 k_7 \sqrt{\frac{p(H_2)}{K_9}}\, p(CH_4)}{k_{5a}(k_6 p(CO_2) - k_1 p(CH_4))} + \frac{k_1 p(CH_4)}{k_{x,a}} + \frac{p(CO)}{K_{10}} + \sqrt{\frac{p(H_2)}{K_9}} + \frac{K_8 p(H_2O)}{\sqrt{\frac{p(H_2)}{K_9}}} + \frac{k_6 p(CO_2) - k_1 p(CH_4)}{k_7 \sqrt{\frac{p(H_2)}{K_9}}} \right) [*] \tag{4-33}$$

In Case **(b)** the terms for the surface species [H*], [CO*], [OH*] are identical to Case **(a),** but the terms for $[O^*_b]$ and $[CH_{x,b}*]$ differ and the term for $[COH^*_b]$ is additionally considered. In this case, $[CH_{x,b}*]$ only describes CH_3* and CH_2*, because CH* participates in the network differently and is expressed as $[CH^*_b]$.

The term for $[CH_{x,b}*]$ can be denoted as:

$$[CH_{x,b}{}^*] = \frac{k_1 p(CH_4)[*]}{k_{x,b}} \tag{4-34}$$

In this case the terms for $[O^*_b]$, $[CH^*_b]$ and $[COH^*_b]$ are

$$[O^*_b] = \frac{k_6 p(CO_2)[*]^2}{k_{4b}[CH^*_b] + k_7[H^*]} \tag{4-35}$$

$$[CH^*_b] = \frac{k_1 p(CH_4)[*]^2}{k_{4b}[O^*_b]} \tag{4-36}$$

$$[COH^*_b] = \frac{k_{4b}[CH^*_b][O^*_b]}{k_{5b}[*]} \tag{4-37}$$

where k_{4b} is the rate constant for COH^*_b-formation from CH^*_b and O^*_b and k_{5b} is the rate constant for the decomposition of COH^*_b into CO* and H*. Substitution gives the terms (4-38), (4-39) and (4-40) with the sole dependence on the partial pressure of the respective gasses, the amount of free sites as well as rate and equilibrium constants.

$$[O^*_b] = \left(\frac{k_6 p(CO_2) - k_1 p(CH_4)}{k_7 \sqrt{\frac{p(H_2)}{K_9}}} \right) [*] \tag{4-38}$$

$$[CH^*_b] = \left(\frac{k_1 k_7 \sqrt{\frac{p(H_2)}{K_9}}\, p(CH_4)}{k_{4b}(k_6 p(CO_2) - k_1 p(CH_4))} \right) [*] \tag{4-39}$$

$$[COH^*_b] = \frac{k_1 p(CH_4)}{k_{5b}} [*] \tag{4-40}$$

Please note here, that the terms for $[O^*_a]$ and $[O^*_b]$ are identical and, therefore, will be referred to as [O*] from now on. This renders the equation for the total number of sites in Case **(b)** $[T]_b$ to be:

$$[T]_b = \left(1 + \frac{k_1 p(CH_4)}{k_{x,b}} + \frac{k_1 k_7 \sqrt{\frac{p(H_2)}{K_9}}\, p(CH_4)}{k_{4b}(k_6 p(CO_2) - k_1 p(CH_4))} + \frac{p(CO)}{K_{10}} + \sqrt{\frac{p(H_2)}{K_9}} + \frac{K_8 p(H_2O)}{\sqrt{\frac{p(H_2)}{K_9}}} + \frac{k_6 p(CO_2) - k_1 p(CH_4)}{k_7 \sqrt{\frac{p(H_2)}{K_9}}} + \frac{k_1 p(CH_4)}{k_{5b}} \right) [*] \tag{4-41}$$

Now all the terms for the species are derived and the rate equations for the CH_4 conversion in the individual scenarios can be described.

In the following, we will discuss the surface coverage of the individual species. We assume here that the species $[CH_{x,a}]$, $[CH_{x,b}]$ and $[COH^*_b]$ are the most abundant reaction intermediates (MARI) [52]. This means that $[CH_{x,a}]$ or $[CH_{x,b}]$ and $[COH^*_b]$ dominate the

surface coverage and they are present on the surface to much greater extent than the other species. This assumption is based on the fact that all other species, [H*], [OH*], [O*], [CO*], [C*$_a$] and [CH*$_b$] depend on at least one of the products, H_2, CO or H_2O. Those gasses are of zero order; they do not impact on the reforming rate and therefore their influences on the surface coverage also assumed as insignificant.

The question to be addressed at this point is the relation between the pronounced formation of carbon-nano tubes (Figure 4-3 and Figure 4-4) and the very low coverage in C*. To address this, let us point to Figure 4-2, which shows increasing catalytic activity during the first minutes of DRM (< 100 min). This means that the formation of carbon to a certain extent does not influence the performance of the catalyst, but it rather enhances DRM by supplying activated C* or CH_x* species to the active sites. We hypothesize that these active carbon species to form CO* or COH*, in a reaction with O* or CO_2*, which are, therefore, needed to continuously clean the surface [41].

The two terms for $[T]_a$ and $[T]_b$, under the MASI assumption for C*, CH* and COH* can be expressed as

$$[T]_a = 1 = \left(1 + \frac{k_1 p(CH_4)}{k_{x,a}}\right)[*] \tag{4-42}$$

$$\begin{aligned}[T]_b = 1 &= \left(1 + \frac{k_1 p(CH_4)}{k_{x,b}} + \frac{k_1 p(CH_4)}{k_{5b}}\right)[*] \\ &= \left(1 + \frac{k_1 (k_{x,b} + k_{5b}) p(CH_4)}{k_{x,b} k_{5b}}\right)[*]\end{aligned} \tag{4-43}$$

Substituting $k_1/k_{x,b}$ by k_a in term (4-42) and $\frac{k_1(k_{x,b}+k_{5b})}{k_{x,b}k_{5b}}$ by k_b in term (4-43) gives

$$[T]_a = 1 = \left(1 + k_a p(CH_4)\right)[*] \quad \text{and} \quad [T]_b = 1 = \left(1 + k_b p(CH_4)\right)[*] \tag{4-44}$$

Thus the two expressions for the number of total sites are identical. For simplification, we will refer to both, k_a and k_b from now on as $k_{a/b}$. Using $[T]_a$ and $[T]_b$ together with the just mentioned simplification, one obtains the following expression for $[*]$:

$$[*] = \frac{[T]_a}{\left(1 + k_{a/b} p(CH_4)\right)} = \frac{[T]_b}{\left(1 + k_{a/b} p(CH_4)\right)} = \frac{1}{\left(1 + k_{a/b} p(CH_4)\right)} \tag{4-45}$$

Two possible scenarios for the rate-determining step were developed above. CH_4 activation as the RDS in the first scenario is challenging to imagine, as it would not be

compatible with the first order dependence on CO_2 in Regime 1. In this scenario, the surface coverage depends strictly on the partial pressure of CH_4 and the RDS would be the activation of CH_4 on the surface, which can be calculated by inserting (4-45) into term (4-19), resulting to the forward turnover rate to be:

$$r_{DRM,1+2} = \frac{k_1 p(CH_4)}{\left(1 + k_{a/b} p(CH_4)\right)^2} \quad (4\text{-}46)$$

This rate equation is independent of the partial pressure of CO_2, which indicates that the dehydrogenation of CH_4 cannot be the RDS in this system as it neglects the observed impact of CO_2 on the reaction kinetics.

We will continue the derivation of the rate equation for the two regimes with this step and investigate the differences and similarities between the two cases of oxidation as RDS.

In **Regime 1,** Ni surfaces are highly occupied with the carbonaceous species in comparison to the fractional coverages of H* and O* and the rates of methane conversion increase with an increase in CO_2 partial pressure. RWGS does not occur at measurable rates and water is only marginally formed at partial pressures of CO_2 <100 kPa. Consequently, the assumed RDS of RWGS, which is the formation of OH* from O* and H* does not occur and is negligible with respect to the oxidation of surface carbon. From the experimental data, we propose that the term $k_1p(CH_4)$ is much larger than term $k_6p(CO_2)$ in this regime. In Case **(a)**, the equation (4-20) is substituted with term (4-28) to form:

$$r_{DRM,a1} = k_{5a}[C^*_a][O^*_a] = k_{5a}[C^*_a]\frac{k_6 p(CO_2)[*]^2}{k_{5a}[C^*_a] + k_7[H^*]} \quad (4\text{-}47)$$

If $k_7[H^*]$ is negligible it becomes 0 and term (4-47) can be re-written as:

$$r_{DRM,a1} = k_6 p(CO_2)[*]^2 \quad (4\text{-}48)$$

In Case **(b)**, under the same assumption ($k_7[H^*] << k_{4b}[CH^*_b]$), term (4-21) can substituted by (4-35), $k_7[H^*]$ also becomes negligible and the equation can be re-written as:

$$r_{DRM,b1} = k_{4b}[CH^*_b][O^*] = k_{4b}[CH^*_b]\frac{k_6 p(CO_2)[*]^2}{k_{4b}[CH^*_b] + k_7[H^*]} = k_6 p(CO_2)[*]^2 \quad (4\text{-}49)$$

The two equations for $r_{DRM,a}$ and $r_{DRM,b}$ are identical, which means that in **Regime 1** we cannot distinguish between Cases **(a)** and **(b).** $[*]$ can be substituted from the equation by using term (4-45) in either of the equations (4-48) and (4-49), which gives

$$r_{DRM,1} = \frac{k_6 p(CO_2)}{\left(1 + k_{a/b} p(CH_4)\right)^2} \tag{4-50}$$

In **Regime 2**, $k_6p(CO_2)$ approaches the same order of magnitude, as the term $k_1p(CH_4)$ and the equations that describe the rate of DRM, (4-20) for case (a) and (4-21) for case (b), respectively, can now be denoted as

$$r_{DRM,a2} = k_{5a}[C^*_a][O^*] = k_1 p(CH_4)[*]^2 = \frac{k_1 p(CH_4)}{\left(1 + k_{a/b} p(CH_4)\right)^2} \tag{4-51}$$

$$r_{DRM,b2} = k_{4b}[CH^*_b][O^*] = k_1 p(CH_4)[*]^2 = \frac{k_1 p(CH_4)}{\left(1 + k_{a/b} p(CH_4)\right)^2} \tag{4-52}$$

Just like in Regime 1, there is mathematically no difference between activation of the C* and the insertion of O* into the CH* (equations (4-51) and (4-52)). The resulting rate equation in Regime 2 is term (4-53):

$$r_{DRM,2} = \frac{k_1 p(CH_4)}{\left(1 + k_{a/b} p(CH_4)\right)^2} \tag{4-53}$$

Now having the DRM rate equations defined for all scenarios, the RWGS reaction can be addressed. The experimental data suggest that RWGS does not occur in **Regime 1** and, therefore, $r_{RWGS,1}$ equals 0. In **Regime 2**, the RWGS is significant with the combination of H* and O* being the rate determining step. Term (4-22) describes the RWGS reaction; [H*] is substituted by term (4-25) and [O*] by term (4-30) (or term (4-35), respectively). DRM and RWGS use the same active sites. Hence, the term for the free sites $[*]$ is identical for both reactions and described by term (4-45). This leads to the final term for the RWGS reaction (4-55):

$$\begin{aligned} r_{RWGS} &= k_7 \sqrt{\frac{p(H_2)}{K_9}} \left(\frac{k_6 p(CO_2) - k_1 p(CH_4)}{k_7 \sqrt{\frac{p(H_2)}{K_9}}} \right) [*]^2 \\ &= \left(k_6 p(CO_2) - k_1 p(CH_4)\right)[*]^2 \end{aligned} \tag{4-54}$$

$$r_{RWGS} = \frac{\left(k_6 p(CO_2) - k_1 p(CH_4)\right)}{\left(1 + k_{a/b} p(CH_4)\right)^2} \tag{4-55}$$

Under the given reaction conditions, the rate of CO_2 conversion (r_{CO_2}) can be described as the sum of RWGS and DRM (term (4-56))

$$r_{CO_2} = r_{DRM} + r_{RWGS} \tag{4-56}$$

In **Regime 1** there is no observable RWGS, so the conversion rate of CO_2 is equal to the DRM rate, as given in term (4-50):

$$r_{CO_2,1} = r_{DRM,1} + 0 = \frac{k_6 p(CO_2)}{\left(1 + k_{a/b} p(CH_4)\right)^2} \tag{4-57}$$

In **Regime 2** the conversion rate of CO_2 can be calculated from the terms (4-53), (4-55) and (4-56) resulting into:

$$\begin{aligned} r_{CO_2,2} &= \frac{k_1 p(CH_4)}{\left(1 + \frac{k_a}{b} p(CH_4)\right)^2} + \frac{\left(k_6 p(CO_2) - k_1 p(CH_4)\right)}{\left(1 + \frac{k_a}{b} p(CH_4)\right)^2} \\ &= \frac{k_6 p(CO_2)}{\left(1 + k_{a/b} p(CH_4)\right)^2} \end{aligned} \tag{4-58}$$

Now all necessary equations are formulated to describe DRM, RWGS and conversion of CO_2 in the system; relevant terms are compiled in table 4-2. It should be noted that the two rate equations for the conversion of CO_2 are identical for the two regimes. This means that the CO_2 conversion is independent from the CH_4/CO_2 ratio, while the DRM and the RWGS reactions are dependent on the ratio between the two reactants.

Table 4-2 Summary of the rate equations for DRM and RWGS and for CO_2 conversion. The terms were deduced for the two regimes of $CH_4/CO_2 > 2$ and $CH_4/CO_2 < 2$.

	Regime 1	**Regime 2**
DRM	$r_{DRM,1} = \frac{k_6 p(CO_2)}{\left(1 + k_{a/b} p(CH_4)\right)^2}$	$r_{DRM,2} = \frac{k_1 p(CH_4)}{\left(1 + k_{a/b} p(CH_4)\right)^2}$
RWGS	0	$r_{RWGS} = \frac{\left(k_6 p(CO_2) - k_1 p(CH_4)\right)}{\left(1 + k_{a/b} p(CH_4)\right)^2}$
CO_2 conversion	$r_{CO_2,1} = \frac{k_6 p(CO_2)}{\left(1 + k_{a/b} p(CH_4)\right)^2}$	$r_{CO_2,2} = \frac{k_6 p(CO_2)}{\left(1 + k_{a/b} p(CH_4)\right)^2}$

These equations depend only on the partial pressures of the two reactants CH_4 and CO_2 and on the rate constants k_1, k_6 and $k_{a/b}$. The values for these constants were obtained by fitting the determined terms to the experimentally obtained data.

Equation (4-50) is used to fit the data for CH_4/CO_2 >2, hence the data in Figure 4-6 at CO_2 partial pressures below 100 kPa. The data in the graph above 100 kPa is fitted with equation (4-53). The data presented in Figure 4-8 has completely measured in Regime 2 and therefore fitted with (4-53). The results of the fits can be found in table 4-3.

Table 4-3 Summary of the fitted kinetic values

	k_1 [$kPa^{-1}sec^{-1}$]	k_6 [$kPa^{-1}sec^{-1}$]	$k_{a/b}$ [$kPa^{-1/2}$]
Fitted value	3.34 ± 0.08	5.41 ± 0.12	0.003 ± $7 \cdot 10^{-5}$

The rate constant for the activation of CH_4 on the Ni surface, k_1, is 3.34 $kPa^{-1}sec^{-1}$ and, therefore, smaller than the rate constant of CO_2 activation on the same sites (k_6 = 5.41 $kPa^{-1}sec^{-1}$). The similar magnitudes of these rate constants will have them contributing equally to the reforming reaction. The value of $k_{a/b}$, which describes the surface coverage of hydrocarbons, is very low (0.003 kPa^{-1}) and, therefore, indicates that the surface concentration of these species is also very low. The experimental data was plotted against the calculated results and the resulting graphs can be found in Figure 4-12. A perfect fit of the experimental data was archived. The measured and calculated DRM forward turnover rates are compared Figure 4-12 (a) and in Figure 4-12 (b) as a function of the CO_2 and CH_4 partial pressure, respectively. The CO_2 forward conversion rates and the results of the fit are shown in Figure 4-12 (c) as a function of the CO_2 partial pressure.

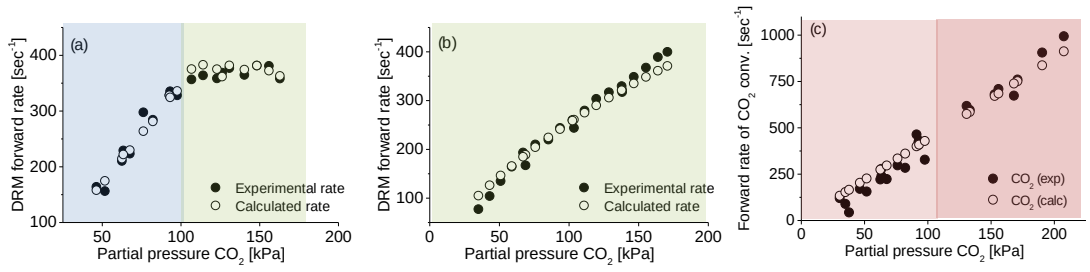

Figure 4-12 DRM forward rates (a) and (b) and for the CO_2 forward conversion rates (c). The data in the blue covered area was fitted with equation (4-50), data in green with equation (4-53). The CO_2 conversion was fitted with the two equations (4-57) (light red) and (4-58) (deep red), respectively. The two latter equations are identical but originate from different calculation pathways.

The resulting rate values for DRM were compared with the experimentally measured data in Figure 4-13, which indicates the good fit of the model to the experimentally found values.

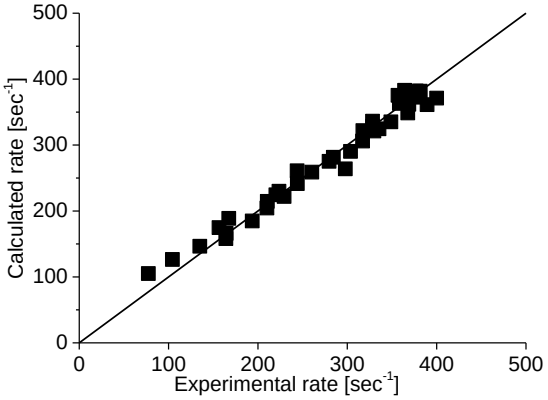

Figure 4-13 Predicted data shown against the experimentally obtained rate values for the DRM rates

1.4 Conclusion

Rate measurements of CH_4-CO_2 reactions under severe deactivating conditions at high pressures and temperatures led to a mechanistic proposal that captures two distinctly different kinetic regimes for dry reforming and reverse-water-gas-shift reactions. In regime 1, at low CO_2 partial pressures (CH_4/CO_2 ratios above 2), the RWGS does not occur at detectable rates, because the concentrations of reactive oxygen species at Ni crystallite surfaces were small at low CO_2 partial pressures. This implies that the rate for the RWGS is low although H_2 is formed by the DRM reaction due to the low oxygen content on the surface. The methane bond activation proceeds independently followed by the dehydrogenation cascade forming surface carbon and hydrogen. However, in this regime the system lacks oxygen species to re-activate the carbon and increasing pressure in CO_2, also enhances the reforming rate by scavenging carbon from the active sites.

At CH_4/CO_2 ratios below 2, the forward CH_4 conversion rate changes from linearly dependence on the partial pressure of CO_2 to complete insensitivity. It is not possible to describe this change, if the activation of CH_4 would be the only kinetically relevant step across all CH_4/CO_2 ratios. In this case, the reaction should not depend on the partial pressure of CO_2 at all. The direct dependence on the CO_2 concentration relative to CH_4 is observed, because the rate determining step for DRM in deficit of CO_2 at $CH_4/CO_2 >$ 2 depends on the oxidation of surface carbon (C*) freeing sites active for CH_4 dissociation.

The fact that carbon deposition occurs under all conditions without influencing the observed activity of the catalyst suggests sufficiently high carbon mobility such that the

CNT formation should not markedly influence the reaction rates under all conditions studied. The possibility to form carbon-nano tubes over Ni catalyst from CO via Boudouard reaction has been described in literature before [53]. We could also show in earlier studies that a significant amount of carbon in the carbon fibers originates from Boudouard reaction but CO partial pressures applied and conversions reached during the previous work were much higher than in the present study [21]. At a first glance, this might contradict the reaction network presented in this work in which the only source of carbon is dehydrated CH_4. However, the finding of severe carbon deposition despite very constant activity in dry reforming suggests that the carbon deposition and the reforming itself occur kinetically independent from one another. It is even possible that the two processes do not occur on the same sites. TEM pictures provide evidence that most of the Ni particles on the surface are free of deposits while some of them are encapsulated within carbon-nano tubes Figure 4-3. The free Ni particles might be active in the reforming and those incorporated into the carbon tubes might be actively deposing carbon onto the surface in the form of fibers. The CO necessary for the latter process could freely migrate over the surface or even though the gas phase and be bound somewhere completely different. Decreasing the CO_2 (or H_2O partial pressure in steam reforming, respectively) directly increases the percentage of Ni particles participating in the carbon deposition and finally in deactivation. This is clearly visible in the methane activation measurements in which no oxygen provider is available. The Ni-catalyst, active for hours without deactivation in DRM, deactivated within seconds losing all its activity (Figure 4-5). At a CH_4/CO_2 ratio of 2 and lower, the share of Ni particles active in DRM has reached its maximum and those Ni particles will also stay free of carbon and active in DRM. A minor percentage of Ni is still encapsulated into CNTs, inactive in DRM but still able to split dissociate CO via the Boudouard reaction into carbon nano-tubes.

Kinetically, there are several important statements that need to be made regarding the formation of active carbon: (1) the first C-H bond cleavage in CH_4 is much slower than that C-H bond cleavage in the other CH_x* species, (2) the dehydrogenation cascade, which is building up surface carbon C* is unidirectional and (3) CH_4 is the only source of active surface carbon C* in the system and the coke formation via reverse Boudouard does not occur on the DRM active sites. This leads to the conclusion that in Regime 2, under conditions richer in CO_2 but still in an excess of CH_4, the rapid reactions of CO_2* or O* maintains all sites active for CH_4 dissociation, leading to a maximum rate, for the rate determining CH_4 dissociation, which depends (as in all regimes) only on the partial pressure of methane.

It is unequivocally shown that the only reasonably abundant species on the catalyst´s surface are CH_x* and COH* being also the only components depending on the kinetically relevant CO_2 or CH_4 pressures. However, even those species appear not to be present in large concentrations on the active sites at $CH_4/CO_2 > 2$ as the kinetic constants calculated for their formation is several orders of magnitude smaller than other relevant constants. Thus, it is concluded that the C* formed during the reaction migrates rapidly from the active sites to sites where it forms carbon fibers, which could be on the metal particle, but also on sites at the support. In neither case, coke deposition does not influence the activity of the catalyst.

Finally, in the proposed reaction network two cases for RDS´s were investigated for the reaction of the surface species CH*. However, there is kinetically no difference between the two cases, allowing not to kinetically differentiating between these pathways.

In the present work, a complete reaction network is presented, which describes not only the dry reforming of methane at elevated pressures but also the most important side reaction, the reverse water-gas-shift under very severe conditions. At high CH_4/CO_2 ratios, the kinetically relevant component is CO_2, whose higher partial pressure increases the concentration of sites active for CH_4 dissociation. At lower ratios, a maximum concentration of sites active for CH_4 dissociation is achieved and only the CH_4 pressure determines the rate.

1.5 Acknowledgements

The authors acknowledge the chemisorption measurements, for which we thank Franz-Xaver Hecht as well as Katia Rodewald and Martin Neukamm for the electron microscopy measurements.

1.6 Literature

[1] M.-S. Fan, A.Z. Abdullah, S. Bhatia, ChemCatChem, 1 (2009) 192.
[2] M.C.J. Bradford, M.A. Vannice, Cat. Rev. - Sci. Eng., 41 (1999) 1.
[3] J. Wei, E. Iglesia, J. Catal., 224 (2004) 370.
[4] J. Wei, E. Iglesia, J. Phys. Chem. B, 108 (2004) 4094.
[5] J. Wei, E. Iglesia, J. Catal., 225 (2004) 116.
[6] A. Yamaguchi, E. Iglesia, J. Catal., 274 (2010) 52.
[7] W. Hally, J.H. Bitter, K. Seshan, J.A. Lercher, J.R.H. Ross, in: B. Delmon, G.F. Froment (Eds.) Catalyst Deactivation, 1994, pp. 167.
[8] J.H. Bitter, W. Hally, K. Seshan, J.G. vanOmmen, J.A. Lercher, Catal. Today, 29 (1996) 349.
[9] J.H. Bitter, K. Seshan, J.A. Lercher, J. Catal., 171 (1997) 279.
[10] J.H. Bitter, K. Seshan, J.A. Lercher, J. Catal., 176 (1998) 93.
[11] K. Seshan, J.H. Bitter, J.A. Lercher, in: T.S.R. Rao, G.M. Dhar (Eds.) Recent Advances in Basic and Applied Aspects of Industrial Catalysis1998, pp. 187.
[12] J.H. Bitter, K. Seshan, J.A. Lercher, J. Catal., 183 (1999) 336.
[13] T. Roussière, L. Schulz, K.M. Schelkle, G. Wasserschaff, A. Milanov, E. Schwab, O. Deutschmann, A. Jentys, J. Lercher, S.A. Schunk, ChemCatChem, 6 (2014) 1447.
[14] J.A.C. Dias, J.M. Assaf, Catal. Today, 85 (2003) 59.
[15] S. Corthals, T. Witvrouwen, P. Jacobs, B. Sels, Catal. Today, 159 12.
[16] S. Corthals, J. Van Nederkassel, H. De Winne, J. Geboers, P. Jacobs, B. Sels, Appl. Catal., B, 105 (2011) 263.
[17] C. Daza, O. Gamba, Y. Hernández, M. Centeno, F. Mondragón, S. Moreno, R. Molina, Catal. Lett., 141 (2011) 1037.
[18] Z. Xu, M. Zhen, Y. Bi, K. Zhen, Appl. Catal., A, 198 (2000) 267.
[19] W. Wintruff, Kristall und Technik, 9 (1974) 391.
[20] L. Maier, B. Schädel, K. Herrera Delgado, S. Tischer, O. Deutschmann, Top. Catal., 54 (2011) 845.
[21] L.A. Schulz, L.C.S. Kahle, K.H. Delgado, S.A. Schunk, A. Jentys, O. Deutschmann, J.A. Lercher, Appl. Catal., A, 504 (2015) 599.
[22] Y. Cui, H. Zhang, H. Xu, W. Li, Appl. Catal., A, 318 (2007) 79.
[23] J.-S. Chang, S.-E. Park, J.W. Yoo, J.-N. Park, J. Catal., 195 (2000) 1.
[24] A.K. Avetisov, J.R. Rostrup-Nielsen, V.L. Kuchaev, J.H. Bak Hansen, A.G. Zyskin, E.N. Shapatina, J. Mol. Catal. A: Chem., 315 (2010) 155.
[25] G. Jones, J.G. Jakobsen, S.S. Shim, J. Kleis, M.P. Andersson, J. Rossmeisl, F. Abild-Pedersen, T. Bligaard, S. Helveg, B. Hinnemann, J.R. Rostrup-Nielsen, I. Chorkendorff, J. Sehested, J.K. Nørskov, J. Catal., 259 (2008) 147.
[26] J.R. Rostrupnielsen, J.H.B. Hansen, J. Catal., 144 (1993) 38.
[27] H.-W. Chen, C.-Y. Wang, C.-H. Yu, L.-T. Tseng, P.-H. Liao, Catal. Today, 97 (2004) 173.
[28] R.M. Watwe, H.S. Bengaard, J.R. Rostrup-Nielsen, J.A. Dumesic, J.K. Nørskov, J. Catal., 189 (2000) 16.
[29] J.R. Rostrup-Nielsen, J. Catal., 85 (1984) 31.
[30] G. Sierra Gallego, C. Batiot-Dupeyrat, J. Barrault, F. Mondragón, Ind. & Eng. Chem. Res., 47 (2008) 9272.
[31] T.H. Gardner, D. Shekhawat, D.A. Berry, M.W. Smith, M. Salazar, E.L. Kugler, Appl. Catal., A, 323 (2007) 1.
[32] T.H. Gardner, J.J. Spivey, E.L. Kugler, A. Campos, J.C. Hissam, A.D. Roy, Journal of Physical Chemistry C, 114 (2010) 7888.
[33] J. Wang, D. Meng, X. Wu, J. Hong, D. An, K. Zhen, React. Kinet. Catal. Lett., 96 (2009) 65.
[34] K. Song, Y. Seo, H. Yoon, S. Cho, Korean J. Chem. Eng., 20 (2003) 471.

[35] G. Groppi, C. Cristiani, P. Forzatti, Appl. Catal., B, 35 (2001) 137.
[36] C.S. Brooks, G.L.M. Christopher, J. Catal., 10 (1968) 211.
[37] J.A. Moulijn, A.E. van Diepen, F. Kapteijn, Appl. Catal., A, 212 (2001) 3.
[38] F. Barrai, T. Jackson, N. Whitmore, M.J. Castaldi, Catal. Today, 129 (2007) 391.
[39] V.Y. Bychkov, Y.P. Tyulenin, A.A. Firsova, E.A. Shafranovsky, A.Y. Gorenberg, V.N. Korchak, Appl. Catal., A, 453 (2013) 71.
[40] J.A. Lercher, J.H. Bitter, W. Hally, W. Niessen, K. Seshan, in: W.N.D.E.I. Joe W. Hightower, T.B. Alexis (Eds.) Stud. Surf. Sci. Catal., Elsevier1996, pp. 463.
[41] Z.L. Zhang, X.E. Verykios, Catal. Today, 21 (1994) 589.
[42] P. Djinović, I.G. Osojnik Črnivec, B. Erjavec, A. Pintar, Appl. Catal., B, 125 (2012) 259.
[43] M. Meyyappan, D. Lance, C. Alan, H. David, Plasma Sources Sci. Technol., 12 (2003) 205.
[44] M.C.J. Bradford, M.A. Vannice, Appl. Catal., A, 142 (1996) 97.
[45] B.R. Jovanić, B. Viana, Optics Communications, 282 (2009) 1798.
[46] D. Baudouin, U. Rodemerck, F. Krumeich, A.d. Mallmann, K.C. Szeto, H. Ménard, L. Veyre, J.-P. Candy, P.B. Webb, C. Thieuleux, C. Copéret, J. Catal., 297 (2013) 27.
[47] M.M.V.M. Souza, D.A.G. Aranda, M. Schmal, J. Catal., 204 (2001) 498.
[48] J.M. Bermúdez, B. Fidalgo, A. Arenillas, J.A. Menéndez, Fuel, 94 (2012) 197.
[49] S. Wang, G.Q. Lu, G.J. Millar, Energy & Fuels, 10 (1996) 896.
[50] M.C.J. Bradford, M.A. Vannice, J. Catal., 173 (1998) 157.
[51] N.-o. Matsui, K. Anzai, N. Akamatsu, K. Nakagawa, N.-o. Ikenaga, T. Suzuki, Appl. Catal., A, 179 (1999) 247.
[52] A. Frennet, in: R.W. Joyner, R.A. Santen (Eds.) Elementary Reaction Steps in Heterogeneous Catalysis, Springer, Netherlands, 1993, pp. 423.
[53] J.W. Snoeck, G.F. Froment, M. Fowles, Ind. & Eng. Chem. Res., 41 (2002) 4252.

4.1 License and contributions

A publication under the topic "*Methane dry reforming on Ni supported on hexa-aluminate catalysts at elevated pressures*" is planned before the final publication of this thesis.

Authors of the publication are:

Linus A. Schulz, Yu Lou, Andreas Jentys, Johannes A. Lercher*
Technische Universität München
Department of Chemistry and Catalysis Research Center
Lichtenbergstraße 4, 85747 Garching, Germany

Weifeng Tu, Ya-Huei (Cathy) Chin
University of Toronto
Faculty of Engineering & Applied Catalysis
Multidisciplinary Laboratory for Innovative Catalytic Science
200 College Street, Toronto, Ontario, M5S 3E5, Canada

Synthesis of the Ni catalysts, N_2-sorption, electron microscopy, kinetic and methane activation experiments were conducted by Technische Universität München. University of Toronto provided significant input on the design of experiments. Interpretation of the experimental results and the derivation of the rate equation were achieved in close cooperation of all involved authors.

5 Summary

The scope of this work was to address the dry reforming of methane under conditions relevant for technical application, which means more than 10 MPa and 1000 K. In a bottom-up-approach, a series of catalyst materials were produced and their behavior in dry reforming was tested. The best-performing material was then taken to further investigations of its carbon-deposition characteristics and reaction kinetics. The combined results provide a full picture of the processes on the catalyst´s surface during the reaction.

Introductory, a review is given on the physio-chemical background and the thermodynamics of dry reforming. The major obstacles for successful implementation of the technique into large scale production, in particular carbon deposition, are discussed. Increasing temperature, decreasing pressure and the employment of noble metal catalysts enhance the reaction and reduce carbon deposition but are usually very costly. The various reaction mechanisms described in literature are summarized and finally the characteristics of numerous catalytic systems known for dry reforming are presented. The section is concluded with a detailed description of the reaction setup and its single-pass and recycle mode.

The second section focuses on the ideal synthesis route of hexaaluminates. Firstly, the counter ions La^{3+}, Ba^{2+} and Sr^{2+} are tested with respect to their influence on activity and stability during DRM. La^{3+} reveals the best stability at moderate activity and is therefore selected over the very active but also very unstable Ba^{2+} and Sr^{2+} materials. Secondly, two different synthesis routes to LaNi-hexaaluminates are tested, recrystallization and PEG-supported synthesis, with the latter providing significantly increased contents of the desired hexaaluminate phases. In both routes 1, 5 and 10 wt.-% of Ni are employed to produce the material and an optimum with an increase up to 96 wt.-% of hexaaluminate phase is observed for 5 wt.-% of Ni. This results in much better stability against reduction of the Ni and into significantly slower deactivation during the dry reforming reaction. As the structural properties (surface and metal dispersion) do not exhibit any differences, the dissimilarities in reactivity can be assigned to the intrinsic phase composition of the materials. The best performing material in the series is the catalyst from the PEG-supported synthesis containing 5 wt.-% Ni (PEG 5). It was therefore tested in detail with respect to its properties in carbon deposition and a kinetic description of the dry reforming of methane was done on this material.

The third section describes a comparison of the PEG5 material to a quasi-commercial Pt-catalyst. The two materials are similarly active but simultaneously Ni exhibits much higher carbon deposition than Pt. The isotope labelling reveals that the hydrocarbon species on the

surface of the catalyst are completely broken down to surface carbon and subsequently re-activated. This reactivation is strongly reduced on the Ni material in comparison to the Pt-catalyst, which is the main reason for the base metal to be much more prone to coke deposition than the noble metal. This means that a good catalyst – which in this case means a carbon stable catalyst – needs to make a good tradeoff between activation of the reactants and removal of the carbon from the surface. Especially, because the formation of surface carbon is a mandatory elemental step in the reaction network.

Knowing the elemental steps of the reaction, a kinetic description of the reaction is possible, which is the topic of the last section. The reforming is under the given conditions only dependent on the two reactant gasses CO_2 and CH_4 but independent on the primary and secondary products. However, the reaction order in CO_2 shifts from 1 to 0 as the CH_4/CO_2 ratio drops below 2. This leads to the assumption that the rate determining step of reforming itself it not the activation of CH_4 on the metal but rather the re-activation of the surface carbon, after complete dehydrogenation, with oxygen-containing species. The kinetic parameters of the reaction are calculated and fit to the experimental data showing good coincidence.

This work gives a complete overview of Ni-hexaaluminates as DRM catalysts. It starts with a bottom-up approach to a synthesis route for $LaNi_{0.7}Al_{11.3}O_{19}$, being optimized by structural and phase composition measurements. The subsequent measurements in single pass and recycle give a close-up picture of the DRM elemental steps and their indications on the kinetics of the reaction. Especially the importance of the reactivation of surface bound carbon for the mechanism and the deactivation is evidently disclosed.

6 Zusammenfassung

Die sich ändernde Zusammensetzung fossiler Rohstoffe macht neue Prozesse notwendig um der steigenden Verfügbarkeit von CH_4 und CO_2 Rechnung zu tragen. Eine Möglichkeit ist die Herstellung von Synthesegas aus den beiden Komponenten durch das trockene Reformieren von CH_4. Diese Reaktion ist derzeit großtechnisch noch nicht weit verbreitet, da sie noch immer einige schwerwiegende Nachteile aufweist – vor allem die starke Koksbildung an Basismetallen, wie Ni. Zielsetzung dieser Arbeit war eine Beschreibung der trockenen Reformierung von CH_4 unter anwendungsnahen Bedingungen. In diesem Fall sind das Drücke über 10 MPa und Temperaturen über 1000 K. In einem Botton-Up-Ansatz wurde eine Serie an Ni-Materialien hergestellt und ihr Verhalten im trockenen Reformieren untersucht. Das beste Material wurde dann hinsichtlich seines Verkokungsverhaltens mit einem Pt-Katalysator verglichen und es wurde ein kinetisches Modell für dieses System aufgestellt. Die kombinierten Ergebnisse ermöglichen ein vollständiges Bild der Prozesse, die auf der Katalysatoroberfläche während dieser Reaktion ablaufen.

Einleitend wird ein Überblick über den aktuellen Stand der Forschung gegeben, insbesondere hinsichtlich des physio-chemischen Hintergrunds und der thermodynamischen Gegebenheiten. Zusätzlich werden die Hauptgründe für die bisher nicht eingetretene technische Implementierung der trockenen Reformierung angesprochen. Hierbei handelt es sich hauptsächlich um die schwer zu vermeidende Koksbildung unter hohen Drücken. Hohe Temperaturen, niedriger Druck oder auch die Verwendung von Edelmetallen als Katalysatoren wären gängige Mittel um die Kohlenstoffbildung zu unterdrücken, aber leider sind diese unter normalen Umständen teuer zu implementieren. Weiterhin werden die verschiedenen Reaktionsmechanismen, wie sie bereits in der Literatur beschrieben wurden, gegeneinandergestellt und die eine Reihe an katalytischen Systeme beschrieben und diskutiert. Abschließend wird das Reaktorsystem, mit seinem Single-Pass und seinem Recycle-Modus im Detail erklärt.

Das zweite Kapitel startet mit einem Vergleich der Gegenionen La^{3+}, Ba^{2+} und Sr^{2+}, wobei klar gezeigt werden kann, dass La-Hexaaluminate zwar weniger aktiv sind als die anderen beiden Sorten. Gleichzeitig weisen diese Materialien eine wesentlich erhöhte Stabilität in der trockenen Reformierung auf und sind deshalb klare Favoriten für eine zweite Generation an Katalysatoren. Der zweite Teil des Kapitels beschreibt die Syntheseroute für das Ni-Hexaaluminate und des Einflusses der Phasenzusammensetzung der Katalysatoren auf deren Stabilität gegen Reduktion sowie ihre Aktivität im trockenen Reformieren. Zwei Syntheserouten werden vorgestellt, die Rekristallisation und die PEG-gestützte Synthese,

wobei letztere stark erhöhte Anteile an den gewünschten Hexaaluminat-Phasen produziert. Für beide Routen werden Materialien mit 1, 5 und 10 Gew.-% hergestellt, wobei klar ein Optimum bei 5 Gew.-% Ni erkennbar ist. Dieses Material enthält bis zu 96 Gew.-% der gewünschten Hexaaluminat-Phase. Daraus folgen eine wesentlich höhere Stabilität gegenüber Reduktion sowie eine verbesserte Reformierungsaktivität. Da die Materialien strukturell (Oberfläche, Metalldispersion) keine nennenswerten Abweichungen aufweisen, ergeben sich die Unterschiede in Stabilität und Aktivität aus den verschiedenen Phasen-Zusammensetzungen. Das Material mit den besten Ergebnissen kommt aus der PEG-gestützten Synthese und enthält 5 Gew.-% Ni. Dieses Material wurde ausgesucht um die Kohlenstoff-Bildung detailliert zu untersuchen und eine kinetische Beschreibung des trockenen Reformierens zu erstellen.

Das dritte Kapitel vergleicht PEG5 mit einem Pt-Katalysator. Die beiden Materialien zeigen ähnliche Reformieraktivitäten, wobei das Ni-Material aber wesentlich mehr Koks ablagert als der Pt-Katalysator. Die Isotopenmarkierung der Edukte zeigt, dass die Kohlenwasserstoffe in der Reaktion komplett zu Kohlenstoff zersetzt werden und dieser sich auf der Oberfläche ablagert. In einem zweiten Schritt muss der Kohlenstoff dann wieder aktiviert werden um nicht zu bleibenden Ablagerungen zu werden. Diese Reaktivierung läuft über Ni wesentlich langsamer, als über Pt, was auch der Grund für die schlechtere Koksstabilität des Basismetalls ist. Das bedeutet, dass ein guter Katalysator – und in diesem Sinne ist ein guter Katalysator stabil gegenüber Koks-Bildung –einen guten Ausgleich finden zwischen der Aktivierung der Edukte und der Ablösung des Oberflächen-Kohlenstoffs sicherstellen muss. Dies ist umso wichtiger, als Oberflächen-Kohlenstoff ein elementarer Bestandteil des Reaktionsnetzwerkes im trockenen Reformieren darstellt.

Da nun die einzelnen Schritte der Reaktion bekannt sind, kann eine kinetische Beschreibung der Reaktion angefertigt werden, was im abschließenden Kapitels dieser Arbeit getan wird. Das trockene Reformieren ist unter den gegebenen Bedingungen von den beiden Eduktgasen CO_2 und CH_4 aber nicht von den primären oder sekundären Produkten abhängig. Gleichzeitig verschiebt sich die Reaktionsordnung von CO_2 von 1 auf 0 wenn das CH_4/CO_2 Verhältnis unter 2 sinkt. Daraus lässt sich ableiten, dass der ratenbestimmende Schritt des Reformierens nicht die Aktivierung von CH_4 auf der Metalloberfläche sein kann, sondern die Reaktivierung von Oberflächenkohlenstoff mit sauerstoffhaltigen Spezies ist. Dieser Oberflächenkohlenstoff entsteht durch vollständige Dehydrierung von CH_4. Der Fit der errechneten kinetischen Reaktionsparameter zeigt gute Übereinstimmung mit den experimentellen Daten.

Abschließend lässt sich sagen, dass diese Arbeit einen kompletten Überblick über die Eigenschaften von Ni-Hexaaluminaten als Trockenreformierkatalysatoren gibt. Beginnend mit einem Vergleich von verschiedenen Gegenionen und verschiedenen Syntheserouten wurde das Material gefunden, welches den Ausgleich bietet zwischen Aktivität und Stabilität. Dieses $LaNi_{0.7}Al_{11.3}O_{19}$ wurde dann im „Single-Pass“ und im „Recycle“ Modus, mit normalen und isotopenmarkierten Gasen untersuch und so ein genaues mechanistisches und kinetisches Bild gezeichnet. Dessen Kern bildet die Erkenntnis wie überaus wichtig Reaktivierung von adsorbiertem Kohlenstoff, sowohl für den Reaktionsmechanismus, als auch für die Stabilität gegenüber Deaktivierung, ist.

7 Appendix

7.1 Supplementary information

Table 7-1 Conversion and formation rates of the gasses in DRM over Pt and Ni at a reaction of 1123 K and 1.0 MPa

Turnover frequency [mol/(sec*mol(metal)]				**Pt**		
Time	CH_4	CO_2	CO	H_2	H_2O
20	37	39	64	57	11
40	22	23	39	42	5
60	14	11	19	23	3
80	8	5	9	13	3
100	5	1	2	10	3
Turnover frequency [mol/(sec*mol(metal)]				**Ni**		
Time	CH_4	CO_2	CO	H_2	H_2O
20	24	40	63	33	5
40	17	16	27	21	8
60	13	13	21	28	5
80	13	9	11	20	5
100	10	4	4	17	5

Table 7-2 Detailed results of the reaction flow analysis. For every carbon containing surface component the possible surface reactions, including desorption, are given with their respective probability under the given conditions. Those results were obtained using DETCHEM^{BATCH} from the previously published reforming mechanisms for Ni and Pt.

Pt				**Ni**			
CO_2*				**CO_2***			
CO_2*	→	CO_2 + *	99.9%	CO_2*	→	CO_2 + *	17.3%
CO_2* + C*	→	2 CO*	0.01%	CO_2* + *	→	2 CO* + O*	82.7%
CO_2* + H	→	C* + OH*	0.09%				
CO*				**CO***			
CO*	→	CO + *	100%	CO*	→	CO + *	99%
				CO + H*	→	C* + OH*	1%
CH_4*				**CH_4***			
CH_4* + *	→	CH_3* + H*	99.9%	CH_4* + *	→	CH_3* + H*	100%
CH_4* + OH*	→	CH_3* + H_2O*	0.1%				
CH_3*				**CH_3***			
CH_3* + *	→	CH_2* + H*	100%	CH_3* + *	→	CH_2* + H*	96.5%
				CH_3* + H*	→	CH_4* + *	3.5%
CH_2*				**CH_2***			
CH_2* + *	→	CH* + H*	74%	CH_2* + *	→	CH* + H*	48%
CH_2* + H*	→	CH_3* + *	26%	CH_2* + H*	→	CH_3* + *	52%
CH*				**CH***			
CH* + *	→	C* + H*	33%	CH* + *	→	C* + H*	99%
CH* + H*	→	CH_2* + *	67%	CH* + H*	→	CH_2* + *	1%
C*				**C***			
C* + H*	→	CH* + *	99.7%	C* + H*	→	CH* + *	0.1%
C* + O*	→	CO* + *	0.05	C* + O*	→	CO* + *	1.4%
C* + CO_2*	→	2 CO*	0.25%	C* + OH*	→	CO* + H*	98.6%

Equation	Number
The chemical potential of SRM, DRM and RWGS can be described as:	
$$Q_{SRM}=\frac{[H_2]_{av}^3[CO]_{av}}{[CH_4]_{av}[H_2O]_{av}}$$	(7-1)
$$Q_{DRM}=\frac{[H_2]_{av}^2[CO]_{av}^2}{[CO_2]_{av}[CH_4]_{av}}$$	(7-2)
$$Q_{RWGS}=\frac{[H_2O]_{out}[CO]_{out}}{[CO_2]_{out}[H_2]_{out}}$$	(7-3)
This renders the approach to equilibrium for the three reactions to be:	
$$\eta_{SRM}=\frac{Q_{SRM}}{K_{SRM}}=\frac{[H_2]_{out}^3[CO]_{out}}{[CO_2]_{out}[H_2O]_{out}}\frac{1}{K_{SRM}}$$	(7-4)
$$\eta_{DRM}=\frac{Q_{DRM}}{K_{DRM}}=\frac{[H_2]_{out}^2[CO]_{out}^2}{[CO_2]_{out}[CH_4]_{out}}\frac{1}{K_{DRM}}$$	(7-5)
$$\eta_{RWGS}=\frac{Q_{RWGS}}{K_{RWGS}}=\frac{[H_2O]_{out}[CO]_{out}}{[CO_2]_{out}[H_2]_{out}}\frac{1}{K_{RWGS}}$$	(7-6)
From the approach to equilibrium and the net rates of the conversion of CH_4 and CO_2, the forward turnover rates of DRM and RWGS can be calculated as:	
$$r_{DRM,f}=\frac{r_{net,\,CH4}}{1-\eta_{DRM}}$$	(7-7)
$$r_{RWGS}=\frac{r_{CO_2,net}-r_{DRM,f}}{1-\eta_{RWGS}}.$$	(7-8)
The three possible RDSs for the DRM and the one for RWGS, as described in the reaction network are:	
$$r_{DRM,1+2}=k_1p(CH_4)[*]^2$$	(7-9)
$$r_{DRM,a}=k_{5a}[C^*_a][O^*_a]$$	(7-10)
$$r_{DRM,b}=k_{4b}[CH^*_b][O^*_b]$$	(7-11)

$$r_{RWGS} = k_7[H^*][O^*] \quad (7\text{-}12)$$

The cascade of dehydrogenation of CH_4 can kinetically be described as

$$[CH_3{}^*] = \frac{k_1 p(CH_4)[*]^2}{k_2[*]} = \frac{k_1 p(CH_4)[*]}{k_2} \quad (7\text{-}13)$$

$$[CH_2{}^*] = \frac{k_2[CH_3{}^*][*]}{k_3[*]} = \frac{k_2}{k_3}\frac{k_1 p(CH_4)[*]}{k_2} = \frac{k_1 p(CH_4)[*]}{k_3} \quad (7\text{-}14)$$

$$[CH^*] = \frac{k_3[CH_3{}^*][*]}{k_4[*]} = \frac{k_3}{k_4}\frac{k_1 p(CH_4)[*]}{k_3} = \frac{k_1 p(CH_4)[*]}{k_4} \quad (7\text{-}15)$$

$$[CH_3{}^*] + [CH_2{}^*] + [CH^*] = \frac{k_1 p(CH_4)[*]}{k_2} + \frac{k_1 p(CH_4)[*]}{k_3} + \frac{k_1 p(CH_4)[*]}{k_4} = \frac{(k_2 + k_3 + k_4)k_1 p(CH_4)[*]}{k_2 k_3 k_4}$$

$$\text{with } [CH_3{}^*] + [CH_2{}^*] + [CH^*] = [CH_{x,a}{}^*] \text{ and } \frac{1}{k_{x,a}} = \frac{(k_2 + k_3 + k_4)}{k_2 k_3 k_4} \quad (7\text{-}16)$$

$$[CH_{x,a}{}^*] = \left(\frac{k_1 p(CH_4)}{k_{x,a}}\right)[*]$$

$$[CH_3{}^*] + [CH_2{}^*] = \frac{k_1 p(CH_4)[*]}{k_2} + \frac{k_1 p(CH_4)[*]}{k_3} = \frac{(k_2 + k_3)k_1 p(CH_4)[*]}{k_2 k_3}$$

$$\text{with } [CH_3{}^*] + [CH_2{}^*] = [CH_{x,b}{}^*] \text{ and } \frac{1}{k_{x,b}} = \frac{(k_2 + k_3)}{k_2 k_3} \quad (7\text{-}17)$$

$$[CH_{x,b}{}^*] = \frac{k_1 p(CH_4)[*]}{k_{x,b}}$$

The next sequence will describe the calculation of the site balance equation in **case a,** which can be denoted as:

$$[T]_a = 1 = [*] + [C^*{}_a] + [CH_{x,a}{}^*] + [CO^*] + [H^*] + [OH^*] + [O^*{}_a] \quad (7\text{-}18)$$

Assuming adsorption-desorption equilibrium for the three species H_2, CO and H_2O gives the terms for the surface coverages of H*, CO* and OH* as:

$$[H^*] = \sqrt{\frac{p(H_2)}{K_9}}[*] \quad (7\text{-}19)$$

$$[CO^*] = \frac{p(CO)}{K_{10}}[*] \quad (7\text{-}20)$$

$$[OH^*] = \frac{K_8 p(H_2O)}{\sqrt{\frac{p(H_2)}{K_9}}}[*] \tag{7-21}$$

In addition, under the assumption of the pseudo steady state hypothesis (PSSH) the two species O^*_a and C^*_a can be denoted as:

$$[O^*_a] = \frac{k_6 p(CO_2)[*]^2}{k_{5a}[C^*_a] + k_7[H^*]} \tag{7-22}$$

$$[C^*_a] = \frac{k_1 p(CH_4)[*]^2}{k_{5a}[O^*_a]} \tag{7-23}$$

Substituting [H*] by (7-19) and $[C^*_a]$ by (7-23) in (7-22) gives (7-24):

$$[O^*_a] = \frac{k_6 p(CO_2)[*]^2}{k_{5a}[C^*_a] + k_7[H^*]} = \frac{k_6 p(CO_2)[*]^2}{k_{5a}\frac{k_1 p(CH_4)[*]^2}{k_{5a}[O^*_a]} + k_7\sqrt{\frac{p(H_2)}{K_9}}[*]}$$

$$[O^*_a] = \left(\frac{k_6 p(CO_2) - k_1 p(CH_4)}{k_7\sqrt{\frac{p(H_2)}{K_9}}}\right)[*] \tag{7-24}$$

Substituting $[O^*_a]$ by (7-24) in (7-23) gives (7-25), which is convertible to (7-26):

$$[C^*_a] = \frac{k_1 p(CH_4)[*]^2}{k_{5a}[O^*_a]} = \frac{k_1 p(CH_4)[*]^2}{k_{5a}\left(\frac{k_6 p(CO_2) - k_1 p(CH_4)}{k_7\sqrt{\frac{p(H_2)}{K_9}}}\right)[*]} \tag{7-25}$$

$$[C^*_a] = \left(\frac{k_1 k_7\sqrt{\frac{p(H_2)}{K_9}}\, p(CH_4)}{k_{5a}(k_6 p(CO_2) - k_1 p(CH_4))}\right)[*] \tag{7-26}$$

$CH_{x,a}$* is product of the irreversible dehydrogenation cascade of CH_4 and following the PHHS hypothesis, it can be described in (7-16):

$$[CH_{x,a}{}^*] = \left(\frac{k_1 p(CH_4)}{k_{x,a}}\right)[*] \tag{7-27}$$

Using equations (7-19), (7-20), (7-21), (7-24), (7-26) and (7-27) to substitute all unknown expressions in (7-18) gives the following term. $[T]_a$ can therefore be described as function of the concentration of empty sites $[*]$.

$$[T]_a = 1 = [*] + [C^*{}_a] + [CH_{x,a}{}^*] + [CO^*] + [H^*] + [OH^*] + [O^*{}_a] =$$

$$\left(1 + \frac{k_1 k_7 \sqrt{\frac{p(H_2)}{K_9}}\, p(CH_4)}{k_{5a}(k_6 p(CO_2) - k_1 p(CH_4))} + \frac{k_1 p(CH_4)}{k_{x,a}} + \frac{p(CO)}{K_{10}} + \sqrt{\frac{p(H_2)}{K_9}} + \frac{K_8 p(H_2O)}{\sqrt{\frac{p(H_2)}{K_9}}} + \frac{k_6 p(CO_2) - k_1 p(CH_4)}{k_7 \sqrt{\frac{p(H_2)}{K_9}}}\right)[*] \quad (7\text{-}28)$$

The following section will deduce $[T]_b$ with the same assumptions for **case b**. The terms for [H*], [CO*] and [OH*] ((7-19), (7-20) and (7-21)) will be the same here:

$$[T]_b = [*] + [CH_{x,b}{}^*] + [CH^*{}_b] + [CO^*] + [H^*] + [OH^*] + [O^*{}_b] + [COH^*{}_b] \quad (7\text{-}29)$$

The PSSH for $CH_{x,b}$*, O^*_b, CH^*_b and COH^*_b give the following terms. Equation (7-30) is equal as derived in (7-17), only dependent on a partial pressure and does not need to be transformed further.

$$[CH_{x,b}{}^*] = \frac{k_1 p(CH_4)[*]}{k_{x,b}} \quad (7\text{-}30)$$

$$[O^*{}_b] = \frac{k_6 p(CO_2)[*]^2}{k_{4b}[CH_b{}^*] + k_7[H^*]} \quad (7\text{-}31)$$

$$[CH^*{}_b] = \frac{k_1 p(CH_4)[*]^2}{k_{4b}[O^*{}_b]} \quad (7\text{-}32)$$

$$[COH^*{}_b] = \frac{k_{4b}[CH_b{}^*][O^*{}_b]}{k_{5b}[*]} \quad (7\text{-}33)$$

In (7-31), the term for $[CH^*_b]$ is substituted by (7-32) and [H*] by (7-19) to give:

$$[O^*{}_b] = \frac{k_6 p(CO_2)[*]^2}{k_{4b}[CH^*{}_b] + k_7[H^*]} = \frac{k_6 p(CO_2)[*]^2}{k_{4b}\frac{k_1 p(CH_4)[*]^2}{k_{4b}[O^*{}_b]} + k_7\sqrt{\frac{p(H_2)}{K_9}}[*]} \quad (7\text{-}34)$$

This term can be rewritten as:

$$[O^*{}_b] = \left(\frac{k_6 p(CO_2) - k_1 p(CH_4)}{k_7 \sqrt{\frac{p(H_2)}{K_9}}}\right)[*] \quad (7\text{-}35)$$

The term $[O^*_b]$ in equation (7-32) can be replaced by (7-35) to give term (7-36), which can be further reconfigured to (7-37):

$$[CH^*{}_b] = \frac{k_1 p(CH_4)[*]^2}{k_{4b}[O^*{}_b]} = \frac{k_1 p(CH_4)[*]^2}{k_{4b}\left(\frac{k_6 p(CO_2) - k_1 p(CH_4)}{k_7\sqrt{\frac{p(H_2)}{K_9}}}\right)[*]} \quad (7\text{-}36)$$

$$[CH^*{}_b] = \left(\frac{k_1 k_7\sqrt{\frac{p(H_2)}{K_9}}\, p(CH_4)}{k_{4b}(k_6 p(CO_2) - k_1 p(CH_4))}\right)[*] \quad (7\text{-}37)$$

Substituting [CH*$_b$] by (7-32) in term (7-33) and reducing the fraction gives:

$$[COH^*{}_b] = \frac{k_{4b}[CH^*{}_b][O^*{}_b]}{k_{5b}[*]} = \frac{k_{4b}\frac{k_1 p(CH_4)[*]^2}{k_{4b}[O^*{}_b]}[O^*{}_b]}{k_{5b}[*]} = \frac{k_1 p(CH_4)}{k_{5b}}[*] \quad (7\text{-}38)$$

Substitution the unknown expressions for the surface species by the terms (7-19), (7-20), (7-21), (7-30), (7-35), (7-37) and (7-38) according to the ones leading to term (7-28), give the following expression for [T]$_b$ as a function of the empty sites [$*$]

$[T]_b = 1 = [*] + [CH_{x,b}{}^*] + [CH^*{}_b] + [CO^*] + [H^*] + [OH^*] + [O^*{}_b] + [COH^*{}_b]$=

$$\left(1 + \frac{k_1 p(CH_4)}{k_{x,b}} + \frac{k_1 k_7\sqrt{\frac{p(H_2)}{K_9}}\, p(CH_4)}{k_{4b}(k_6 p(CO_2) - k_1 p(CH_4))} + \frac{p(CO)}{K_{10}} + \sqrt{\frac{p(H_2)}{K_9}} + \frac{K_8 p(H_2O)}{\sqrt{\frac{p(H_2)}{K_9}}} + \frac{k_6 p(CO_2) - k_1 p(CH_4)}{k_7\sqrt{\frac{p(H_2)}{K_9}}} + \frac{k_1 p(CH_4)}{k_{5b}}\right)[*] \quad (7\text{-}39)$$

All expressions that contain partial pressures of gasses with zero order (i.e. H_2, CO and H_2O) are assumed to be zero. This is true for [H*], [CO*], [OH*], [C*$_a$], [O*$_a$], [O*$_b$] [CH*$_b$] and reduces the expressions for [T]$_a$ (7-28) to (4-36) and [T]$_b$ (7-39) to (4-37):

$$[T]_a = \left(1 + \frac{k_1 p(CH_4)}{k_{x,a}}\right)[*] \quad (7\text{-}40)$$

$$[T]_b = \left(1 + \frac{k_1 p(CH_4)}{k_{x,b}} + \frac{k_1 p(CH_4)}{k_{5b}}\right)[*] = \left(1 + \frac{k_1(k_{x,b} + k_{5b})p(CH_4)}{k_{x,b}k_{5b}}\right)[*] \quad (7\text{-}41)$$

Substitution of $k_1/k_{x,a}$ by k_a in (7-40) and $(k_1*(k_{x,b}+k_{5b}))/(k_{x,b}k_{5b}))$ by k_b in (7-41) results to:

$$[T]_a = 1 = \left(1 + k_a p(CH_4)\right)[*] \quad \text{and} \quad [T]_b = 1 = \left(1 + k_b p(CH_4)\right)[*] \quad (7\text{-}42)$$

This highlights the similarity of the surface coverages in case a and b, which can therefore be expressed as:

$$[\mathrm{T}] = 1 = \left(1 + \mathrm{k_{a/b}p(CH_4)}\right)[*] \tag{7-43}$$

Rewriting this equation gives an expression for [∗], which results to

$$[*] = \frac{[\mathrm{T}]}{\left(1 + \mathrm{k_{a/b}p(CH_4)}\right)} = \frac{1}{\left(1 + \mathrm{k_{a/b}p(CH_4)}\right)} \tag{7-44}$$

Replacing [∗] in term (7-9) by this expression gives

$$\mathbf{r_{DRM,1+2}} = \frac{\mathbf{k_1 p(CH_4)}}{\left(\mathbf{1 + k_{a/b}p(CH_4)}\right)^2} \quad \textbf{(in Regime 1 and 2)} \tag{7-45}$$

Putting into term (7-10) the expression (7-22) for [O*$_a$] and into (7-11) the expression (7-31) for [O*$_b$], respectively, gives the following terms. Under the given conditions in Regime 1 (CH_4/CO_2-ratios > 2), one can assume that k_{5a}[C*$_a$] >> k_7[H*] and k_{4b}[C*$_a$] >> k_7[H*], respectively. Therefore, k_7[H*] becomes 0 and the terms can be rewritten as (7-46) and (7-47):

$$\mathrm{r_{DRM,a1}} = \mathrm{k_{5a}[C^*{}_a][O^*{}_a]} = \mathrm{k_{5a}[C^*{}_a]}\frac{\mathrm{k_6 p(CO_2)[*]^2}}{\mathrm{k_{5a}[C^*{}_a] + k_7[H^*]}} = \mathrm{k_6 p(CO_2)[*]^2} \tag{7-46}$$

$$\mathrm{r_{DRM,b1}} = \mathrm{k_{4b}[CH^*{}_b][O^*{}_b]} = \mathrm{k_{4b}[CH^*{}_b]}\frac{\mathrm{k_6 p(CO_2)[*]^2}}{\mathrm{k_{4b}[CH^*{}_b] + k_7[H^*]}} = \mathrm{k_6 p(CO_2)[*]^2} \tag{7-47}$$

Both terms are equal and replacing [∗] by (7-44) gives for both:

$$\mathbf{r_{DRM,1}} = \frac{\mathbf{k_6 p(CO_2)}}{\left(\mathbf{1 + k_{a/b}p(CH_4)}\right)^2} \quad \textbf{(in Regime 1)} \tag{7-48}$$

Replacing [O*$_a$] (by (7-24)), [C*$_a$] (by (7-26)), [O*$_b$] (by (7-35)) and [CH*$_b$] (by (7-37)), in the terms (7-10) and (7-11), respectively, gives the following expressions for the rates under the conditions of Regime 2 (CH_4/CO_2-ratios < 2):

$$\mathrm{r_{DRM,a2}} = \mathrm{k_{5a}[C^*{}_a][O^*{}_a]} =$$

$$\mathrm{k_{5a}}\left(\frac{\mathrm{k_1 k_7}\sqrt{\frac{\mathrm{p(H_2)}}{\mathrm{K_9}}}\,\mathrm{p(CH_4)}}{\mathrm{k_{5a}(k_6 p(CO_2) - k_1 p(CH_4))}}\right)[*]\left(\frac{\mathrm{k_6 p(CO_2) - k_1 p(CH_4)}}{\mathrm{k_7}\sqrt{\frac{\mathrm{p(H_2)}}{\mathrm{K_9}}}}\right)[*] = \mathrm{k_1 p(CH_4)[*]^2} \tag{7-49}$$

$$\mathrm{r_{DRM,b2}} = \mathrm{k_{4b}[CH^*{}_b][O^*{}_b]} = \tag{7-50}$$

$$= k_{4b}\left(\frac{k_1 k_7\sqrt{\frac{p(H_2)}{K_9}}\,p(CH_4)}{k_{4b}(k_6 p(CO_2) - k_1 p(CH_4))}\right)[*]\left(\frac{k_6 p(CO_2) - k_1 p(CH_4)}{k_7\sqrt{\frac{p(H_2)}{K_9}}}\right)[*] = k_1 p(CH_4)[*]^2$$

Substitution of $[*]$ by (7-44) gives again for both equations above:

$$\mathbf{r_{DRM,2}} = \frac{\mathbf{k_1 p(CH_4)}}{\left(\mathbf{1 + k_{a/b} p(CH_4)}\right)^2} \quad \textbf{(in Regime 2)} \qquad \textbf{(7-51)}$$

Substituting (7-12) with (7-19) and (7-35) (only for Regime 2, because in Regime 1 there is no RWGS observable) gives the term for the RWGS. Substitution of $[*]$ with (7-44) subsequently gives (7-52).

$$\mathbf{r_{RWGS,2}} = k_7[H^*][O^*{}_b] = k_7\sqrt{\frac{p(H_2)}{K_9}}\left(\frac{k_6 p(CO_2) - k_1 p(CH_4)}{k_7\sqrt{\frac{p(H_2)}{K_9}}}\right)[*]^2 = \qquad (7\text{-}52)$$

$$\left(k_6 p(CO_2) - k_1 p(CH_4)\right)[*]^2 = \frac{\left(\mathbf{k_6 p(CO_2) - k_1 p(CH_4)}\right)}{\left(\mathbf{1 + k_{a/b} p(CH_4)}\right)^2}$$

With the conversion rate of CO_2 being defined as the sum of DRM and RWGS, in the two regimes the terms for CO_2 turnover are as follows:

$$r_{CO_2} = r_{DRM} + r_{RWGS} \qquad (7\text{-}53)$$

$$r_{CO_2,1} = r_{DRM,1} + 0 = \frac{k_6 p(CO_2)}{\left(1 + k_{a/b} p(CH_4)\right)^2} \qquad (7\text{-}54)$$

$$r_{CO_2,2} = r_{DRM,2} + r_{RWGS,2} = \qquad (7\text{-}55)$$

$$\frac{k_1 p(CH_4)}{\left(1 + k_{a/b} p(CH_4)\right)^2} + \frac{\left(k_6 p(CO_2) - k_1 p(CH_4)\right)}{\left(1 + k_{a/b} p(CH_4)\right)^2} = \frac{k_6 p(CO_2)}{\left(1 + k_{a/b} p(CH_4)\right)^2}$$

7.2 List of Tables

7.3 List of Figures

7.4 List of publications

Structure-Activity Relationships of Nickel-Hexaaluminates in Reforming Reactions Part I: Controlling Nickel Nanoparticle Growth and Phase Formation
T. Roussière, K.M. Schelkle, S. Titlbach, G. Wasserschaff, A. Milanov, G. Cox, E. Schwab, O. Deutschmann, L. Schulz, A. Jentys, J. Lercher, S.A. Schunk
ChemCatChem, 6 **(2014)** 1438-1446

Structure-Activity Relationships of Nickel-Hexaaluminates in Reforming Reactions Part II: Activity and Stability of Nanostructured Nickel-Hexaaluminate-Based Catalysts in the Dry Reforming of Methane
T. Roussière, L. Schulz, K.M. Schelkle, G. Wasserschaff, A. Milanov, E. Schwab, O. Deutschmann, A. Jentys, J. Lercher, S.A. Schunk
ChemCatChem, 6 **(2014)** 1447-1452

On the coke deposition in dry reforming of methane at elevated pressures
L. Schulz, L.C.S. Kahle, K.H. Delgado, S.A. Schunk, A. Jentys, O. Deutschmann, J.A. Lercher
Applied Catalysis A: General, **(2015)** 599-607

Kinetic modelling of methane dry reforming on a Ni-Hexaaluminate at high pressures
L. Schulz, Y.-H. Chin, W. Tu, Y. Lou, A. Jentys, J.A. Lercher*
To be published

7.5 List of conference contributions

7.5.1 Oral presentations

Isotope labelling investigations on the mechanism of methane dry reforming
L. Schulz, A. Jentys, J.A. Lercher
46. Jahrestreffen deutscher Katalytiker, Weimar, **March 2013**

Dry reforming of methane at elevated pressures
L. Schulz, Y. Lou, A. Jentys, J.A. Lercher, K. Herrera Delgado, L. Kahle, O. Deutschmann
DGMK Meeting on New Technologies and Alternative Feedstock, Dresden, **October 2013**

7.5.2 Posters

DRYREF: Dry Reforming of CO_2 at Elevated Pressures
T. Roussière, S. Schunk, G. Wasserschaff, A. Milanov, E. Schwab, A. Behrens, N. Schoedel, L. Burger, O. Deutschmann, K. Herrera, R. Gläser, J. Peters, B. Scholze, A. Jentys, J. Lercher, L. Schulz
44. Jahrestreffen deutscher Katalytiker, Weimar, **March 2011**

DRYREF: Dry Reforming of CO_2 at Elevated Pressures
T. Roussière, S. Schunk, G. Wasserschaff, A. Milanov, E. Schwab, A. Behrens, N. Schoedel, L. Burger, O. Deutschmann, K. Herrera, R. Gläser, B. Scholze, L. Schulz, A. Jentys, J. Lercher
45. Jahrestreffen deutscher Katalytiker, Weimar, **March 2012**

Understanding the Reduction Mechanism of Ni-Hexaaluminates – a Mechanistic Proposal
K. M. Schelke, T. Roussière, S. Schunk, G. Wasserschaff, A. Milanov, E. Schwab, G. Cox, O. Deutschmann, L. Schulz, A. Jentys, J. Lercher
46. Jahrestreffen deutscher Katalytiker, Weimar, **March 2013**

Understanding Structure-Property Relationships for Ni-containing Hexaaluminates in the Dry Reforming of Methane
T. Roussière, K. M. Schelke, S. Schunk, G. Wasserschaff, A. Milanov, E. Schwab, G. Cox, O. Deutschmann, L. Schulz, A. Jentys, J. Lercher
46. Jahrestreffen deutscher Katalytiker, Weimar, **March 2013**